FIRST-PRINCIPLES STUDY OF SPINTRONIC PHENOMENA IN MAGNETIC TUNNEL JUNCTIONS AND GRAPHENE

Hongxin Yang

UNIVERSITÉ DE GRENOBLE

THÈSE

Pour obtenir le grade de

DOCTEUR DE L'UNIVERSITÉ DE GRENOBLE

Spécialité : **Physique**

Arrêté ministériel : 7 août 2006

Présentée par

Hongxin YANG

Thèse dirigée par **Mairbek CHSHIEV**

préparée au sein du **Laboratoire SPINTEC**
(UMR CEA/CNRS/UJF/Grenoble INP)
dans **l'École Doctorale de Physique**

FIRST-PRINCIPLES STUDY OF SPINTRONIC PHENOMENA IN MAGNETIC TUNNEL JUNCTIONS AND GRAPHENE

Thèse soutenue publiquement le **13 March 2012**
devant le jury composé de :

M. Stefan BLÜGEL (Rapporteur)
Prof., Peter Grünberg Institut & Institute for Advanced Simulation, Jülich
M. Stefano SANVITO (Rapporteur)
Prof., Trinity College, Dublin
M. André THIAVILLE (Examinateur)
D.R. CNRS, Laboratoire de Physique des Solides, Université Paris-sud, Orsay
M. Alain SCHUHL
Prof., Université Joseph-Fourier & Institut Néel, Grenoble
Mme Claudine LACROIX (Examinateur)
D.R. CNRS, Institut Néel, Grenoble
M. Mairbek CHSHIEV (Directeur de Thèse)
Prof., Université Joseph-Fourier & Spintec, Grenoble

Contents

Chapter 1

General introduction

In recent decades, progress in fabrication and characterization of systems with reduced dimensionality has stimulated fundamental research on a wide range of quantum phenomena and has enabled development of nanomaterials with new functionalities related to new information technologies. The most remarkable event, in this context, is the discovery of giant magnetoresistance (GMR) in magnetic multilayered structures in 1988 by the groups of A. Fert [BBF$^+$88] and P. Grünberg [BGSZ89]. They observed a significant change in the resistance of multilayers when the magnetizations of adjacent ferromagnetic layers separated by a nonmagnetic spacer were brought into alignment by an applied magnetic field. This discovery opened new ways of exploring magnetic properties of materials by means of spin-dependent transport and generated a new field of research called spin electronics or spintronics [Ohn98, WAB$^+$01, FBY$^+$01a, BFC$^+$02], which combines two traditional fields of physics: magnetism and electronics. In other words, it is not only the electron charge but also the electron spin that is used to operate a device. Spin is the intrinsic angular momentum of a particle which, in the case of the electron, is characterized by a quantum number equal to 1/2 with two possible states called "spin-up" and "spin-down" (or "majority" and "minority"). In ferromagnetic materials, the Coulomb interaction and Pauli exclusion principle cause a long-range ordering of the unpaired up (or down) spins leading to the finite magnetic moment μ per unit volume (magnetization M) resulting from the difference of majority and minority density of states (DOS). Furthermore, such inequality of the DOS for two spin states at the Fermi surface leads to significantly different conductivities for the spin up and the spin down electrons as was demonstrated by A. Fert and I. Campbell in the late 1960s [CFP67, FC68]. Along with the existence of the long range interlayer coupling between two ferromagnets separated by a nonmagnetic spacer [GSP$^+$86], these observations were the key steps in the discovery of GMR suggesting that the transport in ferromagnetic materials is spin-dependent and can be considered within the two current model [Mot36]. Giant magnetoresistance became the supreme manifestation of spin-dependent transport and was recognized by the award of the Nobel Prize 2007 to A. Fert and P. Grünberg.

The essential prerequisite of discovery of GMR is interlayer exchange coupling (IEC), which is one of the most fundamental phenomena in spintronics. The phenomenon has been demonstrated in 1986 [GSP$^+$86, MCK$^+$86, SSR$^+$86] between the magnetizations of two ferromangetic layers separated by a non-magnetic spacer. It is found that magnets can interact from long distance through nonmangetic spacer to form either ferromagnetic

or antiferromangetic exchange coupling. Further research in these systems leads to the discovery of GMR effect in 1988 [BBF$^+$88, BGSZ89].

The initial explanation for the oscillatory interlayer exchange coupling was based on the Ruderman-Kittel-Kasuya-Yosida (RKKY) indirect exchange which originally described the coupling between two nuclear spins embedded in a degenerated electron gas. Its effective Hamiltonian can be represented by [Slo95],

$$H_{eff}(\rho) = \frac{J_{lc}^2 m_e Q^4 F(2Qd)\mathbf{S_i} \cdot \mathbf{S_j}}{2\pi^3\hbar^2}, \tag{1.1}$$

$$F(z) = \frac{zcosz - sinz}{z^4}, \tag{1.2}$$

where function F is proportional to the nonlocal susceptibility of the gas, d is the distance between local atom spins S_i and S_j, J_{lc} represents the exchange integral between a local electron and a conduction electron, m_e is the mass of electron, and Q is the Fermi vector of the free electron gas. Summing H_{eff} over atomic position i in one magnet and j in the other one gives the coupling energy per unit area

$$W = -J_1 cos\theta, \tag{1.3}$$

where θ is the angle between the two magnetization vectors.

The simple application of RKKY theory, where spin distribution within the ferromagnetic layers is uniform and the spacer thickness was assumed to be able to vary continuously, yields a period $\Lambda = \lambda_F/2 = 1ML$, which is too short compared to the experimental results [BC91a]. The generalized theory of RKKY interlayer exchange coupling was proposed by P. Bruno and C. Chappert [BC91a, BC91b, BC92], where the coupling was related in a physically transparent manner to the topological properties of the Fermi surface at the spacer material. Two key aspects in the interlayer exchange coupling were addressed: (i) the interaction between a ferromagnetic layer and the host conduction electrons, and (ii) the way the spin-polarization is propagated across the host material. The first aspect can actually be ascribed by using the basis of s-$d(f)$ model which is usually used to deal transition metal magnetic impurities.

By 1993, there were a number of theoretical models for interlayer exchange coupling proposed [Sti93, BC91a, BC91b, BC92, Slo95]. From that time on, a flourished one and a half decades, a simple physical picture for interlayer exchange coupling has evolved. Spin dependent reflection from the interfaces in multilayers leads to formation of spin-dependent quantum well states. These quantum well states evolve in energy as the thickness of the spacer layer is varied. As these states pass through the Fermi energy, they are filled or empty therefore changing the energy of the multilayer. These changes are periodic because the quantum well states cross the Fermi energy with a period determined by the Fermi surface of the spacer layer material. At critical points of this Fermi surface, many quantum well states have the same period giving a net oscillatory contribution to the energy. Since the reflection is spin dependent, the energy depends on the relative orientation of the layer magnetizations, i.e., there is an energy difference between parallel and antiparallel alignment of the magnetizations. This energy difference is indeed the interlayer exchange coupling. It has oscillatory contributions with periods determined by the critical spanning vectors of the spacer layer Fermi surface and strengths determined by the spin-dependent reflection at the interfaces.

The advent of GMR has renewed the interest in spin dependent tunneling [Jul75] across semiconductors and insulators and led to demonstrations of high tunnel magnetoresistance ratios (TMR) at room temperature [MKWM95, MT95] in magnetic tunnel junctions (MTJs). MTJs consist of two ferromagnetic (FM) electrodes separated by an insulating barrier have been objects of great interest from both fundamental and applied perspectives. High sensitivity to magnetic fields makes these structures good candidates for hard drive magnetoresistive read heads, logic devices and magnetic random access memories [PRS$^+$99, TCD$^+$99, IHL$^+$07]. Various aspects have been addressed, both theoretically and experimentally, regarding spin dependent properties in MTJs such as the role of disorder and impurities at the interfaces between ferromagnetic and oxide layers, the impact of the junction composition on TMR ratio, temperature dependence of the latter, etc. [TP98, TP99, SWN99, LSK$^+$00, LSKdJ00, DTBF$^+$99a, DTBF$^+$99b, BFC$^+$02, BBVD02, VBBD01, DCT$^+$01, DGC$^+$03, DHC$^+$04, TML03].

A major breakthrough in the area of spin-dependent tunneling was the prediction of extremely high tunnel magnetoresistance ratios for certain epitaxially grown magnetic tunnel junctions [MZBW99, BZSM01, MU01, WMZ$^+$02]. This prediction was based on a spin filtering effect that may arise from the symmetry of the wave functions. At the Fermi energies of bcc Fe, bcc Co and CoFeB, there is a difference in the symmetries of wave functions between the majority and minority spin channels. Specifically there is a Δ_1 Bloch state for the majority, but not for the minority. For some insulating and semiconducting materials, states with this Δ_1 symmetry will decay much more slowly than states with different symmetries due to the presence of corresponding evanescent states in the band gap [BZSM01, MU01, DMW$^+$02, BZV$^+$05, VCB06]. In other words, an insulator separating two ferromagnetic electrodes should not be viewed as a simple barrier and electron tunneling cannot be accurately described in the framework of the Julliere model [Jul75]. Recent experiments [PKP$^+$04, YNF$^+$04, Ike08] largely confirmed predictions made by W. H. Butler et al. [BZSM01] and J. Mathon et al. [MU01] for MgO based tunnel junctions. So far the record values of TMR ratio on MgO-based MTJs reached 600% at room temperature [LHI$^+$07]. This discovery also has a large impact on the technologies of MRAM and of read sensors for hard drives.

In contrast to the case of a metal spacer, much fewer investigations have been devoted to interlayer exchange coupling across nonmetallic spacer layers [TBHL92, Bru95, FML$^+$92, CMW96, KCE$^+$97, EKS99, GBB$^+$01]. The interest has been strongly enforced with the observation of antiferromagnetic interlayer exchange coupling in 2002 in Fe|MgO|Fe crystalline magnetic tunnel junctions (MTJs) by J. Faure-Vincent and coauthors who reported IEC values up to -0.26 mJ/m^2 for thin MgO layer thicknesses [FVTB$^+$02]. The AF IEC phenomenon across the insulator was initially explained using the free electron model for pure tunneling [FVTB$^+$02, Slo89] and the resonant tunneling mechanism due to the presence of localized impurity or defect states in the insulating barrier layer [ZTV05, ZVVT06]. For instance, it was shown from first-principles calculations that oxygen vacancies located in the middle of the MgO layer as well as interfacial oxygen [WAMS08] cause the IEC to be AF for MgO thicknesses below 0.8 nm [KYV$^+$06, ZVVT06]. In recent experiments, Chiang *et al.* [CWT$^+$09] investigated the role of interfacial oxidation on the IEC in Fe|MgO|Fe MTJs and found that oxidation conditions can strongly affect the character of the IEC for MgO thicknesses below 1 nm. They observed that for MgO thicknesses up to 0.6 nm both under- and overoxidized

junctions show AF IEC which is much stronger in case of under-oxidation. However, the IEC becomes FM in case of overoxidized samples for MgO thicknesses larger than 0.6 nm ($\sim$ 3 monolayers). So far, the explanation for IEC across the over- and under-oxidized MgO interface structures is in a well agreement with experimental results, whereas there have been inconsistencies between the experimentally observed *AF* IEC [FVTB$^+$02] and first-principles calculated *FM* IEC in pure Fe|MgO|Fe MTJs [KYV$^+$06, ZVVT06].

In this thesis, we revisited interlayer exchange coupling in Fe|MgO|Fe MTJs and investigated this phenomenon in **Chapter 2**, where the effects of structural relaxation and oxidation conditions on interlayer exchange coupling are presented from first-principles and tight-binding model calculations. In addition, we extend the study of IEC to some other structures with semicondutors separating ferromagnets to have a general view of IEC across insulating spacers.

Another very interesting spintronic phenomenon observed in MTJs is the perpendicular magnetic anisotropy (PMA). Monso *et al*. have shown that PMA could be observed at Co(Fe)|MOx interfaces (M=Ta, Mg, Al, Ru etc.) [MRA$^+$02, RAD$^+$03] in spite of the weak spin-orbit interaction in the system. Large PMA values up to 1 to 2 erg/cm^2 have been reported, which are comparable or even larger than the PMA values observed at Co|Pt or Co|Pd interfaces [GLW$^+$06, JJKdB95]. This result is quite general and has been observed in both crystalline (MgO) or amorphous (AlOx) barriers, using both natural or plasma oxidation [LHA$^+$07, MDL$^+$08, MPV$^+$08]. Especially, recent experiments reported large PMA values of 1.3 erg/cm^2 at CoFeB|MgO structures [IMY$^+$10, EKI$^+$10]. Furthermore, it has been experimentally demonstrated that there is a strong correlation between PMA and TMR maximum values obtained at the same optimal oxidation and annealing conditions [NRD$^+$10].

Even though the experiments show such surprisingly large PMA values and the optimized PMA and TMR maximum at the same oxidation conditions, the understanding of this correlation is not clear. The works on the mechanism of the large PMA at Fe|MgO interfaces are of particular interest. The paper by Nakamura et al used a single layer of Fe on MgO to explore the electric field induced magnetic anisotropy [NAI$^+$10]. They reported that an ideal abrupt Fe|MgO interface gives rise to a large out-of-plane magnetic anisotropy due to weak Fe-O hybridization at the interface, but the anisotropy switching by an applied electric field is found to be difficult to achieve. Instead, the existence of an interfacial FeO layer plays a key role in demonstrating the anisotropy switching that accompanies an electric-field-induced displacement of Fe atoms on the interfacial FeO layer. For PMA at thicker Fe layers on MgO (001) surface, M. K. Niranjan *et al*. have calculated the magnetoelectric effects originating from the influence of an external electric field on magnetic properties of the Fe|MgO(001) interface [NDJT10]. They have shown that the effect on the interface magnetization and magnetocrystalline anisotropy can be substantially enhanced if the electric field is applied across a dielectric material with a large dielectric constant. They predict the effect of electric field on the interface magnetocrystalline anisotropy due to the change in the relative occupancy of the 3*d*-orbitals of Fe atoms at the Fe|MgO interface. However, the PMA mechanism at Fe|MgO interfaces is not clear enough. In particularly, there is no reports about the correlation between PMA and TMR, even though in experiments by L.E. Nistor and coauthors. It was shown that the anisotropy reaches its maximum in the optimal oxidation conditions [NRD$^+$10].

We will devote the **Chapter 3** to investigate mechanisms of magnetic anisotropy at Fe|MgO and Co|MgO interfaces, and will understand them in terms of correlation between Bloch states symmetry based spin-filtering and PMA in MgO-based MTJs.

Starting from **Chapter 4**, we will work on another novel branch of spintronics, namely graphene-based spintronics [FBY+01b, WAB+01, HMP+12]. We will start from PMA at Co|graphene interfaces. Furthermore, magnetic behavior and work function of Co surfaces due to graphene coverage will also be investigated.

Graphene is a very interesting material because it is a real realized two dimensional sheet of carbon atoms in a honeycomb lattice, known as the thinnest material in the universe, can be rolled up to form carbon nanotube, or stacked to form graphite, exhibiting many unique properties. For example, its charge carriers exhibit giant intrinsic mobility, have zero effective mass, and can travel for micrometers without scattering at room temperature. Graphene can sustain current densities six orders of magnitude higher than that of copper, shows record thermal conductivity and stiffness, is impermeable to gases, and reconciles such conflicting qualities as brittleness and ductility. Electron transport in graphene is described by a Dirac-like equation, which allows the investigation of relativistic quantum phenomena in a benchtop experiment [CNGP+09, Gei09, DSAHR11]. For groundbreaking experiments regarding the two-dimensional material graphene, the Nobel Prize in physcis was awarded to A. Geim and K. Novoselov in 2010.

In addition to its promising properties for electronics, graphene is also very attractive for spintronics [FBY+01b, WAB+01], this is due to expected very long spin lifetimes thank to its intrinsic weak spin-orbit coupling and hyperfine interaction, which allows for the spin population to remain spin polarized even over long channel lengths. Also, recent studies have shown spin transport in graphene to be tunable by an electrically controlled back gate [HMP+12].

Another useful feature is that graphene is only one atom thick, and therefore the surface is extremely sensitive to whatever is lying on top of it. It therefore becomes possible to chemically dope the surface to probe the electrical and spin properties of graphene in ways not possible (or very hard) in other systems. Furthermore, as graphene is a nearly ideal two-dimensional system, it provides many interesting phenomena from the point of view of fundamental physics research such as the (fractional and integer) Quantum Hall Effect (FQHE and IQHE) and 'tabletop' relativistic physics [DSD+09, BGS+09, NGM+05, ZLB+12]. Combining these advantages, graphene is an extremely interesting material in the field and opens a new direction for spintronics. For example, exciting spin-dependent effects have been observed or predicted, noticeably in graphene-based non-local spin valve devices: efficient spin injection [TJP+07a], a quest for controlling spin injection in graphene [TJP+07b, HWP+09, HPM+10, YBV+11], and spin-filtering [SCL06b]. In particular, FM|graphene|FM epitaxial stacks with high magnetoresistance [KGK+07] and low resistance area product [YP09] attracted considerable attention in this respect.

Not only spin transport but also spin polarization in graphene is a topic of intense interest. Two-dimensional nature of graphene is again appealing, that is in this aspect, due to shaped nanoribbons and nanomeshes whose edges may intrinsically carry spin-polarized currents (states) [SCL06b, BZJ+10]. Graphene may also be inserted between two planar ferromagnets to build giant magnetoresistance junctions operated

in a current perpendicular to the plane configuration, with neither too low (like for giant magnetoresistance) nor too high (like for tunnel magnetoresistance) resistance-area product, and with extremely thin spacers [KGK+07, YP09]. The magnetoresistive effect outlined in the latter proposal calls for the availability of epitaxial FM|graphene|FM trilayers, due to the importance of band matching with graphene [GKB+08]. This requires that epitaxial graphene be prepared on ferromagnetic supports, which was demonstrated years ago [ON97], and also requires the development of epitaxial two dimensional ferromagnetic layers on top of graphene.

Therefore such layers may serve as building blocks in a number of spintronics setups beyond the scope of magnetoresistive junctions. For instance, a large Rashba field may develop in an ultrathin two dimensional metallic ferromagnetic layer sandwiched between graphene and another metal layer of a heavy element such as gold, due to a strong out-of-plane electron potential gradient resulting from the structural inversion asymmetry imposed by the two distinct interfaces [VSBS+08, RVSB+09, GDM+11].

Beyond the magnetic metal, with magnetic insulating substrates to induce magnetization in graphene is also interesting. This is basically due to the requirements of some devices for spin-polarization and band gap opening. As one knows, that semiconducting devices rely on the gap because it is the gap that allows a semiconductor to be switched from conducting to insulating. In principle, the larger the gap the better for application since it insures a large on to off ratio for switching devices. Therefore, for graphene-based electronic applications, to open a gap is crucial. One way to open a gap in graphene is using confined structures, e.g. graphene nanoribbon and graphene nonomeshes [SCL06b, BZJ+10]. Indeed, a graphene ribbon with a width of 1 nm has theoretically a band gap of nearly 1 eV. An energy gap of this magnitude is good enough for electronic applications, but the size scale of 1 nm is in the range of fabrication limit. In the sense of size scale, graphene nanomeshes may help to solve the problem [BZJ+10]. Another solution to obtain large scale opened-gap graphene is using insulating substrate, the very famous one is using 4H- or 6H-SiC substrate. But other insulating substrates are also intensively investigated, for example, Al_2O_3, MgO, SiO_2, BN and GaAs. While, in the field of spintronics, if one wants to induce magnetism and a gap, one choice turns to the insulating magnetic substrates. As for magnetic insulating materials there are NiO, EuO, EuS, FeO, $FeCo_2O_4$ and Fe_3O_4 etc., here, considering the lattice mismatch, we will choose EuO as substrate. The spin-polarization in graphene caused by EuO substrate will be addressed in **Chapter 5** and a tunable Dirac cone in graphene, as well as an unusual magnetic order in graphene will also be presented in the chapter.

We will next devote our efforts (**Chapter 6**) to another fundamental phenomenon of graphene spintronics, the intrinsic magnetism of graphene.

From experimental side, there are still debates about the magnetism in graphene, especially regarding the atomic-scale defects induced magnetism. Here atomic-scale defects include vacancies, chemisorbed species, grain boundaries etc. [YH07, Yaz08, Yaz10, PFP+08, FPBJ09, ZZZ+09, LFM+04, HZP10, CYL08, SNT+12]. It is indeed particularly difficult to achieve a precise experimental characterization of those defects, where the control of their density, positioning, or chemical reactivity seems an insurmountable challenge, jeopardizing a further use of magnetic properties in real devices. As for graphene nanoribbon, the half-metal property has been proposed for a long time [SCL06b], but its application is still far away. This is due to the scale

limitation (by tearing it into ribbons of less than 10 nm in width) and the zigzag-edge requirements, as well as difficulty to produce scalable arrays of devices.

Therefore, more easy controllable graphene-based materials are necessary. From this point of view, the recently reported graphene nanomesh may become one of the solutions [BZJ+10]. Jingwei Bai and co-workers constructed their devices using techniques borrowed from, and therefore compatible with, large scale semiconductor fabrication. A layer of graphene was coated with protective silica upon which lay a polystyrene film with a hexagonal array of cylindrical pores. Bombarding this with reactive ions transferred the pattern into the silica. A mesh was then created by placing the device when a voltage was applied across the contacts.

Since this material is recently realized in experiments [Gev10], the origin of the band gap is still unclear. Furthermore, the magnetic properties have not been yet well studied. In **Chapter 6**, we systematically investigate the magnetic properties of graphene nanomeshes as a function their shape and size.

The manuscript is organized as following:

Chapter 1, a general introduction of spintronic phenenomena during my Ph.D studies will be given.

Chapter 2, the interlayer exchange coupling across MgO-, $SrTiO_3$-, and GaAs(ZnSe)-based magnetic tunnel junctions is studied.

Chapter 3, perpendicular magnetic anisotropy at Fe|MgO and Co|MgO interfaces is investigated.

Chapter 4, perpendicular magnetic anisotropy and work function reduction at Co|graphene interfaces are calculated.

Chapter 5, the magnetic properties including (i) spin-polarization, (ii) tunning Dirac point and (iii) magnetic ordering in graphene induced by the magnetic insulator proximity effect are studied.

Chapter 6, the possibilities to obtain intrinsic magnetism in graphene nanomeshes are explored.

Finally, in **Chapter 7**, we give conclusions of this work.

Chapter 2

Interlayer Exchange Coupling (IEC)

2.1 *Ab initio* calculations of interlayer exchange coupling

When two ferromagnetic layers are separated by a non-magnetic spacer layer, one may expect, generally, two types of coupling, i.e. Ruderman-Kittel-Kasuya-Yosida (RKKY) type coupling, which is oscillatory [RK54, Kas56, Yos57], and nonoscillatory type with exponentially decrease as a function of the spacer thickness. The oscillatory exchange coupling was initially demonstrated in experiments in 1986 [GSP$^+$86, MCK$^+$86, SSR$^+$86]. Subsequent discoveries in these systems, including giant magnetoresistance (GMR) [BBF$^+$88, BGSZ89], led to an explosion in measurements and theories for more than two decades after its first observation [Yaf94, FGB$^+$95, JS95, Sti99, Bru99]. Unlike the intense research devoted to the interlayer exchange coupling (IEC) across metallic layers, investigations of interlayer exchange coupling across nonmetallic spacer layers were seldom studied. One of the pioneered studies was by Toscano et al. [TBHL92], who studied the coupling of Fe films separated by amorphous Si. A striking feature is that the coupling, in contrast to the case of a metal spacer, increases with increasing temperature [FDD$^+$93]. Since the beginning of this century, boosted by the giant tunnel magnetoresistance (TMR) predicted by Butler in 2001 in MgO-based magnetic tunnel junctions(MTJ) [BZSM01] and observed in 2004 [YNF$^+$04, PKP$^+$04], interlayer exchange coupling across large gap insulating spacers has been intensively studied [FVTB$^+$02].

The interlayer exchange coupling can be expressed in its simplest form,

$$\frac{E}{A} = -J\hat{\mathbf{m}}_\mathbf{1} \cdot \hat{\mathbf{m}}_\mathbf{2}, \tag{2.1}$$

which is called bilinear or *Heisenberg* energy expression because the energy per area (A) is linear in the directions of both magnetizations $\hat{\mathbf{m}}_\mathbf{i}$. With this definition of the coupling, positive values of the constant J favor parallel alignment of the magnetizations, whereas negative values favor antiparallel alignment. There are essentially two classes of approaches to calculate coupling constant: total energy calculations and model calculations. From equation (2.1), the interlayer coupling constant is given by the difference in energy between the antiparallel alignment of the magnetizations and the

parallel alignment

$$J = \frac{E_{anti} - E_{para}}{2A}. \tag{2.2}$$

The idea of the total energy calculations is to compute the energy difference between two configurations of parallel and antiparallel alignment of the magnetizations in neighboring magnetic layers. This can be done either within semiempirical tight-binding models or *ab initio* schemes. Although it is very simple and straightforward in principle, this kind of approach is actually very difficult because the energy difference between the two configurations is usually in order of $10^{-4} \sim 10^{-2}$ eV, whereas the total energy is of order $10^{2\sim4}$ eV. This makes the numerical convergence of the calculations a serious problem. Especially for the *ab initio* calculations, very precious K-point and cut off energy should be considered to use.

In this Chapter, we systematically investigate the interlayer exchange coupling in MgO-based magnetic tunnel junctions. In particular, we clarify the impact of relaxation and oxidation conditions on interlayer exchange coupling.

2.2 Interlayer exchange coupling in MgO-based magnetic tunnel junctions

We demonstrate from first principles the effects of structural relaxation and interfacial oxidations on interlayer exchange coupling (IEC) in crystalline Fe|MgO|Fe magnetic tunnel junctions (MTJ). It is shown that the IEC becomes antiferromagnetic for the relaxed structure in contrast to ferromagnetic for unrelaxed Fe|MgO|Fe MTJs. Furthermore, we show that the antiferromagnetic IEC is strongly enhanced in the presence of oxygen vacancies while it is decreased by overoxidation and may even become ferromagnetic for sufficiently high oxygen concentration at the Fe|MgO interface. These results are supported using a tight-binding model and provide an explanation for recent experimental studies.

2.2.1 Introduction

Since its first observation in Fe|Cr|Fe layered structures [GSP+86], interlayer exchange coupling (IEC) has been a subject of major interest to the spintronic community, both from fundamental and applications points of view [HB05]. This interest was strongly enhanced when antiferromagnetic (AF) IEC between ferromagnetic (FM) layers across an insulator was found in Fe|MgO|Fe crystalline magnetic tunnel junctions (MTJs) [FVTB+02]. Experimentally observed values for the IEC may reach up to -0.26 erg/cm^2 for thin MgO layer thicknesses[FVTB+02, KYV+06]. The AF IEC phenomenon was initially explained using the free electron model for pure tunnelling [FVTB+02, Slo89] and the resonant tunnelling mechanism due to the presence of localized impurity or defect states in the insulating barrier layer [ZTV05, ZVVT06]. For instance, it was shown from first principles that oxygen vacancies located in the middle of the MgO layer as well as interfacial oxygen [WAMS08] cause the IEC to be AF for MgO thicknesses below 0.8 nm [KYV+06, ZVVT06]. In a recent experiment, Chiang *et al.* [CWT+09] investigated the role of interfacial oxidation on the IEC in Fe|MgO|Fe MTJs and found that oxidation conditions can strongly affect the character of the IEC for MgO thicknesses below 1 nm. They observed that for MgO thicknesses up to 0.6 nm both under- and overoxidized junctions show AF IEC which is much stronger in case of underoxidation. However, the IEC becomes FM in case of overoxidized samples for MgO thicknesses larger than 0.6 nm ($\sim$ 3 monolayers(ML)).

Motivated by these observations and desiring to elucidate the impact of oxidation conditions on the nature of the IEC in single crystal MTJs, we performed systematic *ab initio* studies of (i) the influence of oxygen impurities and vacancies and (ii) the effects of structural relaxation on the IEC. We found that oxygen vacancies cause strong AF IEC in agreement with previous theoretical [KYV+06, ZVVT06] and experimental [KYV+06, CWT+09] studies. Furthermore, interfacial oxidation decreases the AF IEC and may even lead to FM IEC depending on the interfacial oxygen concentration. Most importantly, we theoretically demonstrate that the full structural relaxation of pure Fe|MgO|Fe MTJs may lead to AF IEC.

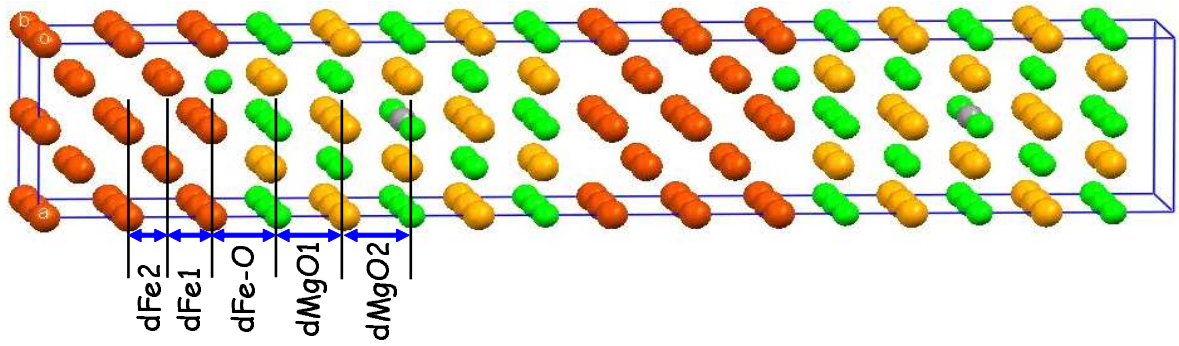

Fig. 2.1 : 2×2 supercell of $[Fe_5(MgO)_5]_2$ used for the calculations of additional oxygen located at the Fe|MgO interface and oxygen vacancy (grey ball). Red ball is Fe, green ball is oxygen and orange ball is Mg.

Table 2.1: Interlayer distances (Å) of $[Fe_5(MgO)_x]_2$. Unrelaxed results are taken from Ref.[BZSM01], the values of $Fe_{10}(MgO)_6$ are taken from Ref.[FBA$^+$09].

Structures	dFe1	dFe2	dFe-O	dMgO1	dMgO2
$[Fe_5(MgO)_2]_2$	1.252	1.405	2.115	2.149	
$[Fe_5(MgO)_3]_2$	1.240	1.398	2.101	2.099	2.099
$[Fe_5(MgO)_4]_2$	1.236	1.395	2.097	2.099	2.120
$[Fe_5(MgO)_5]_2$	1.231	1.392	2.092	2.094	2.111
Unrelaxed	1.433	1.433	2.160	2.026	2.026
$Fe_{10}(MgO)_6$(GGA)	1.350	1.427	2.219	2.219	2.177
$Fe_{10}(MgO)_6$(LSDA)	1.120	1.343	2.002	2.130	2.119

2.2.2 Calculation details

We carried out first-principles calculations by using the Vienna *ab initio* simulation package (VASP) [KH93, KF96b, KF96a]. In our calculations, the electron-core interactions were described by the projector augmented wave method for the pseudopotentials [Blo94, KJ99], and the exchange correlation energy was obtained within the generalized gradient approximation [WP91]. The cutoff energies for the plane wave basis set used to expand the Kohn-Sham orbitals were 400 eV for the ionic relaxations and 500 eV for the subsequent self-consistent FM (AF) energy calculations.

To calculate the IEC, one needs the total energies for parallel and antiparallel structures, respectively. Thus, we constructed periodic supercells of Fe|MgO|Fe|MgO comprising thicknesses between 2 and 5 MLs for MgO layers with the thickness of the Fe layers kept equal to 5 MLs. The lateral cell size accommodated 4 Fe, 4 Mg and 4 O per layer or 8 Fe, 8 Mg, and 8 O per layer [Figure 2.1]. The Monkhorst-Pack scheme was used for the Brillouin zone integration [MP76]. A 21×21×1 k-point mesh was sufficient to ensure good convergence in the total energy differences. Full structural relaxations in shape and volume were performed ensuring that the Hellmann-Feynman forces acting on ions were less than 10^{-3} eV/Å.

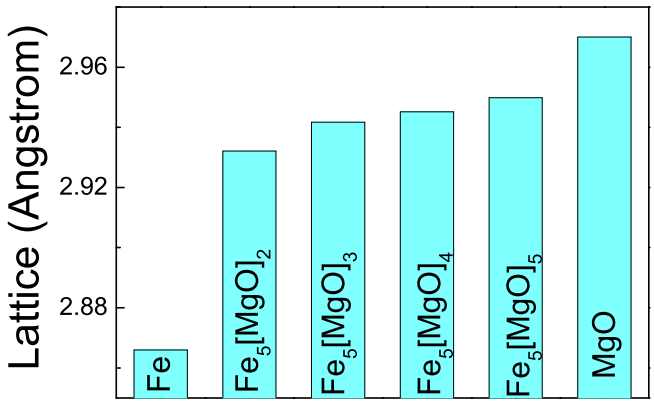

Fig. 2.2 : In plane lattice constant of $[Fe_5(MgO)_x]_2$ as a funciton of MgO thickness.

The IEC constant J across one barrier region and normalized by the lateral area (A)of the computational cell is defined as

$$J = \frac{E_{AP} - E_P}{4A}, \tag{2.3}$$

where E_P and E_{AP} represent total energies for parallel and anti-parallel alignments of adjacent Fe layer magnetizations, respectively. To ensure an accurate value for J, calculations were performed in three steps. First, we relaxed the structure with parallel alignment of Fe slabs magnetizations. Next, we calculated the total energy E_P (E_{AP}) for FM (AF) configuration with the relaxed structure. Finally, the strength of the IEC was calculated using formula (2.3).

2.2.3 Structural Relaxation Effects on Interlayer Exchange Coupling

We begin by describing the results of the structural relaxation of the "pure" structure, i. e. with no vacancies and/or additional oxygen. The longitudional interatomic distances along the out-of-plane (001) direction are summarized in Table 2.1. One can note that the interlayer distances within Fe are strongly decreased compared to unrelaxed structures used in Ref. [BZSM01]. Furthermore, the distances between the first and second interfacial Fe layers (dFe1) are shorter than the distances between the second and third ones (dFe2). This is consistent with previous results for $Fe_{10}(MgO)_6$ [FBA$^+$09] and can be attributed to the formation of the interface. At the same time, the thicknesses of MgO slabs are less affected compared to unrelaxed structures, but the MgO interlayer distances are still shorter around the Fe|MgO interface compared to those within the bulk. Finally, the interfacial Fe-O distances are found to be slightly shorter compared to unrelaxed distances (2.16 Å) or bulk FeO (2.154 Å) [MPK$^+$01] and fall between values obtained within GGA and LSDA approximations in $Fe_{10}(MgO)_6$ [FBA$^+$09] (see Table 2.1). The slight discrepancies between aforementioned interlayer distances and those reported in Ref. [FBA$^+$09] within GGA aproximation are due to full structural

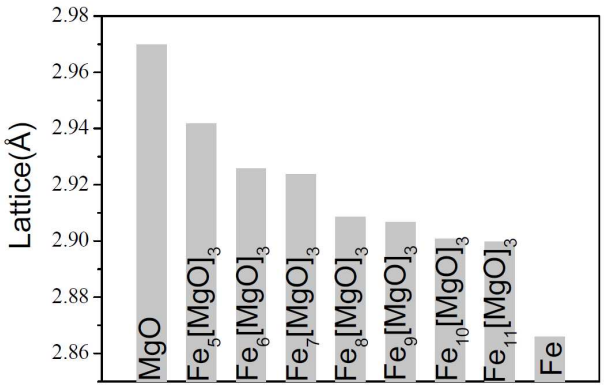

Fig. 2.3 : In plane lattice constant of $[Fe_x(MgO)_3]_2$ as a funciton of Fe thickness.

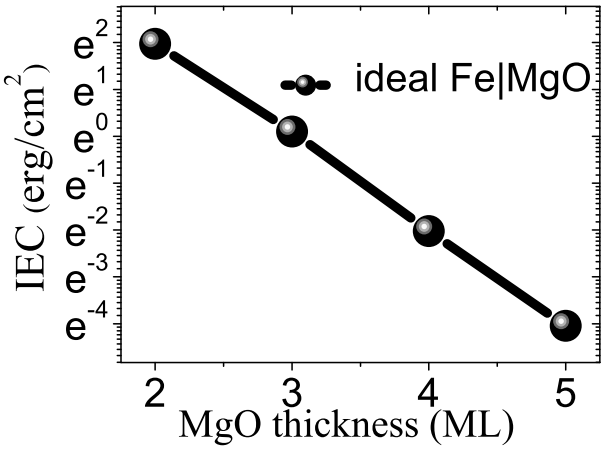

Fig. 2.4 : IEC for unrelaxed $[Fe_5(MgO)_x]_2$.

relaxation in shape and volume performed in our case unlike that in Ref. [FBA+09].

In the lateral direction, the Fe layers expand while the MgO layers shrink compared to the bulk values for bcc Fe (2.866 Å) and rocksalt MgO ($\frac{\sqrt{2}}{2}a_{MgO}$=2.977 Å), respectively, as shown in Figure 2.2. One can indeed note that for all cases investigated the relaxed lateral lattice constants are found to be distributed between those for the bulk bcc Fe and MgO (Figure 2.2). This result can be viewed as a relaxation"compromise" between these materials originating from the mismatch between different crystal lattices comprising the supercell under investigation. To further prove this, we also investigate the lateral lattice constant for $Fe_x(MgO)_3]_2$ as shown in (Figure 2.3). One sees that the lattice constant 'smoothly' decreases with increasing Fe layers.

Let us now to discuss the calculated IEC values for these structures. In Figure 2.5(black circles) we show the dependence of the IEC on MgO thicknesses between 2 and 5 MLs. Surprisingly, the IEC is found to be AF unlike the case of unrelaxed structures where we found the IEC to be FM [Figure 2.4] in agreement with Ref. [KYV+06, ZVVT06]. This underlines the crucial importance of structural relaxation on IEC similarly to the case of transport properties in Fe|MgO MTJs [FBA+09]. The values of IEC for relaxed structures can reach up to -0.406 erg/cm^2 and -0.038

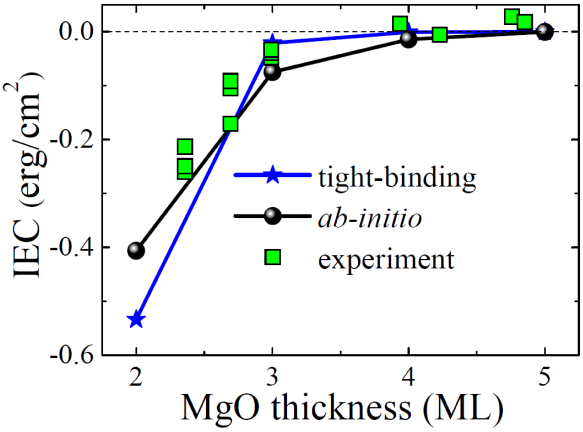

Fig. 2.5 : IEC for $[Fe_5(MgO)_x]_2$ calculated using *ab initio* and tight-binding methods together with experimental results taken from Ref. [FVTB$^+$02].

erg/cm^2 for structures with 2 and 3 MLs of MgO, respectively. These values are in agreement with experimental results [FVTB$^+$02] as shown with open squares in Figure 2.5. To support these *ab initio* results, we performed total energy calculations using a single-band tight-binding model based on the nonequilibrium Green function technique. This method was successfully used to predict voltage dependences of the spin transfer torques (STT) in MgO-based MTJs [TKK$^+$06, CTK$^+$08, KCT$^+$09]. Taking the parameters from Refs [CTK$^+$08, KCT$^+$09] corresponding to the measured STT voltage dependences [KFY$^+$08, SCS$^+$08], where the hopping and exchange-splitting parameters are - 1.0 eV and 1.3 eV, respectively. The spin-averaged on-site energies for electrodes and barriers are 4.3 eV and 9.0 eV, respectively. Fermi energy is set to zero. The resulting IEC turns out to be AF in agreement with the *ab initio* results (Figure 2.5) providing support for simple modeling approaches to spin-dependent tunneling in MTJs.

2.2.4 Oxidation Effects on Interlayer Exchange Coupling

Next, we investigated the effects of oxidation conditions on IEC in the Fe|MgO|Fe MTJs. The underoxidation was modeled by creating an oxygen vacancy in the middle of the MgO (grey ball in Figure 2.1) while the overoxidized case was represented by additional oxygen atoms at the Fe|MgO interface (Figure 2.1). The calculated results are summarized in Figure 2.6. One can see that oxygen vacancies strongly enhance the AF IEC in agreement with previous theoretical [ZVVT06] and experimental studies [CWT$^+$09] (see Figure 2.6, orange hexagons). At the same time interfacial oxidation decreases the strength of AF IEC (Figure 2.6, blue up triangles) and may cause the IEC to become ferromagnetic for higher oxygen concentration (Figure 2.6, purple down triangles) in partial agreement with experiment [CWT$^+$09] (see Figure 2.6, green diamonds). We included in Figure 2.6 the case of the pure MTJ (black squares) in order to clearly represent the impact of oxidation on the nature of the IEC. Namely, one can note that as the amount of oxygen present in the MTJ increases, the AF IEC first decreases, vanishes and becomes finally

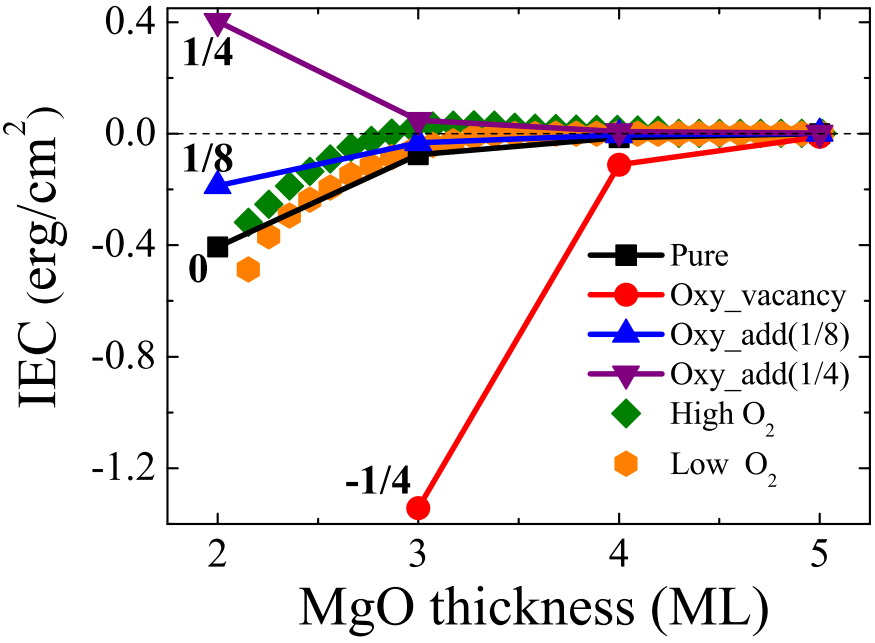

Fig. 2.6 : IEC for $[Fe_5(MgO)_x]_2$ pure structure (black squares), for the case with oxygen vacancy in the MgO layer (red circles), and two cases with 1/8 (blue up triangles) and 1/4 (purple down triangles) oxygen at the interface as a function of MgO thickness. The experimental results for IEC with high(green diamond) and low O_2 (orange hexagon) conditions are taken from Ref. [CWT$^+$09]

ferromagnetic (red circles→black squares→blue up triangles→ purple down triangles trend in Figure 2.6).

2.2.5 Conclusion

In conclusion, we presented systematic studies of the IEC in Fe|MgO|Fe structures and showed the impact of structural relaxation and oxidation conditions on the nature of IEC in MTJs. The IEC is found to be antiferromagnetic for relaxed structures in agreement with experiment. Furthermore, it is shown that the oxygen vacancy strongly enhances the AF IEC while additional oxygen at the Fe|MgO interface, on the contrary, weakens the AF IEC and may even change its sign to FM depending on the oxygen concentration.

2.3 IEC in $SrTiO_3$-based MTJs

In this section, the effect of ferromagnetic electrode compositions and barrier layer properties are demonstrated from first principles to have a crucial impact on interlayer exchange coupling (IEC) in crystalline Co(Fe)/$SrTiO_3$/Co(Fe) magnetic tunnel junctions. It is shown that the IEC can be varied from antiferromangtic to ferromagnetic by either changing the Co and Fe alloy ratio in the electrodes or the band gap of the barrier.

2.3.1 The choice of Co, Fe and $SrTiO_3$

Ground state of Strontium Titanate oxide ($SrTiO_3$ in short of STO) is a pervoskite cubic structure as shown in Figure 2.7(a). In our first-principles calculations, the band gap of STO is about 1.8 eV, as shown in Fig2.7(c), which is underestimated compared to experiments (experimentally determined indirect band gap energy of 3.25 eV, while the direct band gap energy is 3.75 eV), which is much lower than MgO (7.4 eV). In practice, this means that the tunnel barrier can be much thicker with the same Resistance × Area (RA) as MgO. Furthermore, STO deposited by ion beam sputtering exhibits outstanding low crystallization temperature at 260°C which contrasts with 650°C when deposited by RF sputtering. This makes ion beam sputtering STO compatible with usual magnetic electrodes.

Experimentally, in 1996 Lu et al. reported a TMR of 85% at 4 K in LSMO/STO/LSMO junctions [LLG+96]. Later, in 2003, Bowen et al. showed a TMR of 1800% at 4K for the same kind of structure [BBB+03].

At the same time, *ab initio* calculations indicated a high TMR at room temperature with epitaxial Co(bcc)|SrTiO3|Co(bcc) junctions [VBS+05]. With CoFe as electrode, the experimental attempt was realized by Coey et al. in 2009 based on sputtered STO MTJs [OC09]. The authors compared the results between MgO and STO MTJs deposited by RF sputtering. They reported a TMR of 2.25% at room temperature in CoFeB/STO/CoFeB based MTJs after annealing at 325°. Recent experiments of Spintec reported that the TMR can reach up to 13% [HVC+].

Similar to the case of Fe|MgO magnetic tunnel junctions, interlayer exchange coupling behavior in $SrTiO_3$ based MTJs is thus very interesting to address. Considering similar Bloch states spin-filtering in bcc Fe and bcc Co [Figure 2.8], here we investigate interlayer exchange coupling behavior in MTJs with Fe, Co and their mixed alloy as electrode and with $SrTiO_3$ as barrier spacer.

2.3.2 Structure of Co(Fe)|STO|Co(Fe) MTJs and calculation details

For the first-principles calculations, we again used the Vienna *ab initio* simulation package (VASP) [KH93, KF96b, KF96a]. In our calculations, the electron-core interactions were described by the projector augmented wave method for the pseudopotentials [Blo94, KJ99], and the exchange correlation energy was obtained within the generalized gradient approximation [WP91]. The cutoff energies for the plane wave basis set used to expand the Kohn-Sham orbitals were 500 eV for the ionic relaxations and for the subsequent self-consistent FM (AF) energy calculations. The Monkhorst-Pack scheme was used for

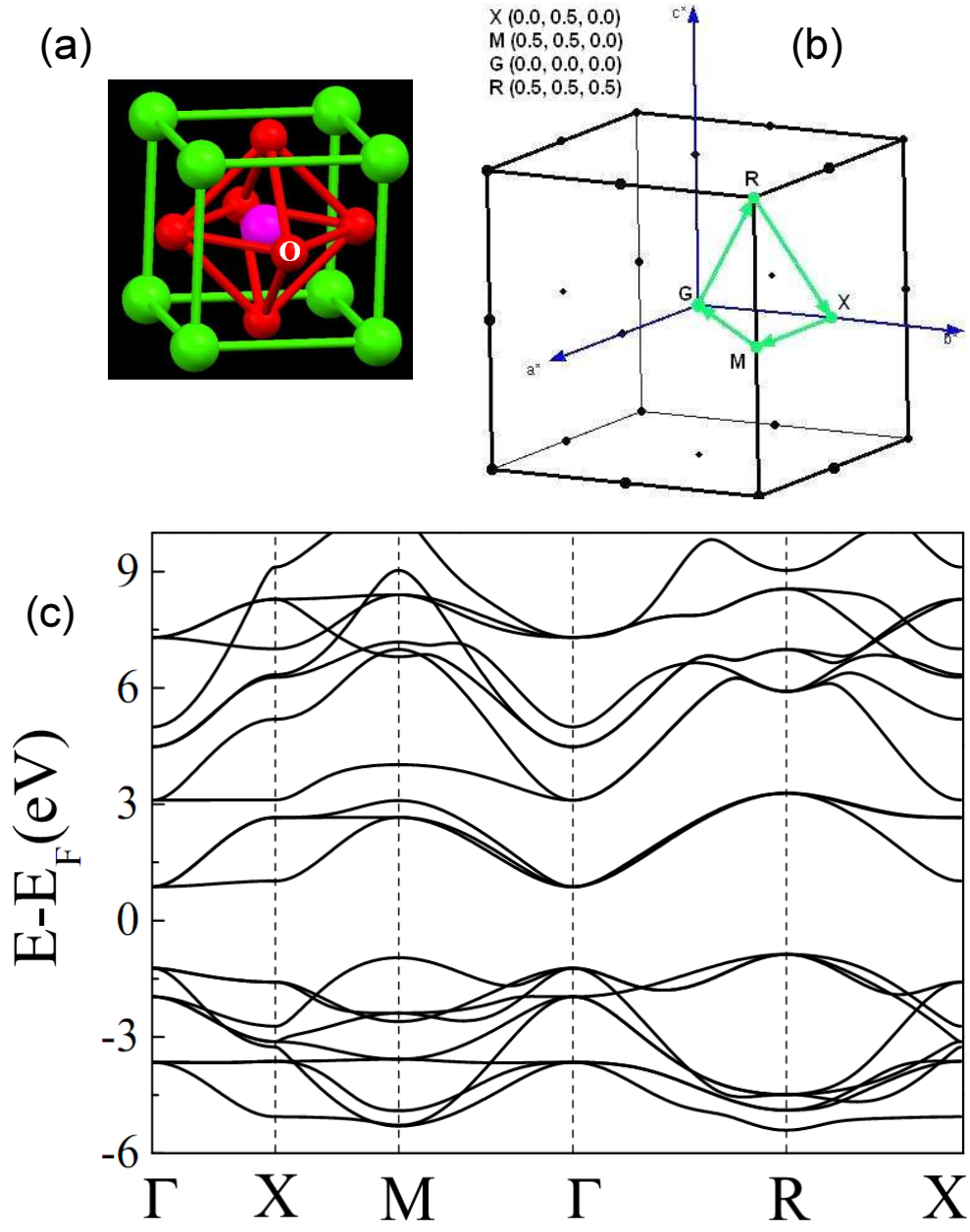

Fig. 2.7 : (a) Perovskite cubic SrTiO3 structure, (b) high symmetry K-points in Brillouin zone used for band structure calculations, and (c) band structure of SrTiO3 calculated with first-principles.

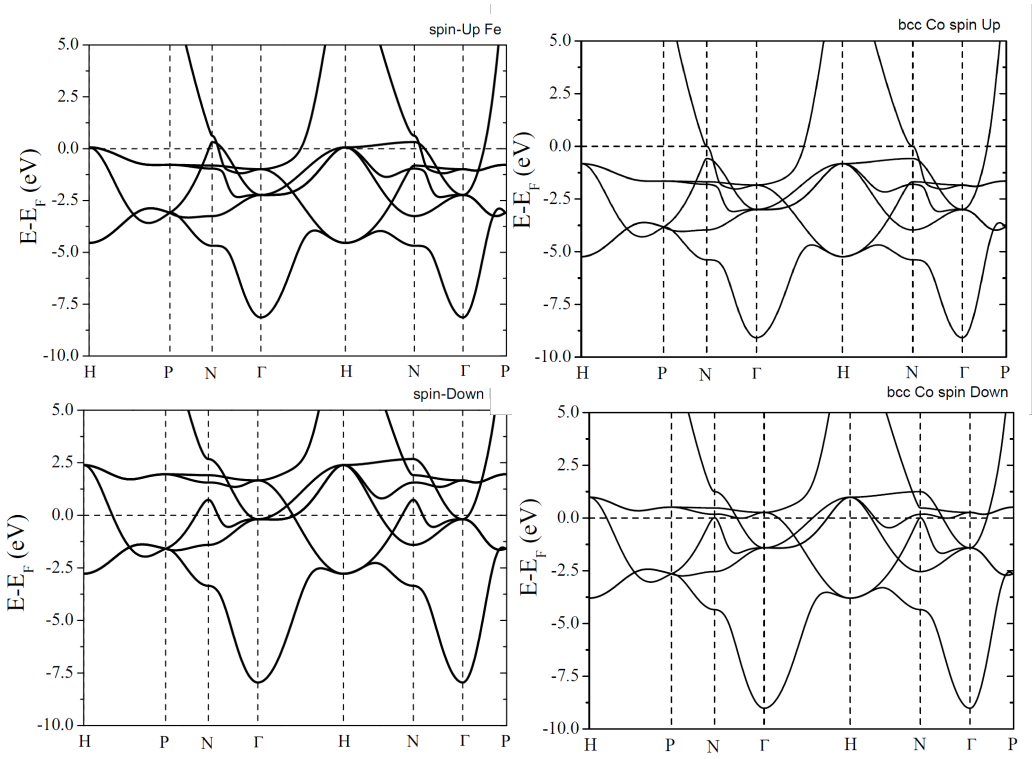

Fig. 2.8 : Band structures for bcc Fe and bcc Co. Upper panels are bcc Fe and bcc Co spin up band structures on left and right sides, respectively. Lower panels are their spin down band structures correspondingly.

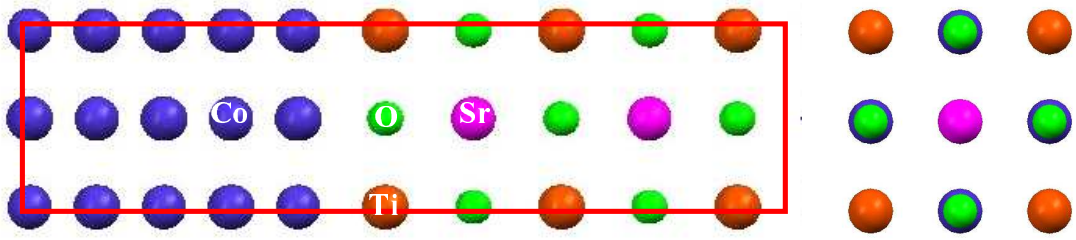

Fig. 2.9 : IEC for $[Fe_5(MgO)_x]_2$ pure structure (black squares), for the case with oxygen vacancy in the MgO layer (red circles), and two cases with 1/8 (blue up triangles) and 1/4 (purple down triangles) oxygen at the interface as a function of MgO thickness. The experimental results for IEC with high(green diamond) and low O_2 (orange hexagon) conditions are taken from Ref. [CWT$^+$09].

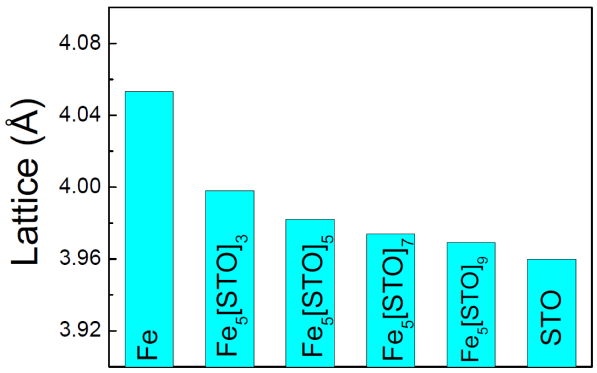

Fig. 2.10 : In plane lattice constant of $[Fe_5(STO)_x]_2$ as a function of STO thickness.

the Brillouin zone integration, and we have used a $19 \times 19 \times 3$ k-point mesh is sufficient to ensure a good convergence in the total energy differences in order to ensure the small IEC values are not affected by k-point convergence. Similar to the previous work in FeMgO, we constructed periodic supercells of Co(Fe)|STO|Co(Fe)|STO comprising thicknesses between 3 and 9 MLs for STO layers with the thickness of the Co(Fe) layers kept equal to 5 MLs. Full structural relaxations in shape and volume were performed ensuring that the Hellmann-Feynman forces acting on ions were less than 10^{-3} eV/Å. To further investigate the IEC as a function of band gap of STO, we used GGA+U methods, where U is added on Ti, we change U values from 3 to 7 eV to vary the band gap of the insulating barrier.

The relaxed equilibrium lattice parameter of bcc Co is 2.81 Å, which has only a 0.3% mismatch with the $SrTiO_3$ lattice (3.96 Å) rotated by 45° around the [001] axis [Figure 2.9].

In case of Fe|STO, the mismatch is about 2.3%. We found that, similar to Fe/MgO case, the relaxed lateral lattice constant depends on the ratio of STO and Fe content in the junction [Figure(2.10].

The definition of interlayer exchange coupling is the same as we used in previous section in equation(2.3).

2.3.3 Effects of ferromagnetic electrode on IEC

With pure Co, pure Fe and the mixed CoFe as magnetic electrodes in STO-based magnetic tunnel junctions, we show the calculated IEC in Figure 2.11. One can see that with Co as electrode, IEC is antiferromagnetic for all Co thicknesses considered. While with pure Fe as electrode, the coupling is ferromagnetic except at 7 monolayer STO thickness. With mixed FeCo magnetic electrode, the IEC values fall between those of Fe|STO and Co|STO cases.

To understand the different IEC behavior caused by Fe and Co electrodes, we analyze the density of states in the middle layer of STO as shown in Figure(2.11). For Co|STO, the Fermi level falls very close to the conduction band [lower left panel], while in case of Fe|STO, Fermi level falls in the middle of the band gap[upper right panel]. According to

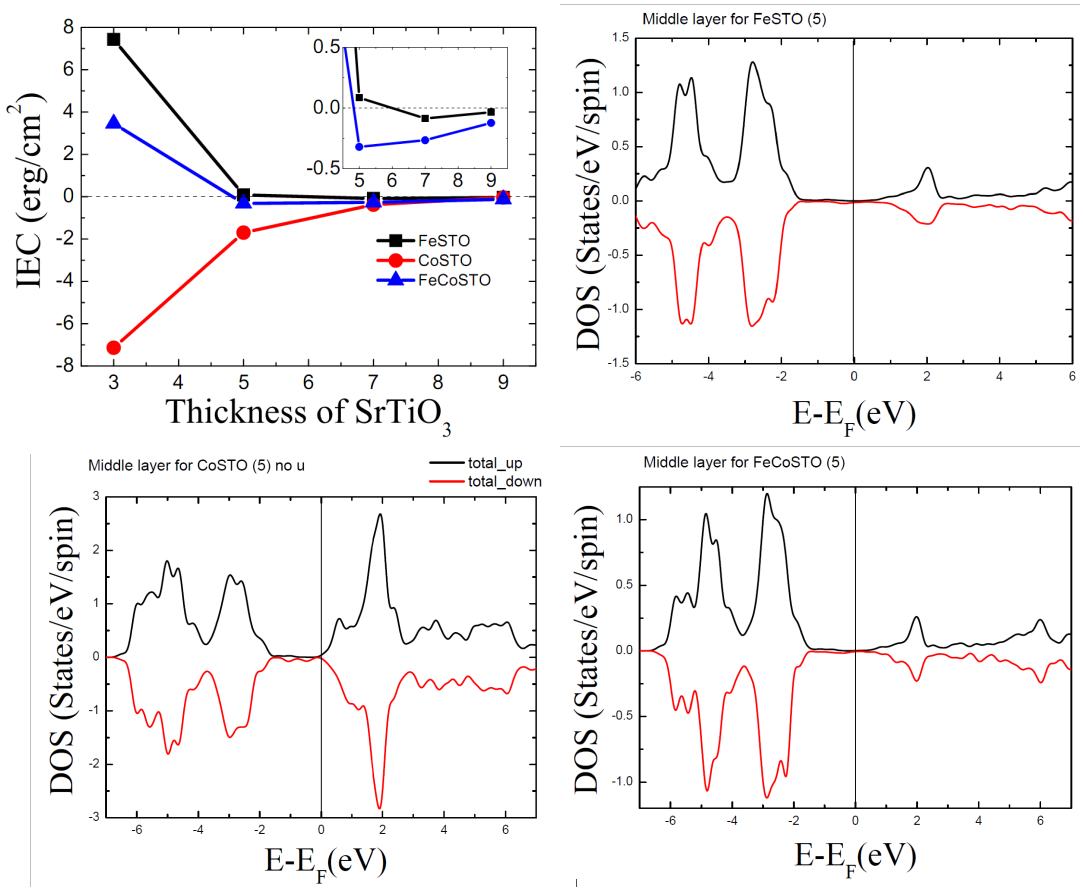

Fig. 2.11 : IEC for $[Co_5(STO)_x]_2$, $[Fe_5(STO)_x]_2$, and $(FeCo)_5(STO)_x]_2$ as a function of STO thickness. The density of states for the middle layer of STO are shown for the case of 5 monolayer STO.

the free electron model by P. Bruno [Bru95] or by J. C. Slonczewski [Slo93], in the case of an insulating spacer, the sign of the coupling at large spacer thicknesses is determined by the values of Fermi wave vectors in spacer $|k_F|$, and in magnetic electrodes, $k_F^{\uparrow}$ and $k_F^{\downarrow}$. when

$$|k_F|^2 < k_F^{\uparrow} k_F^{\downarrow}, \tag{2.4}$$

the coupling is antiferromagnetic, while for

$$|k_F|^2 > k_F^{\uparrow} k_F^{\downarrow}, \tag{2.5}$$

the coupling becomes ferromagnetic. It is hard to estimate the values of $k_F^{\uparrow}$ and $k_F^{\downarrow}$ from our first-principles calculations, but the value of

$$k_F = i\sqrt{2m(U - \epsilon_F)}, \tag{2.6}$$

is related to the energy from the bottom of barrier conduction band to the Fermi level. Since Fermi level almost touches the conduction band in $Co_5(STO)_7$ case, $|k_F|^2$ is close to zero giving a value smaller than $k_F^{\uparrow} k_F^{\downarrow}$. Therefore, the IEC should be antiferromagnetic. In case of $Co_5(STO)_7$, since the Fermi level falls in the middle of the band gap, thus U-ϵ_F becomes large, which may cause the square of $|k_F|$ larger than $k_F^{\uparrow} k_F^{\downarrow}$ and leading to ferromagnetic coupling across STO barrier.

2.3.4 Effects of barrier on IEC

As we have just seen, the exchange coupling strongly depends on the Fermi level position and the band gap of insulating spacer. It is known that the DFT calculations underestimate the band gap of STO. To get the correct band gap, one option would be using *GW* corrections. The *GW* approach, however, is very time consuming. So we employed DFT+U methods to correct the band gap. Even though the band gap from DFT+U is less accurate compared to *GW* corrections, the advantage of DFT+U is the fast calculation and tunable U. We show the calculated density of states for different U values in bulk $SrTiO_3$ structure in Figure 2.12. One can see that with increasing of U, the band gap is increasing and can reach up to 2.5 eV when U is set to 7 eV.

In order to see the IEC variation as a function of band gap, we choose the values of U equal to 3, 5 and 7 eV. The calculated IEC as a function of STO thicknesses for different band gaps tuned by parameter U in Co|STO magnetic tunnel junction is shown in Figure(2.13). One can see a clear trend of decreasing of AF IEC with increasing of U. When U is big enough, the coupling can even change its sign to ferromagnetic. The effects of U on insulating spacer is analyzed in Figure(2.13) for 7 monolayers of STO cases. With increasing of U, the band gap in the spacer is increasing as seen from the density of states in the TiO_2 layer in the middle of spacer. Here the sign change of IEC is similar to the aforementioned analysis. Since the value of $|k_F|^2$ is increasing with U, the coupling becomes ferromagnetic when the value of $|k_F|^2$ is larger than $k_F^{\uparrow} k_F^{\downarrow}$.

For the case of Fe/STO, the coupling becomes ferromagnetic for all thicknesses considered [Figure 2.14]. At the same time the values of IEC are quite similar for U set to 5 and 7 eV.

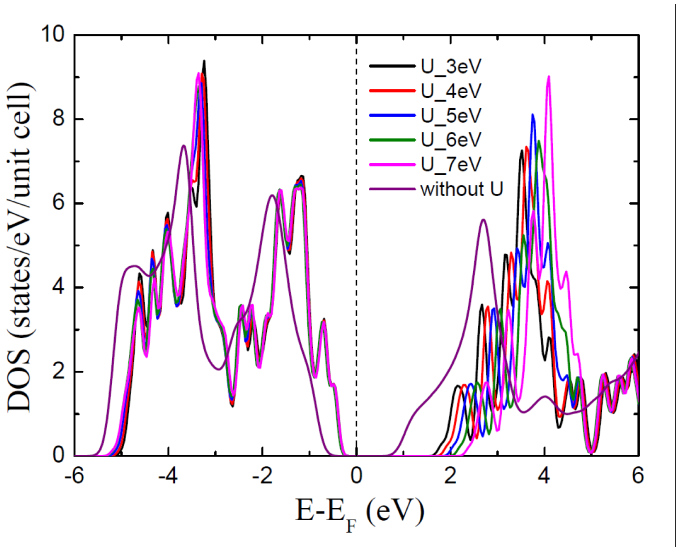

Fig. 2.12 : Band gap variation as a function of U.

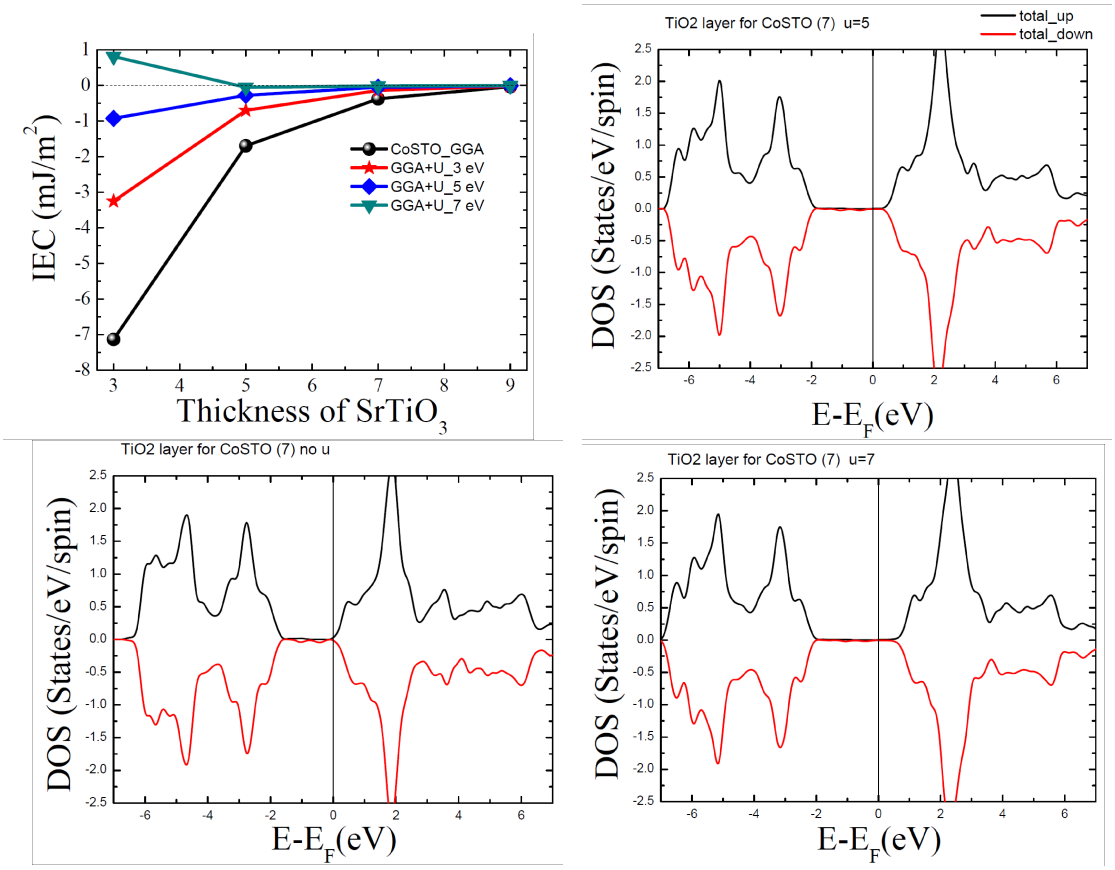

Fig. 2.13 : IEC for $[Co_5(STO)_x]_2$ as a function of STO thickness for different U. The density of states for the middle layer of STO are shown for 7 monolayer STO case.

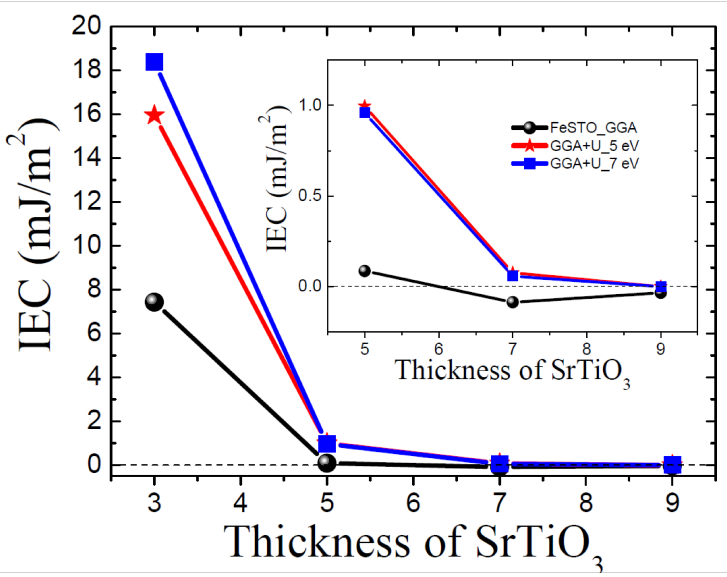

Fig. 2.14 : IEC for $[Fe_5(STO)_x]_2$ as a function of STO thickness for different U.

2.3.5 Conclusion

In this section, we have studied the IEC in $Co/SrTiO_3/Co$, $Fe/SrTiO_3/Fe$ and $Co(Fe)/SrTiO_3/Co(Fe)$ magnetic tunnel junctions. A DFT+U approach is used to vary the band gap of $SrTiO_3$. We demonstrated that both electrodes and spacers can strongly influence the interlayer exchange coupling. This is surprisingly consistent with the free electron model by P. Bruno [Bru95] or J. C. Slonczewski [Slo93], where the sign of the coupling is determined by the values of Fermi wave vectors in spacer $|k_F|$, and in magnetic electrodes, $k_F^{\uparrow}$ and $k_F^{\downarrow}$.

2.4 IEC in GaAs(ZnSe)-based MTJs

By varying the thickness of barrier to tune the occupied states at the Fermi energy, we show that the filling of Fermi level in the spacer will give an oscillatory interlayer exchange coupling, wile with empty state at the Fermi level, the exchange coupling shows no oscillatory character but decays exponentially as a function of spacer thickness.

2.4.1 Introduction

As we have already mentioned, interlayer exchange coupling (IEC) has been a subject of major interest for spintronic community both from fundamental and applications points of view, and the interest strongly increased when the AF IEC between ferromagnetic layers was also found across a semiconductor in Fe|Si|Fe [dVKdB$^+$97, HWSS02, GBD$^+$07] or an insulator in Fe|MgO|Fe crystalline magnetic tunnel junctions (MTJ) [FVTB$^+$02]. The IEC in Fe|MgO|Fe MTJs has already been studied and it has been shown that it strongly depends on oxidation conditions at the interface and barrier [KYV$^+$06, ZTV05, YCK$^+$10]. The MgO-based MTJs has been of great interest for spintronic community due to Bloch-states symmetry based spin filtering leading to huge TMR values. On another hand, the same spin filtering phenomenon has been also predicted for Fe|GaAs and Fe|ZnSe crystalline MTJs [VCB06, BZW$^+$97] but the IEC for these structures has rarely studied theoretically [HWV$^+$01].

2.4.2 Interfacial structure of Fe/GaAs(ZnSe)

As we have seen in Fe/MgO/Fe MTJs, the structural relaxation and oxidation conditions are crucial to understanding interlayer exchange coupling. Therefore, the interfacial mixing should also have impact on IEC behavior. The structure of Fe/GaAs or Fe/ZnSe interfaces have been studied by S. Vutukuri, et al. [VCB06]. Here we use the same interfacial model [Figure 2.15] [VCB06]. Figure 2.15 (a) is the atomically abrupt interface of bcc Fe and zinc-blende GaAs(ZnSe), which we call pure interface. Figure 2.15 (b) is the partially intermixed structure with one Fe atom filling the vacancy site in the GaAs (ZnSe) lattice, and Figure 2.15 (c) is the fully intermixed configuration, in which two Fe atoms filling the vacancy sites in the GaAs (ZnSe) lattice. For each model, we use five monolayers of Fe and vary the thickness of GaAs (ZnSe) from 2 to 9 layers. We define the thickness of GaAs (ZnSe) corresponding only to As (Se). For example, the 2 layers of GaAs contain 2 layers of As and 1 layer of Ga [Figure 2.16]. The calculation method and the calculation of IEC are the same as the calculations for IEC in Fe/MgO/Fe MTJs. Only difference is the energy cut off taken 400 eV here.

2.4.3 Correlation between IEC and the band gap in barrier

The calculated IEC for Fe/ZnSe/Fe/ZnSe as a function of ZnSe thickness is shown in Figure 2.17 (f). One sees that for thicknesses less than 4 layers, the coupling is oscillatory for all interfaces considered. For thicknesses larger than 4 layers, the coupling decays exponentially as a function of ZnSe thickness. To understand this phenomenon, we analyzed the density of states layer by layer in the barrier system as shown in Figure 2.17

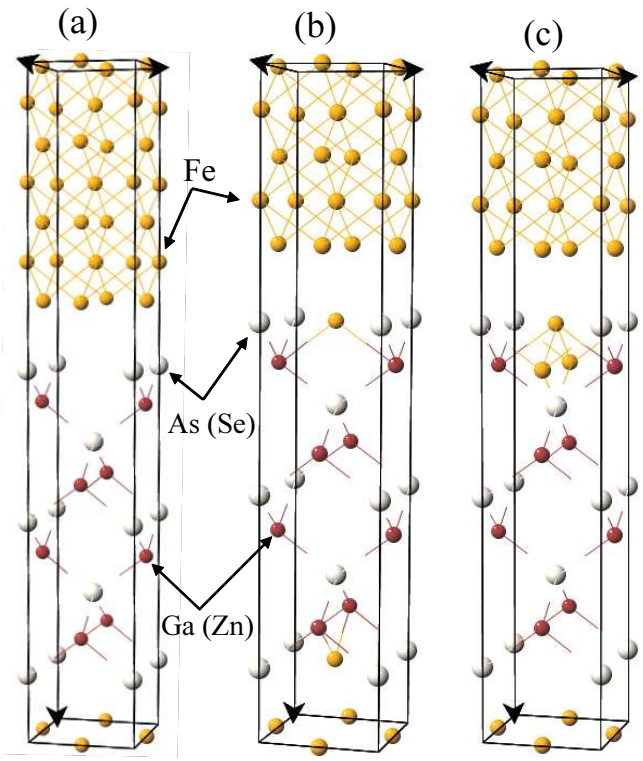

Fig. 2.15 : Interfacial structures of Fe/GaAs(ZnSe) for (a) pure, (b) partially-intermixed, and (c) fully-intermixed interfaces.

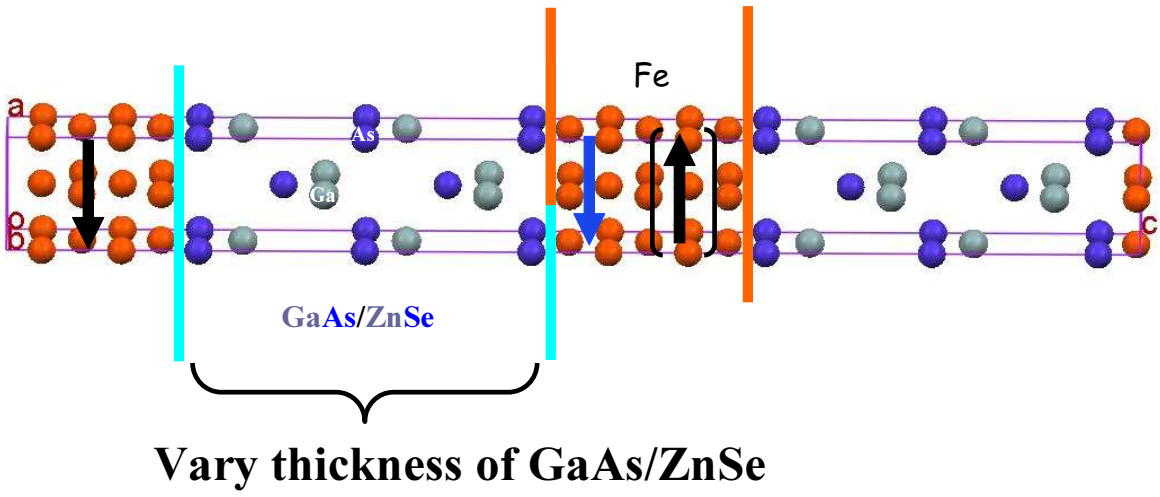

Fig. 2.16 : Schematic structure for calculation of IEC as a function of barrier thickness in Fe/GaAs(ZnSe)/Fe MTJs.

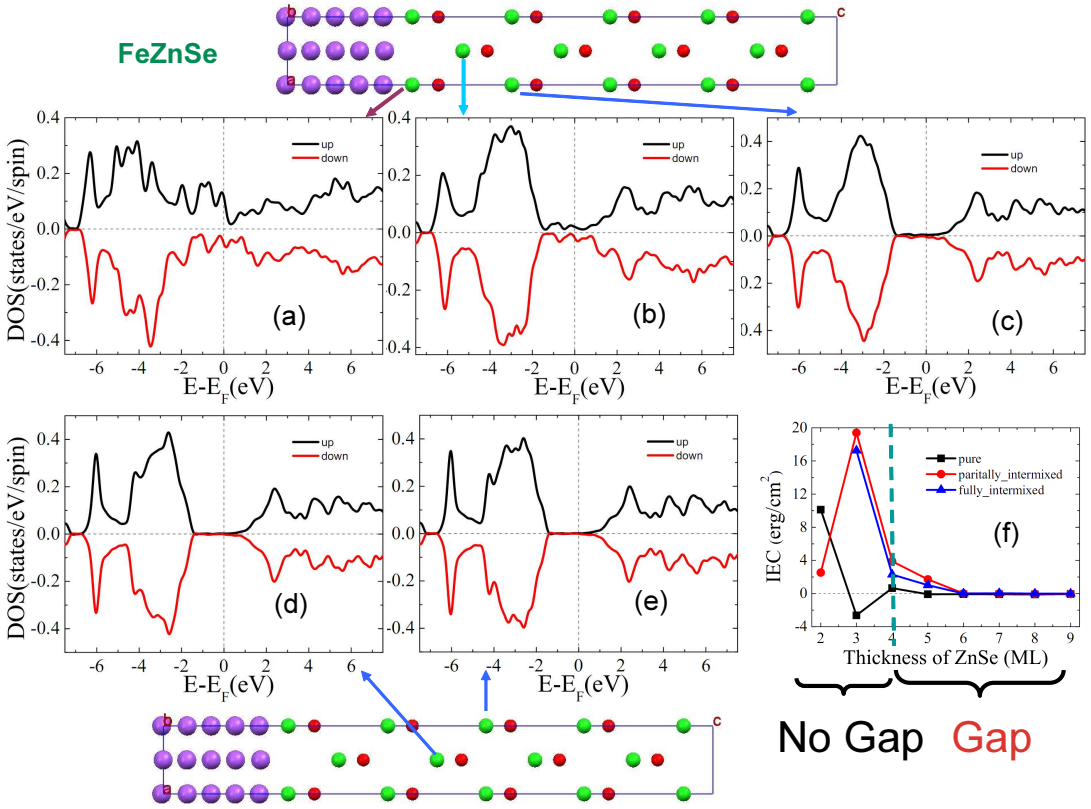

Fig. 2.17 : IEC for $[Fe_5ZnSe_x]_2$ as a function of ZnSe thickness and the density of states for different layers in ZnSe barrier.

(a)-(e). One can see that for the first, second and third layer of Se, there are some occupied states at the Fermi level, which means that the system is still 'metallic' up to 3 monolayer thickness, while starting from the fourth layer Se, the occupation at Fermi level is zero, which means that the system becomes 'insulating' for thickness larger than 4 monolayer. This explains that the coupling has RKKY type for the barrier thickness less than 3 monolayers. However, as long as there is gap appears in the barrier, the coupling will exponentially decay as barrier thickness increasing.

The situation is different regarding GaAs. One can see that the coupling is oscillating for all thicknesses considered as shown in Figure 2.18 (f). Similar analysis of the DOS in the barrier shows that there are still occupied states at the Fermi level until 9 layers of GaAs, as shown in Figure 2.18 (a)-(e). This is consistent with before that with no gap opening in the barrier, the coupling will be oscillatory.

The experimental results in $Fe/Fe_{1-x}Si_x/Fe$ junctions showed that for spacer thicknesses larger than 14 Å, with x=0.7, the coupling decays exponentially, and for thicknesses less than 14 Å, the coupling is oscillatory. At the same time, with x=1, the exponential decay IEC starts at 8 Å, and for x=0.8, the exponential decay IEC starts around 10 Å. Actually, the ratio between Fe and Si is playing the role of tuning the gap in the barrier: with more Si, the gap appears earlier, so exponential decay of IEC starts with thinner barrier thickness [BBC+03].

It is worth to note that DFT underestimates the band gap of GaAs and ZnSe. With

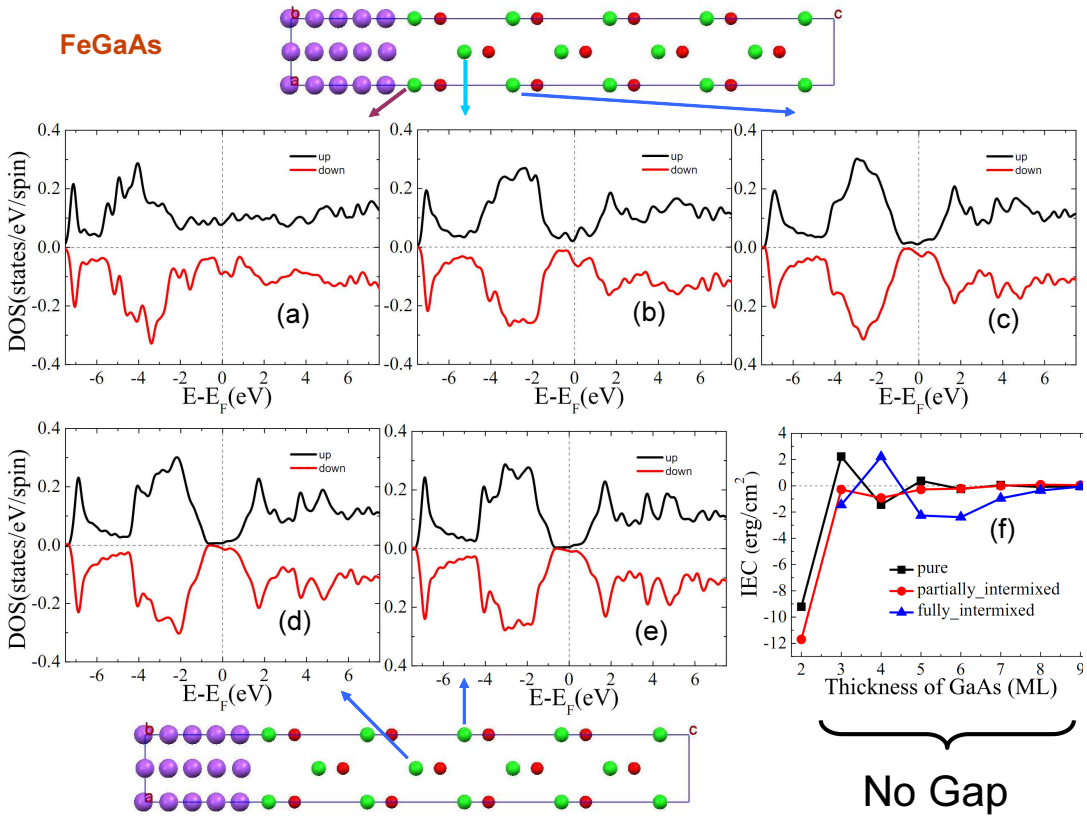

Fig. 2.18 : IEC for $[Fe_5GaAs_x]_2$ as a function of GaAs thickness and the density of states for different layers in GaAs barrier.

our calculation with GGA as exchange potential, the band gap of GaAs is 0.57 eV compared to 1.53 eV in experiments. For ZnSe, GGA gives a gap of 1.68 eV compared to the experimental value of 2.82 eV. For the correct band gap calculation, one may use GW corrections where the gaps of GaAs and ZnSe are 1.55 eV and 2.84 eV which are almost the same as experiments [SMK07].

Even though the band gap is not correctly estimated, the relation between IEC and band gap in the barrier should not change: when there are states occupying Fermi level the coupling will be oscillatory; when there is a gap in the barrier, the coupling will exponentially decay as a function of barrier thickness.

2.4.4 Conclusion

In conclusion, we have shown a general picture for the interlayer exchange coupling behavior related to the presence of states at Fermi level. When Fermi level in the spacer is not empty, the coupling will show a RKKY-like oscillatory character. Empty states at Fermi energy will lead to decay of IEC as a function of barrier thickness.

2.5 Summary

In this Chapter, we investigated the interlayer exchange coupling in Fe|MgO|Fe magnetic tunnel junctions. We showed that the interlayer exchange coupling across fully optimized pure Fe|MgO|Fe magnetic tunnel junctions is antiferromagnetic, and decays as a function of MgO thickness, which is in a good agreement with experimental results. Furthermore, a general trend of interlayer exchange coupling related to the oxidation conditions is given. The underoxidized structure enhances the antiferromagnetic coupling, in agreement with previous work, whereas overoxidization decreases it, and may even change the sign of interlayer exchange coupling to ferromagnetic, depending the oxygen concentration at interfaces.

Furthermore, we have investigated the interlayer exchange coupling in MTJs across $SrTiO_3$, GaAs and ZnSe spacers. In case of $SrTiO_3$-based MTJs, by changing the electrodes and barrier band gap (via the DFT+U approach) to vary the Fermi level position, we found a general relation between the sign of IEC and the Fermi level position in the band gap. This can be explained by the models of P. Bruno [Bru95] or J. C. Slonczewski [Slo93]. In case of GaAs and ZnSe having different band gap but the same crystal structure, oscillatory or exponentially decay IEC depends on the presence or absence of occupied states at the Fermi level within the spacer.

Chapter 3

Spin-orbit coupling induced phenomena at FM|MgO interfaces

It is well known from special relativity that the motion of an electron (a particle) in an electric field results in a kinematic effect in which part of the electric field is seen as a magnetic field in the electron's rest frame [Jac98]. The interaction of the electron spin with the electric field is called the spin-orbit interaction (SOI) or spin-orbit coupling (SOC), which has the general form,

$$\mathbf{H}_{SO} = \frac{\hbar}{4m_0^2c^2}\mathbf{p}\cdot(\sigma\times\nabla\mathbf{V}) \tag{3.1}$$

where m_0 is the free electron mass, c is the velocity of light, σ is a vector which components are the Pauli matrices, and V is the electric potential. In equation(3.1), $\mathbf{p}$ represents the canonical momentum. In presence of an external magnetic field $\mathbf{B}=\nabla\times\mathbf{A}$, $\mathbf{p}$ should be replaced by the kinetic momentum $\mathbf{P}=\mathbf{p}+e\mathbf{A}$. In the case of atoms, for example, the spin-orbit interaction refers to the interaction of the electron spin with the average Coulomb field of the nuclei and other electrons. In the case of crystal, spin-orbit interaction is determined by the interaction of the electron spin with the average electric field corresponding to the periodic crystal potential.

With SOI, Bloch states can be written as [Ell54],

$$\psi_{\mathbf{k},n\uparrow(\mathbf{r})} = [a_{\mathbf{k}n}(\mathbf{r})\ |\uparrow> + b_{\mathbf{k}n}(\mathbf{r})\ |\downarrow>]e^{i\mathbf{k}\cdot\mathbf{r}}, \tag{3.2}$$

$$\psi_{\mathbf{k},n\downarrow(\mathbf{r})} = [a^{\star}_{-\mathbf{k}n}(\mathbf{r})\ |\downarrow> - b^{\star}_{-\mathbf{k}n}(\mathbf{r})\ |\uparrow>]e^{i\mathbf{k}\cdot\mathbf{r}} \tag{3.3}$$

which will cause shifts in an electron's atomic energy levels due to electromagnetic interaction between the electron's spin and the nucleus's magnetic field. A simple picture is shown in Figure(3.1) for spin-orbit effects in semiconductor.

In the field of spintronics, SOI plays a major role in a wide class of physical phenomena both from fundamental and applications points of view [FMAE+07]. For instance, it is at the heart of basic magnetic phenomena such as Spin Hall effect, Rashba effect [BR84, ZFDS04] magnetocrystalline anisotropy [MAF09], and magnetization damping, etc.

In this chapter, we address from first-principles the mechanisms of perpendicular magnetic anisotropy at Fe|MgO interfaces as well as establish the correlation between

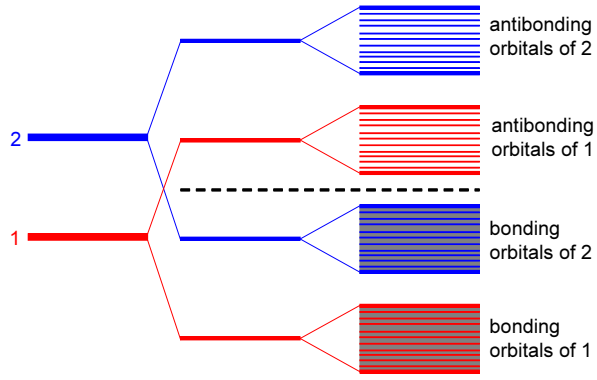

Fig. 3.1 : Schematics of the evolution of the atomic orbitals 1 and 2 into valence and conduction bands in a semiconductor.

Bloch states symmetry-based spin filtering and perpendicular magnetic anisotropy (PMA).

3.1 PMA at Fe(Co)|MgO interfaces

The perpendicular magnetic anisotropy arising at the interface between ferromagnetic transition metals and metallic oxides was investigated via first-principles calculations. In this section very large values of PMA, up to 3 erg/cm^2, at Fe|MgO interfaces are reported, in agreement with recent experiments. The origin of PMA is attributed to overlap between O-p_z and transition metal d_{z2} orbitals hybridized with d$xz(yz)$ orbitals with stronger spin-orbit coupling-induced splitting around the Fermi level for perpendicular magnetization orientation. Furthermore, it is shown that the PMA value weakens in the case of over- or under-oxidation due to the fact that oxygen p_z and transition metal d_{z2} orbital overlap is strongly affected by disorder, in agreement with experimental observations in magnetic tunnel junctions.

3.1.1 Introduction to the PMA at interfaces

Controlling SOI strength at the interface between ferromagnetic (FM) and non-magnetic layers represents an outstanding challenge for advancement of transport and magnetic properties of spintronic magnetic devices, such as perpendicular Magnetic Tunnel Junctions [MIP$^+$09, KSO$^+$08, DCR$^+$08, PPJ$^+$08, LKL05, NRAD09, YCD$^+$11] (p-MTJs) and tunneling anisotropic magnetoresistive (TAMR) systems [GJY$^+$07, PWW$^+$08]. Recently, electric field control of interfacial magnetic anisotropy has attracted much attention as well [SMN$^+$09, NAI$^+$10]. Traditionally, interfaces between magnetic and heavy non-magnetic transition metals such as Co|Pt [NKS$^+$98], Co|Pd [CMS85, DdJdB87], Co|Au [WWS$^+$94] have been used to obtain perpendicular magnetic anisotropy. It has been shown that the onset of the PMA at these interfaces is related to an increase of the orbital momentum of Co [WWS$^+$94] due to the strong hybridization between the 3d orbitals of the transition metal and the 5d orbitals of heavy metal [NKS$^+$98]. This hybridization enhances the energy splitting between the Co $3d_{z^2}$ and $3d_{x^2-y^2}$ orbitals and induces a charge transfer between the two layers [Bru89, DKS94a, KYA92]. As a result, the combination between SOI and hybridization-induced charge transfer leads to the PMA. Thus, the presence of a heavy non-magnetic layer (Pt, Pd, Au, W, Mo) was believed to be essential to obtain large PMA.

However, Monso et al have shown that PMA could be observed also at Co(Fe)|MOx interfaces (M=Ta, Mg, Al, Ru etc.) [MRA$^+$02, RAD$^+$03] in spite of the weak SOI at the interface. Surprisingly large PMA values up to 1 to 2 erg/cm^2 have been reported, which are comparable or even larger than the PMA observed at Co|Pt or Co|Pd interfaces [GLW$^+$06, JJKdB95]. This result is quite general and has been observed in both crystalline (MgO) or amorphous (AlOx) barriers, using both natural or plasma oxidation [LHA$^+$07, MDL$^+$08, MPV$^+$08]. The PMA could be dramatically improved under annealing [MPV$^+$08, RMD$^+$09a, NRAD09] and X-ray Photoemission Spectroscopy has demonstrated that the PMA could be correlated without ambiguity with the presence of oxygen atoms at the interface [LHA$^+$07, MPV$^+$08]. In fact, a correlation between PMA and oxidation conditions have been demonstrated for a wide range of FM|MOx including those based on Co_xFe_{1-x}, thus indicating that the phenomenon is quite general at interfaces between magnetic transition metals and oxygen terminated oxides. These

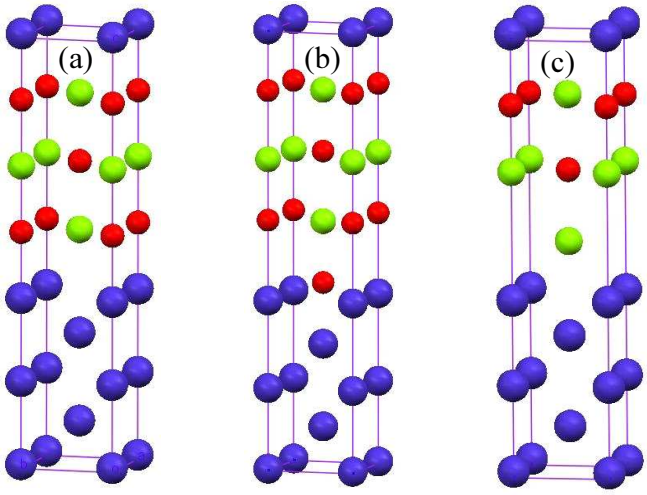

Fig. 3.2 : Schematics of the calculated crystalline structures for (a) pure, (b) over-oxydized and (c) under-oxydized geometries. Fe, Mg and O are represented by blue, green and red balls respectively.

observations led the authors to postulate that, in spite of the weak SOI of the elements (Fe, Co, Al, O), oxidation condition plays an essential role in the PMA, as they do in TMR [ZBB03] or interlayer exchange coupling (IEC) [YCK$^+$10]. Recent experiments reported large PMA values of 1.3 erg/cm^2 at CoFeB|MgO structures [IMY$^+$10, EKI$^+$10].

In this section, we report first-principles investigations of the PMA and the effect of interfacial oxidation conditions on the PMA at Fe|MgO(100) structures. The latter can be viewed as a model system for FM|MOx interfaces involving bcc electrodes including Co_xFe_{1-x} alloys. In agreement with experiments, it is demonstrated that despite the weak SOI, the bonding between the Fe-3d and O-2p orbitals can give rise to even stronger PMA than that of Co|Pt interfaces. The largest PMA value is obtained for ideal interfaces while it is reduced for the case of over- or underoxidized interfaces. In addition, it is found that the FM|MgO PMA strength decreases when Fe is replaced by Co, consistent with the recent report that the PMA values decrease in Co_xFe_{1-x}|MgO as the Co concentration increases [YKS$^+$09].

3.1.2 Methodology and structures

For the *ab inito* calculations, Vienna *ab initio* simulation package (VASP) [KH93, KF96a, KF96b] was used with generalized gradient approximation [WP91] and projector augmented wave potentials [Blo94, KJ99]. The calculations were performed in three steps. First, the calculations were performed for both unrelaxed and relaxed structrures. In the case of relaxed structures, full structural relaxation in shape and volume was performed until the forces become smaller than smaller than 0.001 eV/Å for determining the most stable interfacial geometries. Next, the Kohn-Sham equations were solved with no spin-orbit interaction taken into account to find out the charge distribution of the system's ground state. Finally, the spin-orbit coupling was included and the total energy of the system was determined as a function of the orientation of the

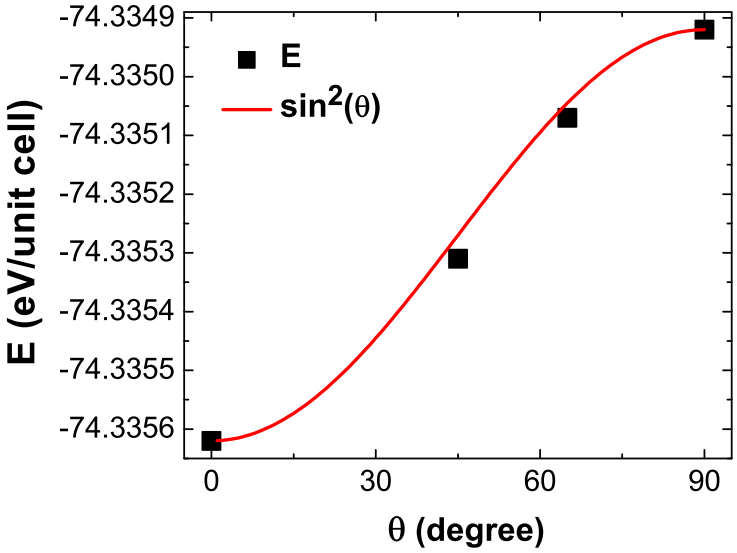

Fig. 3.3 : Angular dependence of the magnetic energy, where θ is the angle between the magnetization direction and the normal to the interface plane.

magnetic moments. A 19×19×3 K-point mesh was used in our calculations with the energy cut-off equal to 520 eV. Three structures were considered as shown in Figure 3.2: (a) "pure" (O-terminated) interface, (b) over-oxidized interface (with O inserted at the interfacial magnetic layer), and (c) under-oxidized (Mg-terminated) interface. The relaxed structures have been reported in our previous work [YCK$^+$10]. We point out that the situation of "pure" interface is the most stable one as observed in annealing experiments [MPV$^+$08, RMD$^+$09a]. The most stable location for the oxygen atoms is on top of metal ions due to strong overlap between Fe-3d and O-2p orbitals. Correlatively, it is interesting to note that this structural configuration also yields the spin filtering phenomenon based on Bloch states symmetry leading to high TMR values [BZSM01, MU01]. Furthermore, the strong hybridization significantly modifies the band structure giving rise to a high interfacial crystal field [Bru89].

3.1.3 Results and discussion

In Figure 3.3, we present the calculated energy per unit cell as a function of the angle θ between magnetization orientation and normal to the plane for pure *unrelaxed* Fe|MgO interface. The dependence is well fitted by the conventional uniaxial anisotropy expression $E_A = K_0 + K_2 \sin^2\theta$, where $K_2 = 0.7$ meV/atom ($K_2 = 1.36$ erg/cm^2). Interestingly, the perpendicular surface anisotropy in this case is stronger than that of Co|Pt [GLW$^+$06, JJKdB95] in agreement with recent experiments [IMY$^+$10]. The calculated anisotropy value is further enhanced for relaxed structures [as shown in Table 3.1], reaching the very large value of almost 3 erg/cm^2 for the structure with three MgO monlayers shown in Figure 3.2(a). It is interesting to note that the PMA is not strongly affacted when the MgO thickness is increased up to 11 monolayers,

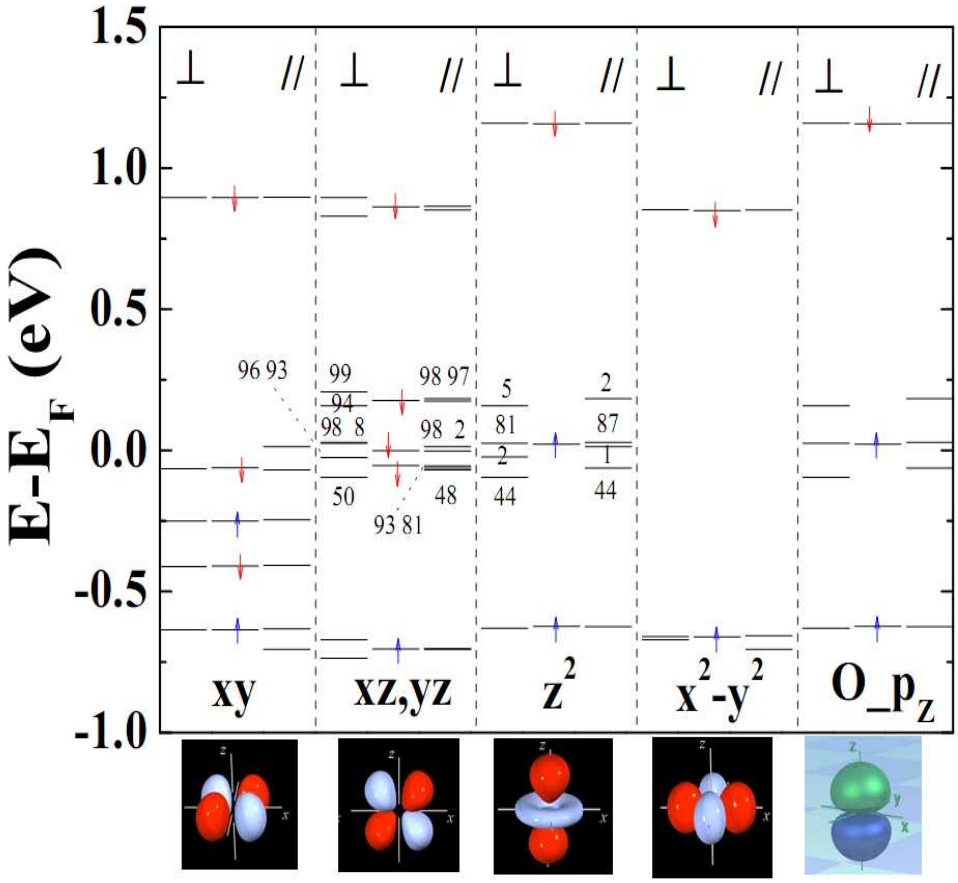

Fig. 3.4 : Spin-orbit coupling effects on wave function character at $\bar{\Gamma}$ point of interfacial Fe d and neighbor oxygen p_z orbitals for pure Fe|MgO interface shown in Figure 3.2a. Three subcolumns in each column show the band levels for out-of-plane(left) and in-plane(right) orientation of magnetization as well as for the case with no spin-orbit interaction included(middle), respectively. Numbers are the percentage of the orbital character components within Wigner-Seitz spheres around interfacial atoms.

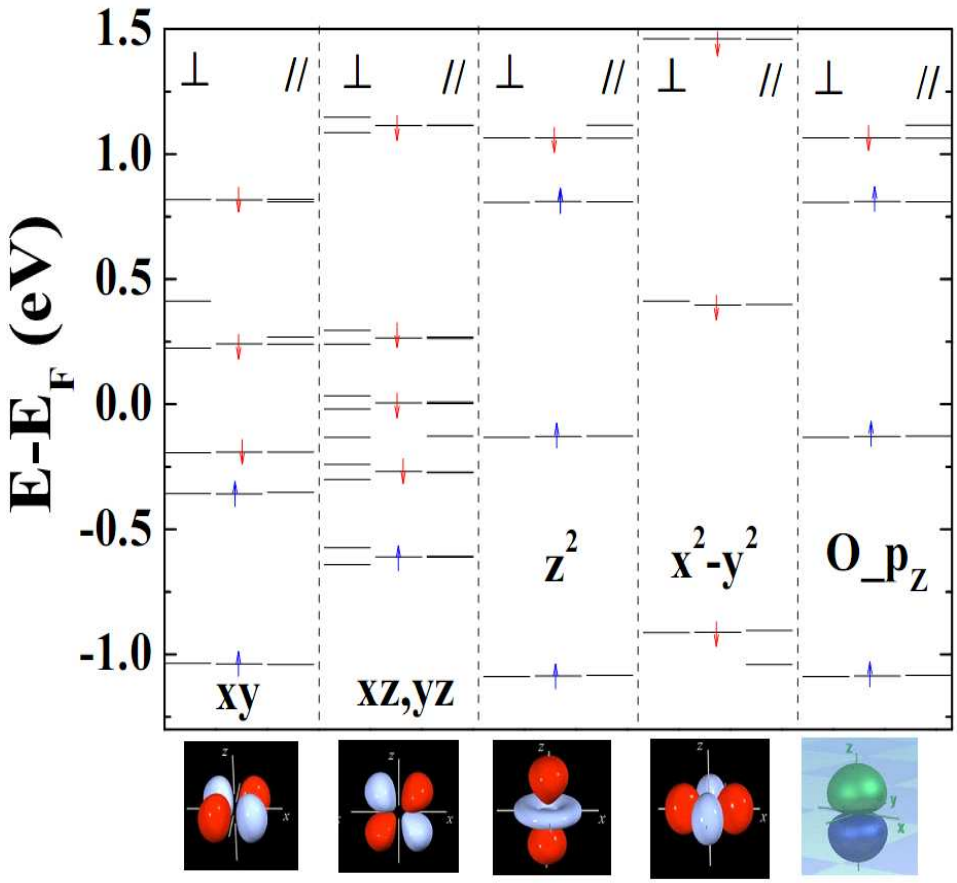

Fig. 3.5 : The same as Figure 3.4 for over-oxidized Fe|MgO interface.

giving the calculated value of 3.15 erg/cm^2[Table 3.1], which provides a good agreement with recent experiment [YKI$^+$11]. The PMA for relaxed Fe|MgO structures weakens in case of interfacial disorder and becomes equal to 2.27 and 0.93 erg/cm^2 for under- and overoxidized cases, respectively (see Table 3.1), indicating that the oxidation condition plays a critical role in PMA as it does in both TMR [ZBB03] and IEC [YCK$^+$10]. If replacing Fe by Co, the PMA value decreases down to 0.38 erg/cm^2 [Table 3.1], which agrees with Yakata's report that Fe-rich FeCoB top free layers in $Co_{60}Fe_{20}B_{20}$|MgO|$(Co_xFe_{1-x})_{80}B_{20}$ MTJs exhibit larger PMA than their Co-rich counterparts [YKS$^+$09]. Furthermore, the tendency of PMA to decrease with oxygen excess or deficit along the metal/oxide interface is consistent with the experimental observations of PMA dependence on annealing temperature and oxydation conditions [NRAD09, NRD$^+$10]. It was reported that with higher annealing temperatures, PMA increases due to interfacial quality improvement [NRAD09]. Furthermore, when varying the oxidation or annealing conditions, it was observed that the PMA reaches a maximum value for the same conditions at which the TMR ratio also gets maximized indicating that ideal interfaces are crucial also for PMA observation [NRD$^+$10].

Table 3.1: PMA value(mJ/m^2) and magnetic moment m(μ_B per Fe(Co) atom) for different layers of Fe(Co) in Fe(Co)|MgO MTJs with different oxidation conditions.

		PMA	$m_s(\mu_B)$		
		(mJ/m^2)	interfacial	sublayer	bulk
$Fe_7[MgO]_{11}$	pure	3.15	2.77	2.55	2.52
(MTJs)	under-	2.53	2.18	2.41	2.49
	over-	2.28	3.36	2.61	2.51
$Fe_7[MgO]_{11}$	pure	2.73	2.75	2.54	2.49
(vacuum)	under-	2.10	2.11	2.39	2.45
	over-	-0.33	3.37	2.67	2.52
Fe_7|(vacuum)		0.87	2.96	2.37	2.33
	pure	2.93	2.73	2.54	2.56
$Fe_5[MgO]_3$	under-	2.27	2.14	2.41	2.55
	over-	0.98	3.33	2.70	2.61
	pure	0.38	1.67	1.84	1.60
$Co_5[MgO]_3$	under-	1.56	1.35	1.81	1.63
	over-	0.78	2.24	1.88	1.82

In Table 3.1 we give also the evolution of interfacial Fe magnetic atomic moments as a function of distance from the interface. One can see that compared to the pure case, the moments are enhanced(weakened) for over(under)oxidized interfaces.

Let us now proceed with the explanation of the physical origin of the results obtained from first principles on the effect of oxidation conditions on PMA. To understand the PMA origin at Fe|MgO interfaces, we performed detailed analysis of the impact of spin-orbit interaction on electronic band structure with out-of-plane (d_{z^2}, d_{xz}, d_{yz}) and in-plane ($d_{x^2-y^2}$, d_{xy}) Fe-3d and O-p_z orbitals character.

We start from the analysis for pure interfaces represented in Figure 3.2a. In Figure 3.4, we show bands around the Fermi level E_F at $\bar{\Gamma}$-point with orbital and interfacial atoms projected wave function character for out-of-plane (left) and in-plane (right) orientation of the magnetization as well as in the absence of spin-orbit coupling (middle). Let us concentrate on band levels in the immediate vicinity of the Fermi level. When no SOI is included (middle subcolumns), there are several double degenerated band levels with d_{xz} and d_{yz} character which represent the minority Bloch state with $\Delta_5(p_x,p_y,d_{xz},d_{yz})$ symmetry. At the same time, there is a band level resulting from hybridization between Fe-d_{z^2} and O-p_z orbitals which is a signature of majority Bloch state with $\Delta_1(s,p_z,d_{z^2})$ symmetry for Fe and MgO which is at the heart of the spin filtering phenomenon causing enhanced TMR values in MgO based MTJs [BZSM01]. When spin-orbit interaction is switched on, the picture is strongly modified. Firstly, one can clearly see that the degeneracy is lifted for energy levels with $d_{xz,yz}$ orbital character. Secondly, these levels become hybridized with Fe d_{z^2} resulting in appearance of additional levels of both d_{z^2} and $d_{xz,yz}$ orbital character represented by numbers showing percentage of the corresponding orbital character components within Wigner-Seitz spheres (see Figure 3.4). In particular, for the out-of-plane magnetization orientation (left subcolumns), the additional d_{z^2} levels with 5, 2 and 44 percentage originate from $d_{xz,yz}$ orbital character due to SOI. For

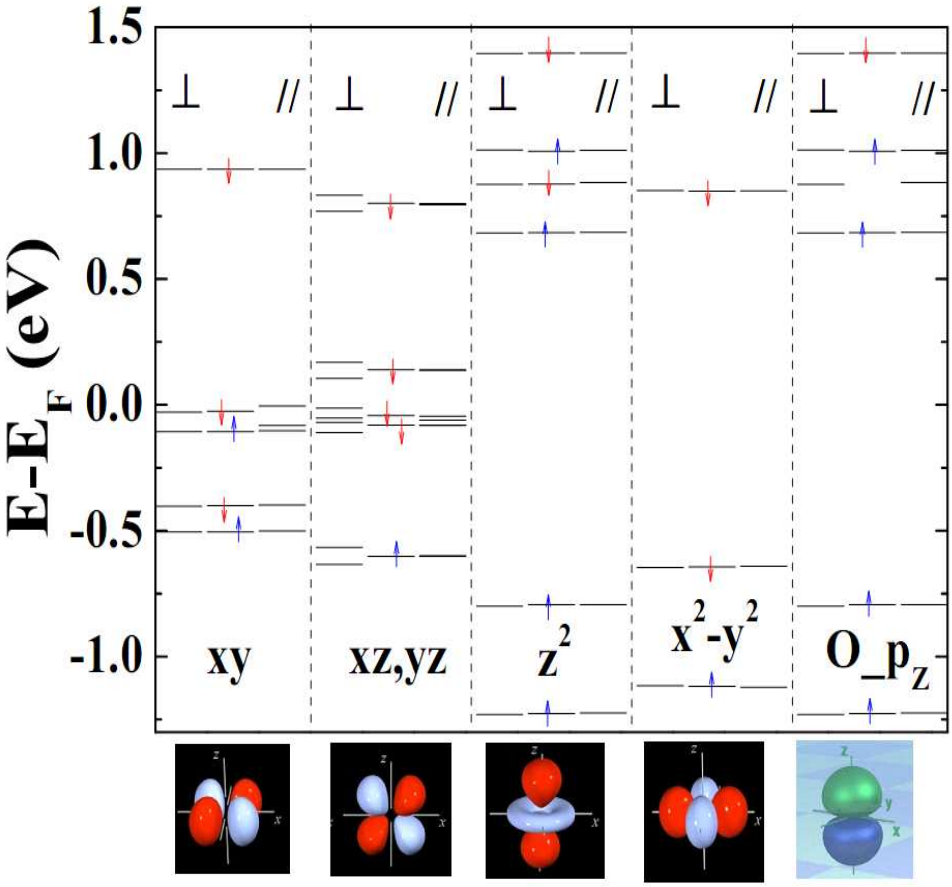

Fig. 3.6 : The same as Figure 3.4 for under-oxidized Fe|MgO interface.

the same reason, the additional $d_{xz,yz}$ band with 8 percents comes from d_{z^2} orbital. Furthermore, since the Fe-d_{z^2} orbital has already been hybridized with O-p_z being a part of the Δ_1 Bloch state, the additional energy levels with O-p_z character also appeared with SOI switched on. All this mechanism can be seen as the spin-orbit induced mixing between majority Δ_1 and minority Δ_5 Bloch states which, of note, may affect observation of predicted high TMR ratios in MTJs [VRS$^+$10]. Finally, the hybridized band levels with d_{z^2}, d_{xz}, d_{yz} and p_z character are lower in energy with a larger splitting for out-of-plane magnetization orientation compared to the in-plane one as clearly seen in left and right subcolumns in Figure 3.4, respectively. Thus, the lift of degeneracy of d_{xz} and d_{yz} orbitals, combined with hybridizations between $d_{xz,yz}$ and d_{z^2}, Fe-d_{z^2} and O-p_z orbitals is at the origin of perpendicular magnetic anisotropy for pure Fe|MgO interfaces. This result shows that the out-of-plane components of $d_{xz,yz}$ orbitals plays a crucial role for PMA similarly to Co|Pd interfaces [WWF93].

Next, we proceed with the same analysis for under- and over-oxidized Fe|MgO interfaces represented in Figure 3.2(b) and (c), respectively. As shown in Figure 3.5 for the case with an additional oxygen located at the Fe|MgO interface (Figure 3.2(b)), spin orbit coupling lifts again the degeneracy for states with $d_{xz,yz}$ causing stronger splitting and deeper level position for out-of-plane orientation of magnetization compared to the in-plane one. However, the number of mixed states with both Fe-d_{z^2} and O-p_z orbitals is reduced due to local charge redistribution induced by additional oxygen atoms [ZBB03]. Since d_{z^2} and p_z orbital hybridization which is one of the main causes for PMA is not splitted, the anisotropy is significantly reduced.

A different picture occurs in case of underoxidized Fe|MgO interface represented in Figure 3.2(c). As shown in Figure 3.6, the Fe-d_{z^2} and O-p_z components around the Fermi-level are now absent. As a result, the degeneracy lift induced by spin-orbit interaction for states with $d_{xz,yz}$ character is now solely responsible for the PMA. Since the splitting of these $d_{xz,yz}$ orbitals is still relatively strong and higher for out-of-plane magnetization orientation compared to the in-plane one, anisotropy values are higher compared to over-oxidized case but lower compared to the ideal Fe|MgO interfaces. Thus, the PMA reaches its maximum for ideal interfaces.

When no SOI is included (middle subcolumns in Figure 3.10, the band level resulting from hybridization between Fe-d_{z^2} and O-p_z orbitals is present. The double degenerated bands with Δ_5 symmetry related to minority Fe are also present close to the Fermi level. When spin-orbit interaction is switched on, the degeneracy is lifted and majority Δ_1 and minority Δ_5 are mixed up producing bands with both symmetry characters. As a result, band levels with d_{z^2}, $d_{xz(yz)}$ and p_z character split around the Fermi level and this splitting is larger and the lowest band deeper for out-of-plane magnetization orientation as clearly seen in left and right subcolumns in Figure 3.10 (b), respectively. Thus, the lift of degeneracy of dxz and dyz orbitals, combning the hybridization between $d_{xz(yz)}$ and d_{z^2}, as well as their mixing with Fe-d_{z^2} and O-p_z orbitals are at origin of perpendicular magnetic anisotropy for pure Fe|MgO interfaces

For Co|MgO case, the anisotropy value is reduced to 0.38 mJ/m^2 [shown in Table 3.1]. To understand this, we did the same band spectrum analysis for Co|MgO interface [Figure 3.7(a)]. For comparison, we plot the band spectra of Fe|MgO in Figure 3.7(b). One can see that SOI lifts the degeneracy for states with $d_{xz(yz)}$ causing stronger splitting and deeper level position in case of out-of-plane orientation of magnetization compared

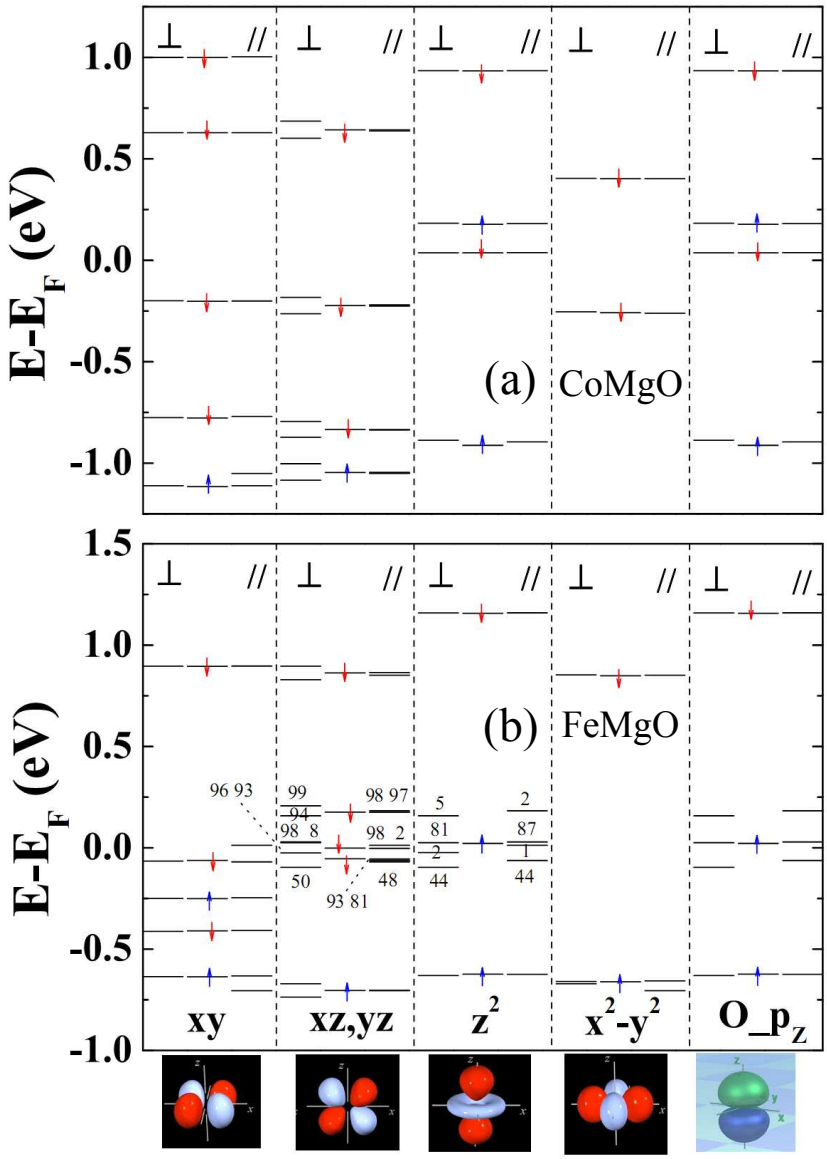

Fig. 3.7 : Spin-orbit coupling effects on wave function character at $\bar{\Gamma}$ point of interfacial Co(Fe)-d and neighboring oxygen p_z orbitals for pure $Co_5[MgO]_3$ (a) and $Fe_5[MgO]_3$ (b), respectively. Three subcolumns in each column show the band levels for out-of-plane(left) and in-plane(right) orientation of magnetization as well as for the case with no spin-orbit interaction included(middle), respectively. Numbers are the percentage of the orbital character components within Wigner-Seitz spheres around interfacial atoms.

to the in-plane one. However, these states are far away to the Fermi level and are not hybridized with Co-d_{z^2} and O-p_z orbitals, as well as there is no splitting of d_{z^2} and p_z orbitals, thus the perpendicular magnetic anisotropy is significantly reduced compared to that of Fe|MgO interfaces.

3.1.4 Conclusion

In conclusion, we presented *ab initio* studies of perpendicular magnetic anisotropy at Fe|MgO and Co|MgO interfaces as a function of the oxygen content along the interface. The PMA values are higher in the case of pure at Fe|MgO interfaces in agreement with recent experimental studies [IMY$^+$10, NRD$^+$10] and may reach up to 3 erg/cm^2 for relaxed interfaces. The origin of the large PMA is ascribed to combination of several factors: the degeneracy lift of out-of-plane 3d orbitals, hybridizations between $\Delta_1(d_{z^2})$ and Δ_5-like(d_{xz} and d_{yz}) 3d orbitals induced by spin-orbit interactions and hybridizations between Fe-3d and O-2p orbitals at the interface between the transition metal and the insulator. The PMA amplitude degrades in the case of over- or underoxidized interfaces in agreement with recent experiments [NRAD09, NRD$^+$10]. This is due to the impact of splitting(disappearing) of Δ_1-like hybridized states around the Fermi level in presence(absence) of additional oxygen atom. In addition, the PMA value is lower in the case of Co|MgO interface, which agrees with experiment that Fe-rich $Co_xFe_{1-x}B$|MgO structures have larger PMA than their Co-rich counterparts [YKS$^+$09].

3.2 Correlation between Bloch state spin filtering and PMA

In this section, we used much thicker MgO spacers and magnetic electrodes to study the correlation between Bloch state spin filtering and perpendicular magnetic anisotropy. In Fe(Co)|MgO|Fe(Co) MTJs, the TMR ratio will reach its maximum in case of interface is ideal, this is also true for the perpendicular magnetic anisotropy. The mechanism responsible for these phenomena is studied. From the band structure analysis we explicitly demonstrate the main contribution to the PMA originates from the Δ symmetry bands, which are well-known to be responsible for the Bloch state symmetry based spin filtering leading to large TMR ratios.

3.2.1 Introduction

We have mentioned in Chapter 1 that MgO-based magnetic tunnel junctions made a breakthrough for spintronic applications [MZBW99, BZSM01, MU01, WMZ$^+$02, PKP$^+$04, YNF$^+$04, Ike08, LHI$^+$07]. The mechanism responsible for large TMR ratio in Fe|MgO, Co|MgO, or FeCoB|MgO is the Bloch-states-symmetry-based spin filtering effect [BZSM01, MU01, DMW$^+$02, BZV$^+$05, VCB06], where the Δ symmetry bands play the crucial role.

Besides large PMA at FM|MgO interfaces, it was also demonstrated experimentally that there is a strong correlation between PMA and TMR maxima, i.e. they are obtained at the same optimal oxidation and annealing conditions [NRD$^+$10].

In this section, we report systematic studies of the correlation between PMA and TMR in terms of oxidation conditions and provide with underlying mechanisms responsible for such correlation.

3.2.2 Structures, results and discussion

The calculations are the same as in the first section of this Chapter. But the structures here are MTJs with 7 monolayers of Fe and 11 monolayers of MgO as shown in Figure 3.8 for (a) "pure" (O-terminated) interface, (b) over-oxidized interface (with O inserted at the interfacial magnetic layer), and (c) under-oxidized (Mg-terminated) interface.

In order to understand the correlation between PMA and TMR, we have plotted the wave function character of Δ_1 Bloch state as a function of the position across the supercells used for PMA calculations for the $Fe_5[MgO]_3$ [Figure 3.9] and $Fe_7[MgO]_{11}$ [Figure 3.10], respectively. One can clearly see that the Δ_1 decay rate is strongly enhanced in the case of overoxidized interface compared to the ideal one. There is no Δ_1 band around the Fermi level for underoxidized case as demonstrated above. This explains why both PMA and TMR reach their maximum values in a correlated way as observed experimentally [NRD$^+$10], this maximum being reached for ideal interfaces.

The reason for TMR ratio decreasing in case of overoxidized Fe|MgO|Fe magnetic tunnel junctions has been discussed by Zhang, et al. [ZBB03], where the additional oxygen at Fe|MgO interface weakens the overlap between O-P_z and Fe-d_{z2}. That is consistent with our analysis above that with additional oxygen at Fe|MgO interface, Δ_1 symmetry bands are strongly affected.

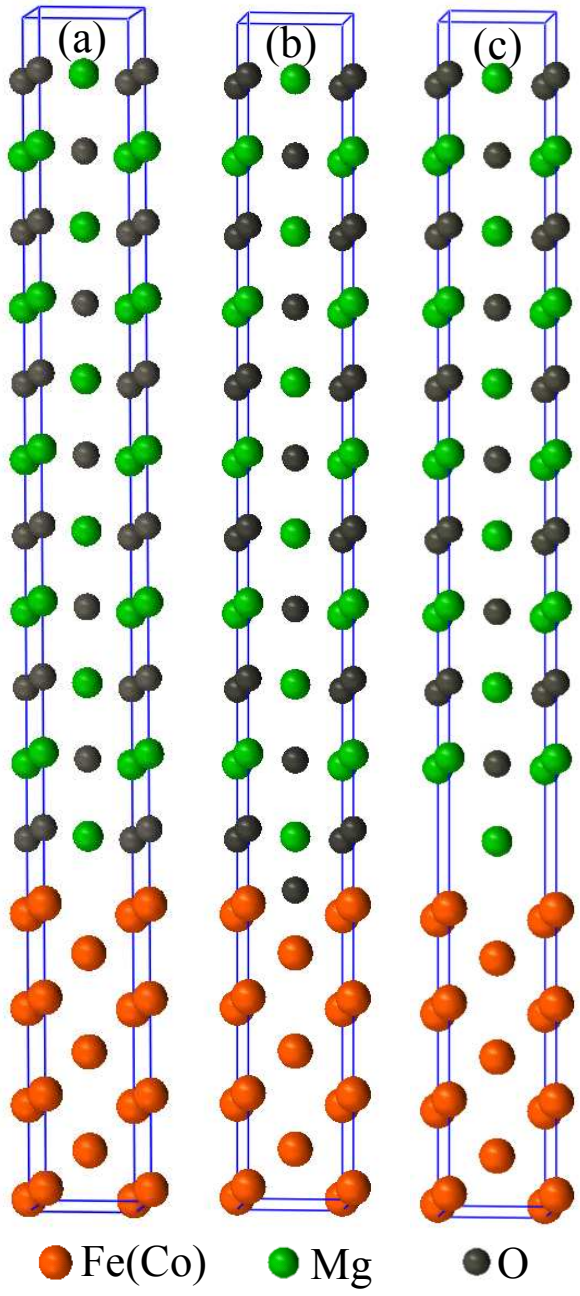

Fig. 3.8 : Schematics of the calculated crystalline structures for (a) pure, (b) overoxidized, and (c) underoxidized Fe(Co)|MgO magnetic tunnel junctions. Fe(Co), Mg and O are represented by red, green and dark balls respectively.

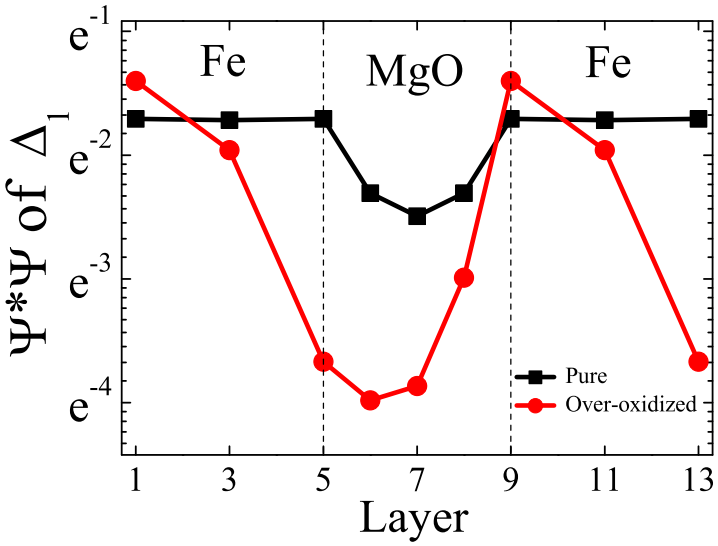

Fig. 3.9 : Δ_1 Bloch state character at $\bar{\Gamma}$-point around the Fermi level as a function of layer number in pure and over-oxidized Fe|MgO interfaces shown in Figure 3.2(a) and (b), respectively. Δ_1 Bloch state is absent around Fermi level in underoxidized case shown in Figure 3.6.

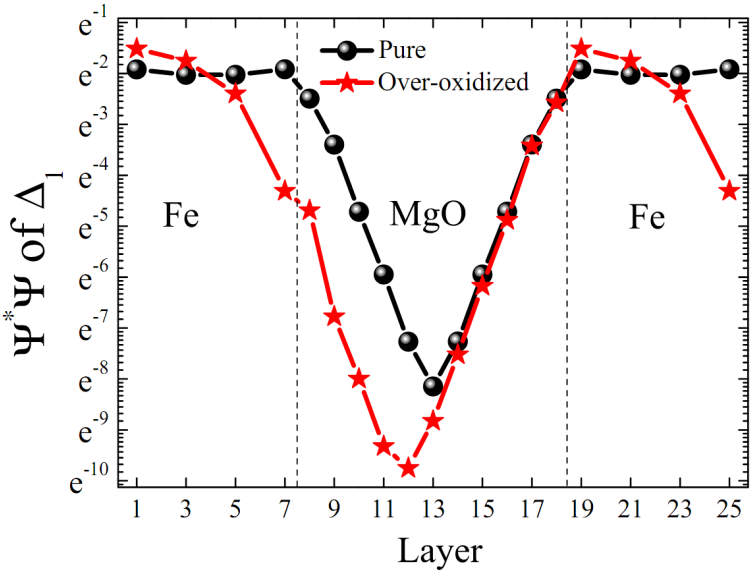

Fig. 3.10 : Δ_1 Bloch state character at $\bar{\Gamma}$-point around the Fermi level as a function of layer number in pure (black ball) and over-oxidized (red star) interfaces shown in Figure 3.8(a) and (b), respectively.

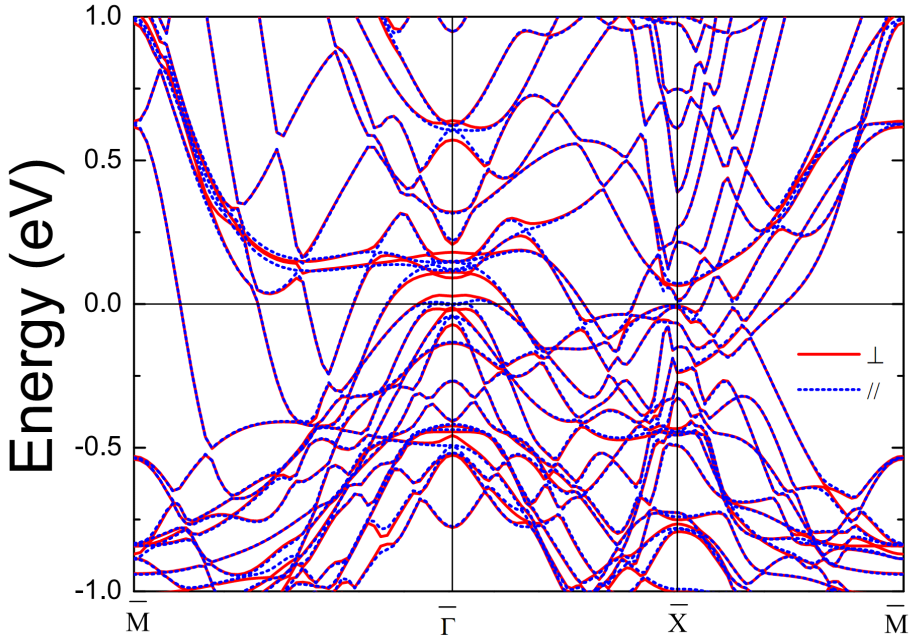

Fig. 3.11 : Band structure of pure $Fe_7[MgO]_{11}$ MTJs in case of out-of-plane (red solid) and in-plane (blue dish) orientation of Fe moment when spin-orbit interaction is switched on.

To further understand the underlying mechanism, we performed detailed analysis of the impact of spin-orbit coupling on band structure in case of out-of-plane and in-plane orientation of Fe moments as shown in Figure 3.11. One can see that degeneracy lift appeared mainly around $\bar{\Gamma}$ point which demonstrates that influence from spin-orbit coupling on Bloch states around Fermi level along Γ-H ($\bar{\Gamma}$ is the Γ-H projection) direction plays a crucial role for PMA origin.

3.2.3 Conclusion

In conclusion, we clarified the mechanisms responsible for large PMA at Fe|MgO MTJs and degradation in the case of Co|MgO MTJs. Furthermore, we revealed a strong correlation between underlaying mechanisms responsible for PMA and Bloch states symmetry based spin filtering, which paves the way for spintronic applications.

3.3 Summary

In this chapter, we first studied the mechanisms responsible for the large large perpendicular magnetic anisotropy at Fe|MgO interfaces in view of Bloch states symmetry-based band spectra analysis. We showed that the PMA are mainly caused by: (i) the spin-orbit coupling with out-of-plane quantization orientation axis causes larger splitting for the degenerated Δ_5 $[d_{xz(yz)}]$ symmetric orbitals compared to those in case of SOC with in-plane quantization orientation axis; (ii) the hybridization between d_{z2} and $d_{xz(yz)}$ enhances the effect from degeneracy lift of Δ_5 symmetric orbitals; and (iii) the hybridization between Fe-3d_{z2} and O-2p_z orbitals further enhances the effect from (ii). Indeed, this also explains the weakening of the PMA in case of contaminated Fe|MgO interfaces.

Next, we demonstrated a correlation between Bloch states symmetry based spin filtering and PMA. It shows that PMA and TMR can reach their maximum in case of ideal interfacial junctions, the underlying mechanism responsible for this is unveiled: both PMA and TMR origin from the same Bloch states.

Chapter 4

Graphene on magnetic metal

4.1 Perpendicular Magnetic Anisotropy of Co on Gr

As discussed in previous chapter, interfaces between magnetic and heavy non-magnetic transition metals such as Co|Pt [NKS+98], Co|Pd [CMS85, DdJdB87], and Co|Au [WWS+94] are used to obtain perpendicular magnetic anisotropy (PMA). Since hexagonal close packed (hcp) or face centered cubic (fcc) Co crystal lattices have very small mismatch with graphene, plus graphene has so many unique properties, here we investigate the PMA of Graphene|Co system. Furthermore, we provided a comparison study of the work function between graphene|Co to vacuum|Co interfaces. It is found that the graphene|Co interface strongly decrease the work function of vacuum|Co system, which are in a good agreement with experimental results.

4.1.1 Introduction

As we have mentioned in the general introduction, graphene has so many promising properties [CNGP+09, Gei09, DSAHR11] and has been proposed for spintronics devices. The application of graphene into spintronics therefore forms a new branch of topics, named graphene-based spintronics or graphene spintronics. One fundamental research of graphene spintronics is to induce spin-polarization in graphene by using substrates [KGK+07, TJP+07a, YP09, TJP+07b, HWP+09, HPM+10, YBV+11]. Well studied metal substrates are Co and Ni [VSBS+08, WRH+10, RVSB+09, VVKBY+10]. This is because graphene and Co or Ni has a very small lattice constant mismatch. Even though, Co|graphene system has been intensive studied, one very interesting topic, the magnetic anisotropy at Co|graphene interfaces is seldom studied [VVKBY+10].

In this chapter, we study the role of graphene on PMA and work function behavior on Co surfaces.

4.1.2 Methodology

We used again the Vienna *ab initio* simulation package (VASP) [KH93, KF96b, KF96a] with the generalized gradient approximation (Perdew-Burke-Ernzerhof) [KJ99] and projector augmented wave potentials [Blo94]. The calculations were performed in two steps. First, out-of-plane structural relaxation was allowed and the Kohn-Sham

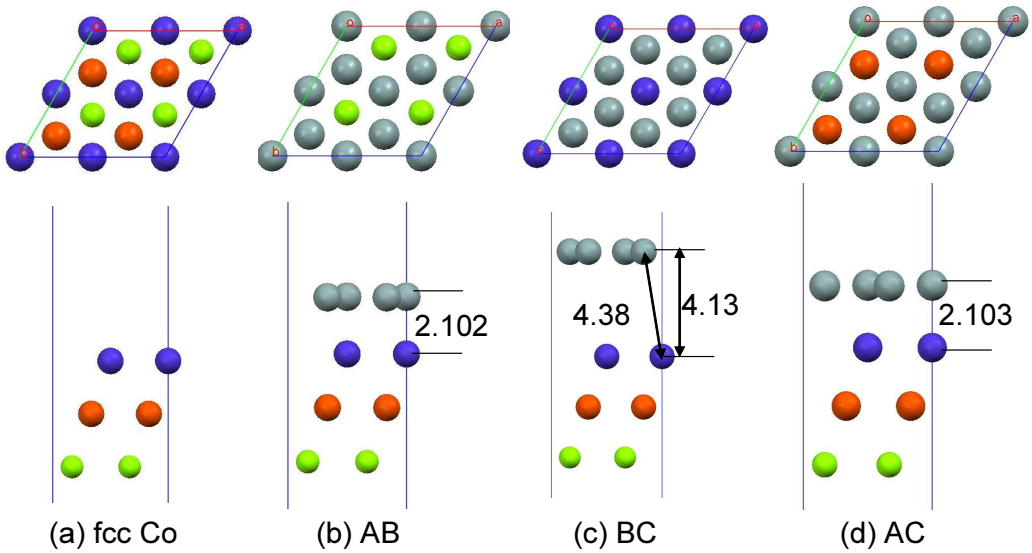

Fig. 4.1 : Top view (upper panels) and side view (lower panels) of calculated crystalline structures for (a) pure fcc Co film, (b) Graphene on top of AB sites, AB-Gr|Co(fcc), (c) Graphene on top of BC sites, BC-Gr|Co(fcc), and (d) Graphene on top of AC sites, AC-Gr|Co(fcc) structures. Co atoms in the 1st(A site), 2nd(B site) and 3rd(C site) layers are represented with blue, red and green balls, respectively. Carbon atoms are indicated with gray balls. The distances between graphene and Co substrates are labeled.

equations solved with no spin-orbit interaction taken into account for determining the most favourable adsorption geometry of graphene on Co. Then the spin-orbit coupling was included and the total energy of the system was determined as a function of the orientation of the magnetic moments. The k-point mesh used in all calculations is 15×15×1. The energy cutoff was set to 520 eV. The atomic structures are relaxed until the forces are smaller than 0.001 eV/Å. For the anisotropy calculations, the total energies are converged to 10^{-7} eV.

4.1.3 Stability of epitaxial graphene on Co films

Let us start from the possible structures and their stabilities for graphene on Co films. Co can form hcp, fcc and bcc crystal structures. Among these, hcp structure is the ground phase, while bcc structure is not stable and it is not of good match with graphene honeycomb lattice. In this chapter, we consider only Co fcc and hcp structures.

When graphene is formed on thick (more than three layers) Co substrates, the substrate can have fcc or hcp structure. According to the symmetry of stacking, there are three high symmetry structures as shown in Figure 4.1 and Figure 4.2 for fcc and hcp substrates, respectively, where the two carbon atoms of graphene are located on top of fcc Co lattice A and B, B and C, or A and C sites. For two monolayer of Co substrate, there is only hcp stacking possibility.

As shown in Table 4.1, for three monolayers of Co films with 12 Co atoms/cell, fcc structure is less stable compared to hcp one with energy higher about 0.087 eV/cell. We see clearly that the energy difference between fcc and hcp structures is so tiny, less than

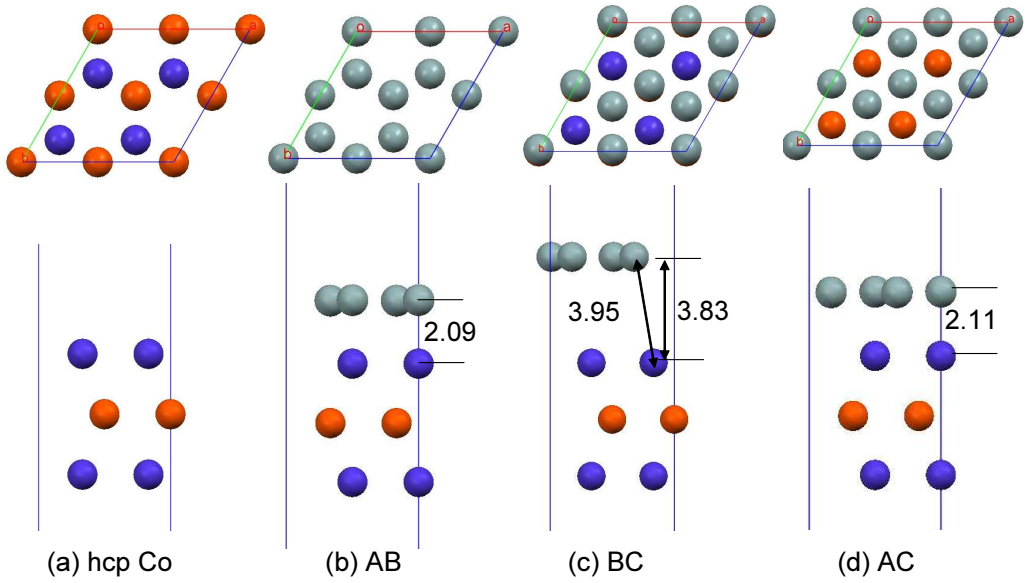

Fig. 4.2 : Top view (upper panels) and side view (lower panels) of calculated crystalline structures for (a) pure hcp Co film, (b) Graphene on top of *AB* sites, *AB*-Gr|Co(hcp), (c) Graphene on top of *BC* sites, *BC*-Gr|Co(hcp), and (d) Graphene on top of *AC* sites, *AC*-Gr|Co(hcp) structures. Co atoms in the 1st and 3rd (*A* site) are represented by blue balls, those in the 2nd(*B* site) layers are represented with red balls. Carbon atoms are indicated with gray balls. The distances between graphene and Co substrates are labeled.

8 meV/atom, which is negligible at room temperature (corresponding to 26 meV).

When Co substrates are covered with graphene, the most stable structure is *AC*-Gr|Co(hcp) as shown in Figure 4.2(d). But the energy difference between *AC*-Gr|Co(hcp) and *AB*-Gr|Co(hcp) is very tiny (0.01 eV/cell) for 12 cobalt and 8 carbon atoms per cell. For *AC*-Gr|Co(hcp) and *BC*-Gr|Co(hcp), the energy difference is a little bit large, 0.26 eV/cell. The stability can also be deducted from the distance between graphene and Co substrate shown in Figure 4.1 and Figure 4.2. For graphene on top of *BC* sites, the interaction is so weak between graphene and Co, and the distance is more or less around 4 Å. While for graphene on top of *AC* or *AB* sites, the distance is about 2.1 Å.

Overall, one can see that total energies of *AC* and *AB* structures for both hcp and fcc Co substrates are so close, and at room temperature, the difference can be neglected.

4.1.4 Magnetic Anisotropy of Graphene/Co

Now, let us discuss the magnetic anisotropy energy (MAE) of these films, which determines the easy axis of magnetization. The same as was discussed in Chapter 3, in a uniaxial system, the density of MAE can be described to first order as

$$E = Ksin^2\theta \tag{4.1}$$

with K in units of Jm^{-3}. Here θ is the direction of magnetization with respect to the normal to the layers. Positive values of K mean PMA, while negative values mean

Table 4.1: Thickness (momolayer) of Co, total energy $E_\perp$ ($E_\parallel$) of the system for magnetization orientation set to out-of-plane(in-plane), PMA value(mJ/m^2) and magnetic moment M(μ_B/cell) for different Gr|Co structures.

Structures	T_{Co} ML	$E_\perp$ eV	$E_\parallel$ eV	MAE mJ/m^2	M μ_B/cell
fcc Co	3	-79.455265	-79.454684	0.3703	20.765
AB-Gr|Co(fcc)	3	-153.18535	-153.18441	0.5991	19.3468
BC-Gr|Co(fcc)	3	-153.12020	-153.11962	0.3702	20.7495
AC-Gr|Co(fcc)	3	-153.22212	-153.22200	0.0765	19.4811
hcp Co	3	-79.542381	-79.540467	1.2274	19.799
AB-Gr|Co(hcp)	3	-153.41593	-153.41456	0.8731	18.985
BC-Gr|Co(hcp)	3	-153.16046	-153.15857	1.2045	19.783
AC-Gr|Co(hcp)	3	-153.42603	-153.42444	1.0133	18.656
Co	2	-51.343627	-51.342788	0.5347	13.6345
AB-Gr|Co	2	-125.11284	-125.11182	0.6501	12.7184
BC-Gr|Co	2	-124.97769	-124.97684	0.5417	13.6227
Co	1	-22.257611	-22.261216	-2.2975	7.6471
AB-Gr|Co	1	-95.770919	-95.768749	1.4020	6.2976
BC-Gr|Co	1	-95.937717	-95.941386	-2.3382	7.6160

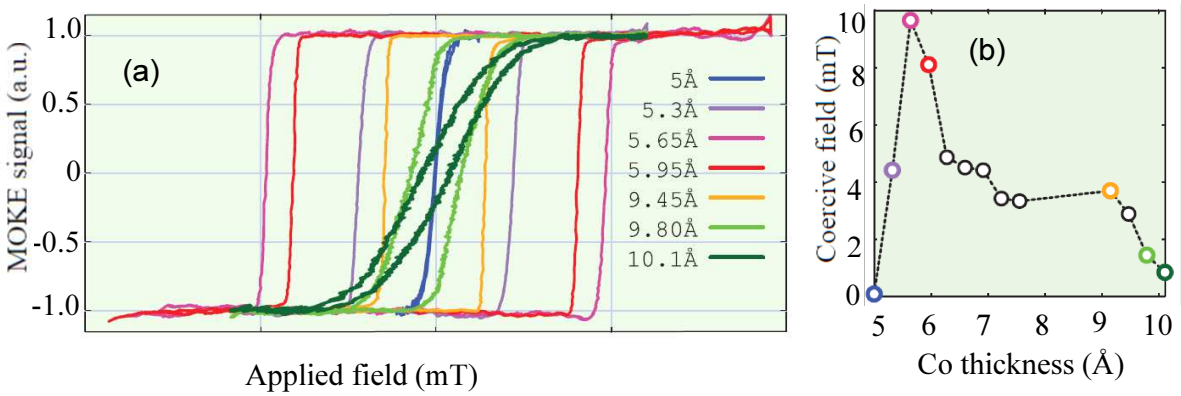

Fig. 4.3 : (a) Focused MOKE hysteresis loops of Co (capped with 3 nm Au, on graphene|Ir(111)) with various thicknesses in the range of PMA. The loops have been cycled and averaged at 11 Hz. (b) Coercive field (HC) as a function of the thickness of the Co layer, as derived from loops in (a) (and others which are not displayed for clarity in (a)). The peak of coercivity at low thickness may be related either to the expected variation of anisotropy, roughly inversely proportional to the thickness, or to the relative influence of thickness fluctuations. The figures are taken from reference [VVKBY$^+$10]

alignment of magnetization in the plane of the layers.

In experiments, hysteresis loops provide evidence for PMA in the range of thickness t∈ [0.5-1] nm (figure 4.3). In this range, the remanence is complete, i.e. the magnetization remains fully perpendicular to the film plane after the external field has been set back to zero. Let us recall that for most magnetic films the magnetization is strongly constrained to lie in-the-plane, due to the negative contribution to the MAE of the magnetostatic energy

$$E_{Shape} = -\mu M_s^2/2 \tag{4.2}$$

which would arise in the case of perpendicular magnetization. An effective PMA may be achieved only for selected cases where the magnetostatic energy is overcome by positive contributions to the MAE. Here we leave aside those cases where positive contributions arise from bulk magnetocrystalline anisotropy such as for intermetallics $4f - 3d$, FePt, CoPt, etc, because we focus on ultrathin films to highlight interfacial effects with graphene. In ultrathin films, positive contributions to the MAE may arise from interface and/or magneto-elastic effects. As both terms decay typically like 1/t, PMA is restricted to thicknesses typically below 1-3 nm. Known ultrathin stackings with PMA are either all metal based [JBdBdV96] or more recently metal oxide based [RMD$^+$09b, IMY$^+$10].

Combining with extraordinary Hall effect (EHE) measurements, the magnetic anisotropy is estimated around 0.185± 0.025 mJ/m^2 for the 0.7 nm thick Co layer. While recent experimental results show that PMA can be persisted with more than 50 monolayers of Co thickness [LHHW11].

In our calculations, we find that the anisotropy of Co films strongly depends on the crystal structure and the thickness of Co. As shown in Table 4.1, for three monolayers of Co, hcp structure gives more than 3 times larger PMA than that of fcc one. This is in a very well agreement with previous calculations for free standing Co films [DKS94b]. With the coverage of graphene, *AB*-Gr|Co(fcc) structure gives almost double the PMA of pure Co, but *AC*-Gr|Co(fcc) structure decreases the PMA almost to the in plane one. As for *BC*-Gr|Co(fcc) structure, the PMA is almost the same as that of pure fcc Co due to very weak interaction between graphene and Co, which can not create much impact on Co orbitals. For hcp structure, with 3 layers of Co film, graphene coverage does not improve the PMA of Co. But for two monolayers of Co, graphene does enhance the PMA from 0.53 mJ/m^2 of pure Co to 0.65 mJ/m^2 of *AB*-Gr|Co. More interestingly, anisotropy of single Co layer is known to be in plane [DKS94b]. In our calculation, the in-plane anisotropy of single layer of Co is about -2.3 mJ/m^2. According to reference [DKS94b], the in-plane anisotropy of one layer of Co is about -1.6 meV. If we assume the energy is per one Co atom, then the anisotropy is about -4.07 mJ/m^2, if we assumes -1.6 meV per 2 Co, (we assume 2 Co atoms because one hcp Co unit cell contains 2 atoms) then the anisotropy is about -2.04 mJ/m^2. In all cases, the order and the sign of anisotropy are in good agreement. Unlike graphene on thick Co films, with the coverage of graphene on one single Co layer, graphene has strong influence on anisotropy which even changes the sign from in-plane to out-of-plane. The value of PMA is also very large, 1.4 mJ/m^2, even larger than for pure 3 layers of hcp Co (1.2 mJ/m^2).

In addition to the effects on PMA, graphene also causes the reduction of magnetic moment of Co at the interface, as shown in [see Table 4.1]. With the presence of graphene, *AB*-Gr|Co and *AC*-Gr|Co structures, both fcc and hcp stacking, Co magnetic moments

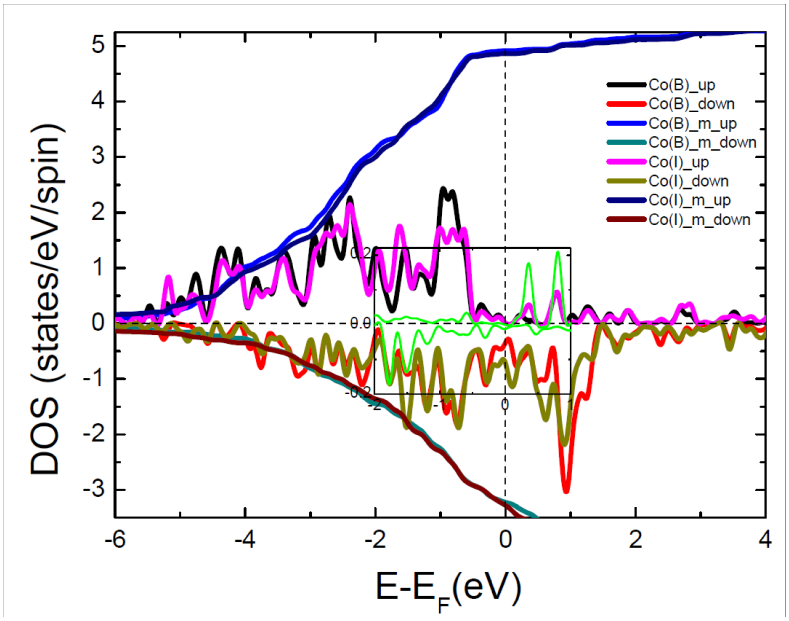

Fig. 4.4 : Spin-resolved density of states for bulk cobalt, Co(B), and interfacial cobalt, Co(I), are shown in graphene|Co systems. The integrated DOS are also shown correspondingly. Inset is the density of states for the carbon atom on top of Co.

decrease about 1 to 2 ν_B per cell. Whereas, due to the distance between graphene and Co surface is quite large in *BC*-Gr|Co structures, the total moments of *BC*-Gr|Co structures do not change much compared to no graphene covered Co films. Here, again from magnetic moments changes, we can also see the strength of interaction between graphene and Co substrates. Normally, when forming films or small clusters, Co magnetic moment will be enhanced. But here graphene reduces the magnetic moment of Co. In order to understand this unusual phenomenon, we did further calculations by using a five layers of hcp Co film with both sides of Co slab covered with graphene. Then we analyzed the density of states of Co atoms at interface [Co(I)] and in the middle layer [Co(B)], respectively, as shown in Figure 4.4. One sees that the occupation numbers (DOS integrated till Fermi level) of spin up states for bulk Co(B) at most of the energy range are higher than those of interface Co(I) (see the integration of bulk Co DOS: the blue line of Co(B)_m_up). For spin down states, however, absolute value of total Co(I), Co(I)_m_down, is larger than Co(B)_m_down at Fermi level. This is due to stronger hybridization between C-p_z and Co spin down states compared to that between C-p_z and Co spin up states, as shown by green curves with inset in Figure 4.4, which enhances the spin down occupation numbers. Thus, it becomes clear from equation (8.2) in Appendix to calculate total magnetic moments, bulk Co has larger magnetic moment than interfacial Co.

In conclusion, we demonstrated that graphene may have strong influence on the anisotropy of Co films, depending on the crystal structure and thickness of Co, as well as the epitaxial orientation. Here it is also worth to mention that with graphene coverage, the interfacial Co magnetic moment is reduced [see Table 4.1], which has been observed

in experiment [VVSC$^+$11].

4.2 Work Function of Graphene/Co

In solid-state physics, the work function is defined as the minimum energy needed to remove an electron from a solid to a point immediately outside the solid surface, namely the energy needed to move an electron from the Fermi level into vacuum. Here "immediately" means that the final electron position is far from the surface on the atomic scale but still close to the solid on the macroscopic scale.

The work function is important for design of the metal-semiconductor junction in Schottky diodes or vacuum tubes. Similarly, the work function is a very important parameter for the application of graphene. In this section, we investigate the impact of graphene on work function of Co films.

In the first section of this chapter, we have seen that interaction between graphene and hcp or fcc Co films strongly depends on the epitaxial orientation. But the crystal structures of fcc or hcp actually have no much difference. The energy difference is less than 0.2 eV for 12 Co and 8 carbon atoms per cell. Since the work function is of order of eV, here we consider the most stable case of hcp Co substrate.

As shown in Figure 4.5, we considered *AB*-Gr|Co(hcp), *BC*-Gr|Co(hcp) and *AC*-Gr|Co(hcp) structures, where Co films contain 5 layers for symmetric structures, while it contains 4 layers of Co for asymmetric case. The position of Co and graphene layers are represented with black and grey balls, respectively. Fermi level is normalized to zero eV. In symmetric structures [Figure 4.5(a),(b) and(c)], the solid black lines indicate the electrostatic potential of pure hcp Co films, and the dashed red lines represent the electrostatic potential of Gr|Co|Gr structure. In asymmetric case, left hand side is the vacuum/graphene/Co potential, and right hand side is the Co|Vacuum potential, respectively. For pure hcp Co films, the work function is about 4.9 eV, which is very close to experimental value of 5 eV. With asymmetric Gr|Co|Vacuum structure, the work function is a little bit smaller with value of 4.53 eV compared to that of the symmetric case.

When covered with graphene, the work function of Co is strongly reduced as shown in Figure 4.5. For *AB*-Gr|Co(hcp) and *AC*-Gr|Co(hcp) structures, the work functions decrease to 3.5 and 3.6 eV, respectively. For *BC*-Gr|Co(hcp) structure, as we have mentioned before, the interaction between graphene and substrate is very weak and the work function is not influenced much, giving 10 orders smaller than those of *AB*-Gr|Co(hcp) and *AC*-Gr|Co(hcp) structures. For the asymmetric structure, where we used only 4 monolayers of Co, the reduction of work function due to graphene coverage is estimated to be about 0.9 eV.

In experiments, using spin-polarized low-energy electron microscopy (SPLEEM), N. Rougemaille et al obsered that the work function is reduced about 0.83 eV due to the coverage of graphene [CNR$^+$]. This reduction is much larger compared with conventional metal or molecule contacts.

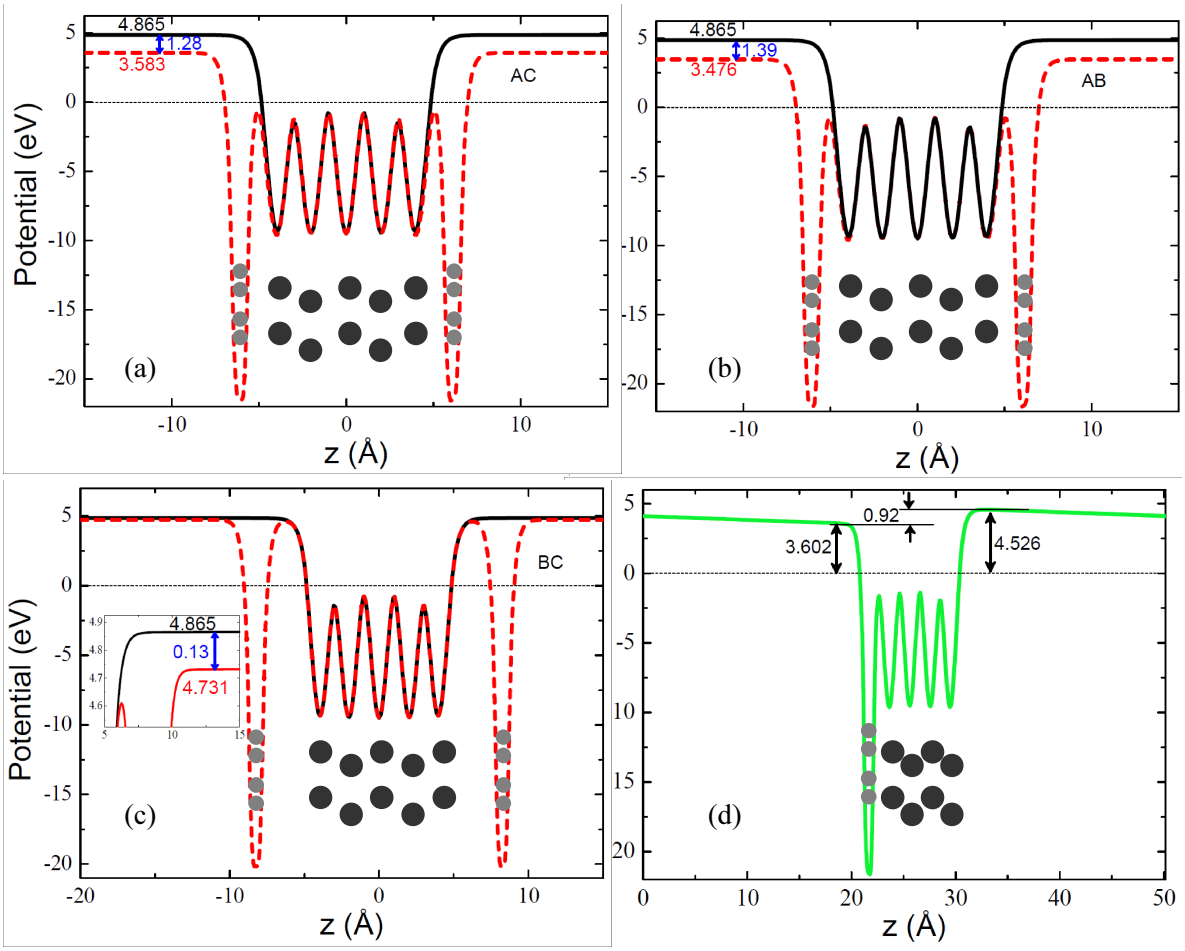

Fig. 4.5 : Electrostatic potential energy of graphene/Co slab relative to Fermi level. The position of the Co layers and of the graphene one used in the calculations are shown on a side view with gray balls. The work function are labeled and the reduction due to graphene is also indicated. For example, in Figure (d) the work function on graphene side is 3.60 eV, and it is 4.52 eV on the Co side. Thus, graphene decreases the work function by 0.92 eV.

4.3 Summary

In this Chapter, we have studied the impact of graphene on Co film properties. We showed that for thick Co films with graphene coverage the perpendicular magnetic anisotropy is preserved, which has been proved by experiments. Moreover, in case of a single layer of Co film, graphene coverage can switch the anisotropy from in-plane to out-of-plane with a large PMA value. Furthermore, we demonstrated that the graphene can strongly reduce the work function of Co surface which is also in a good agreement with experiments. Finally, the reduction of magnetic moment of interfacial Co is presented and explained, providing a good agreement with observations as well.

Chapter 5

Graphene on magnetic insulator

In this chapter, the spin-polarization of graphene on EuO substrate is investigated. We show that an average spin-polarization about 12 % could be obtained. Moreover, with a shifting of Fermi level, much larger spin-polarization of 100 % may be attained. It is also demonstrated that Dirac cone in graphene could be tuned by the substrate. Finally an unusual magnetic order is unveiled in graphene layer.

5.1 Interest of graphene on magnetic insulator

Semiconducting devices rely on the gap because it is the gap that allows a semiconductor to be switched from conducting to insulating. In principle, the larger the gap the better for application since it insures a large on/off ratio for switching devices. Therefore, for graphene-based electronic applications, we have to find ways to make graphene open a gap. One way to open a gap in graphene is using confined structures, e.g. graphene nanoribbon and graphene nonomesh [SCL06b, BZJ$^+$10]. Indeed, a graphene ribbon with a width of 1 nm has theoretically a band gap of nearly 1 eV. An energy gap of this magnitude is good enough for electronic applications, but the size scale of 1 nm is in the range of fabrication limit. In the sense of size scale, graphene nanomeshes may help to solve the problem [BZJ$^+$10]. Another solution to obtain large scale opened-gap graphene is using insulating substrate, the very famous one is using 4H- or 6H-SiC substrate. But other insulating substrates are also intensively investigated, for example, Al_2O_3, MgO, SiO_2, BN and GaAs.

In parallel to semiconductor applications, graphene is also believed to have intensive potential applications for spintronics. For graphene-based spintronics, one may say to induce magnetism is as important as to open a band gap in graphene-based electronics. Just like in semicondutor applications, the approaches to open a gap in graphene are also used to induce magnetism, e.g. half-metallic zigzag graphene nanoribbon and graphene nanomeshes, as well as using a substrate. However, the substrates used to induce magnetism are mainly metals, like Co and Ni [VSBS$^+$08, WRH$^+$10, RVSB$^+$09, GKB$^+$08]. The properties of these epitaxial films have been extensively studied, however since these film are grown on conducting substrates, they have little electronic applications potential which requires insulating substrates. Thus, to epitaxially grow graphene on insulating magnetic substrates becomes critical for spintronic applications.

As for magnetic insulating materials there are NiO, EuO, EuS, and Fe_3O_4 etc.

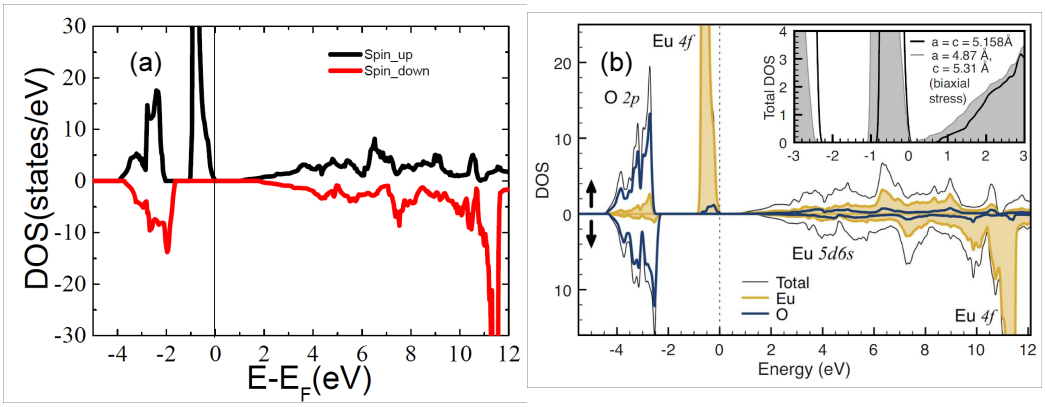

Fig. 5.1 : GGA+U calculated total density of states for bulk EuO, panel(a) is our calculation with PBE potential and (b) is taken from reference PRB 77, 121202(R) 2008 with LDA+U. Both approaches give magnetic insulating ground state.

Considering the lattice mismatch, in this chapter, we choose EuO for substrate to investigate graphene on insulating magnet.

5.2 Calculation details and structures

The Vienna *ab initio* simulation package (VASP) [KH93, KF96b, KF96a] was used again in our calculations, where the electron-core interactions were described by the projector augmented wave method for the pseudopotentials [Blo94], and the exchange correlation energy was obtained within the generalized gradient approximation of the Perdew-Burke-Ernzerhof (PBE) form [WP91, KJ99]. The cutoff energies for the plane wave basis set used to expand the Kohn-Sham orbitals were 520 eV for all the calculations. A $4 \times 4 \times 1$ k-point mesh within Monkhorst-Pack scheme was used for the Brillouin zone integration. Structural relaxations and total energy calculations were performed ensuring that the Hellmann-Feynman forces acting on ions were less than 10^{-3} eV/Å. Since Eu is a heavy element with atomic number of 63, and its outer shell ($4f^7 6s^2$) contains f electrons, GGA approach fails to describe the strongly correlated localized $4f$ electrons of EuO giving the metallic ground state of EuO, whereas a clear band gap is observed in experiment [IE08, MG86]. Thus, here we introduce Hubbard-U parameter to describe the strong intra-atomic interaction in a screened Hartree-Fock like manner. For the parameter choice, we take the on-site Coulomb repulsion and exchange interaction on Eu $4f$ orbital of 8.3 eV and 0.77 eV, respectively. For oxygen p orbitals, the on-site Coulomb and exchange parameters are 4.6 eV and 1.2 eV, respectively [IE08].

Using GGA+U method, we first optimized the lattice of EuO and found the lowest energy is reached when lattice equals to 5.188 Å. This value is very close to the LDA+U result, 5.158 Å, and experimental one, 5.141 Å(the error is about 0.9 %). With the

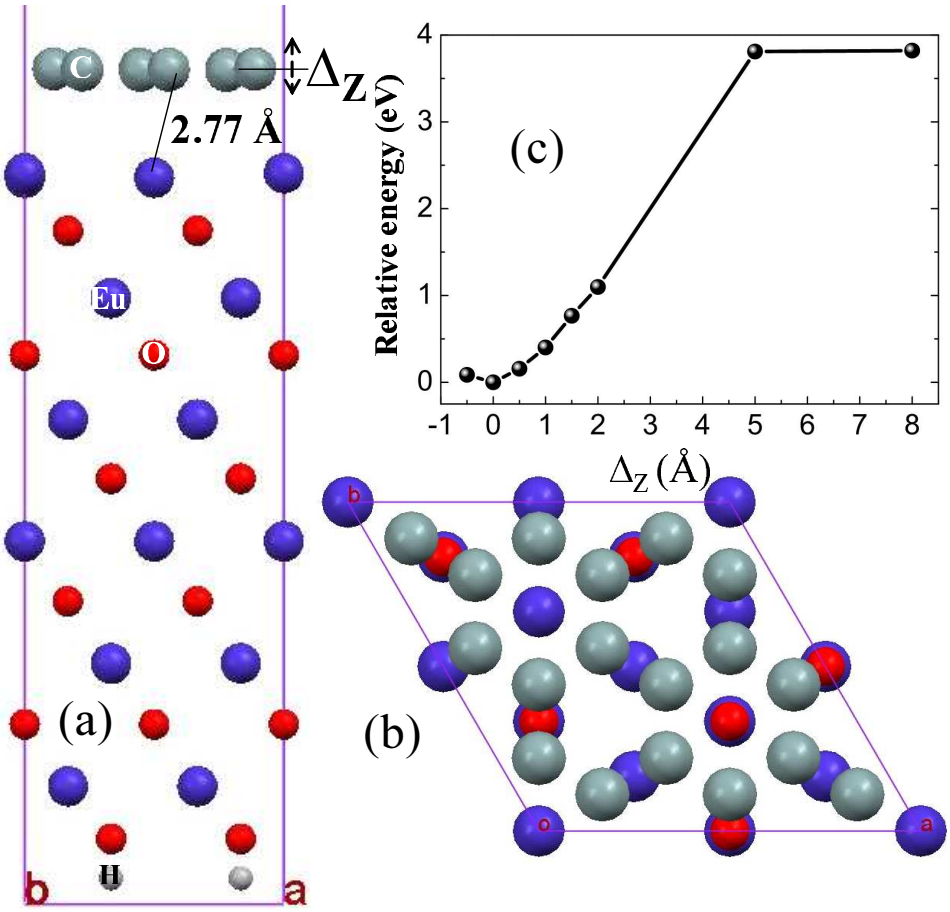

Fig. 5.2 : (a) side view and (b) top view of the calculated crystalline structures for graphene on top of a six bi-layer EuO film, the bottom of EuO is terminated with hydrogen atoms. (c) relative energy (to the optimized structure) of Graphene/EuO as a function of shifting distance (Δ_Z) between graphene and substrate.

optimized lattice, we then calculated the density of states for EuO with ferromagnetic state as shown in Figure 5.1, where a band gap is observed with value about 1.0 eV. This is consistent with the experimental optical absorption gaps of 0.9 and 1.2 eV observed below and above the magnetic transition temperature [SW74]. Here GGA+U method gives better results compared to LDA+U. LDA+U method gives 0.7 eV band gap with ferromagnetic spin arrangement, and 1.2 or 1.3 eV for 111 antiferromangetic spin configuration (AFMI) or the NiO-type antiferromangetic spin configuration (AFMII), respectively.

Let us now consider the lattice mismatch between graphene and EuO. If we use experimental values, graphene lattice constant is 2.46 Å, and EuO one is 5.141 Å. Along (111) surface of EuO, a 2 × 2 surface unit cell is about 7.2704 Å, which can fit with a 3 × 3 unit cell of graphene with lattice mismatch about 1.46%. If the GGA+U optimized lattice constant is used, 5.188 Å, the mismatch is much smaller (less than 1%).

With such a reasonable lattice matching, we first studied the stability of graphene on EuO surface prior studying spintronic properties. Two structures with graphene on oxygen terminated surface and Eu terminated surfaces are considered. In this two configurations, we have the same amount of atoms, 18 carbon atoms, 24 oxygen and 24 Eu atoms. The calculated total energies are found to be -544.50389 eV and -545.16824 for Gr@EuO(O-terminated) and Gr@EuO(Eu-terminated), respectively. One can see that with Eu-terminated surface, the system is more stable with gaining energy about 0.67 eV. Thus, we use the lowest energy configuration of 12 layers of EuO as a substrate and the bottom oxygen terminated by hydrogen to simulate graphene on a semi-infinite EuO surface. For all calculations, the vacuum length is chosen larger than 20 Å. The interaction between EuO substrate and graphene are quite strong, with the vertical distance about 2.57 Å as shown in Figure 5.2.

5.3 Spin polarization of graphene on EuO

In this thesis, spin polarization is defined as the ratio between occupied spin up and spin down at Fermi level. One can calculate this directly from spin-resolved density of states.

Using the optimized structure of graphene on EuO shown in Figure 5.2, we calculated the local density of states for this system [Figure 5.3]. Due to the existence of EuO substrate, symmetry of carbon atoms in graphene lattices are broken into six folders as shown in Figure 5.3(a) with different colors. For clarity, atoms in EuO substrate are shown with crosses. In this structure, the calculated magnetic moment of Eu on surface are found a little bit enhanced about 7.0 μ_B compared to the bulk ones of 6.9 μ_B. And the sublayer oxygen atoms are found to be spin polarized too, with magnetic moment of about -0.11 μ_B.

Due to very strong spin polarization of EuO substrate, magnetic properties of graphene are strongly affected. As shown in Figure 5.3, the average spin polarization in graphene layer is found to be about 12%. This value is not large, but if we can shift a little bit Fermi level, the spin polarization can be strongly enhanced even up to 100%. Interestingly, around -1 eV, the spin up and spin down densities are zero, but the energy ranges are different, which actually related to the breaking of Dirac point. We will discuss this in more details in the next section. Since these 18 carbon atoms are broken into 6

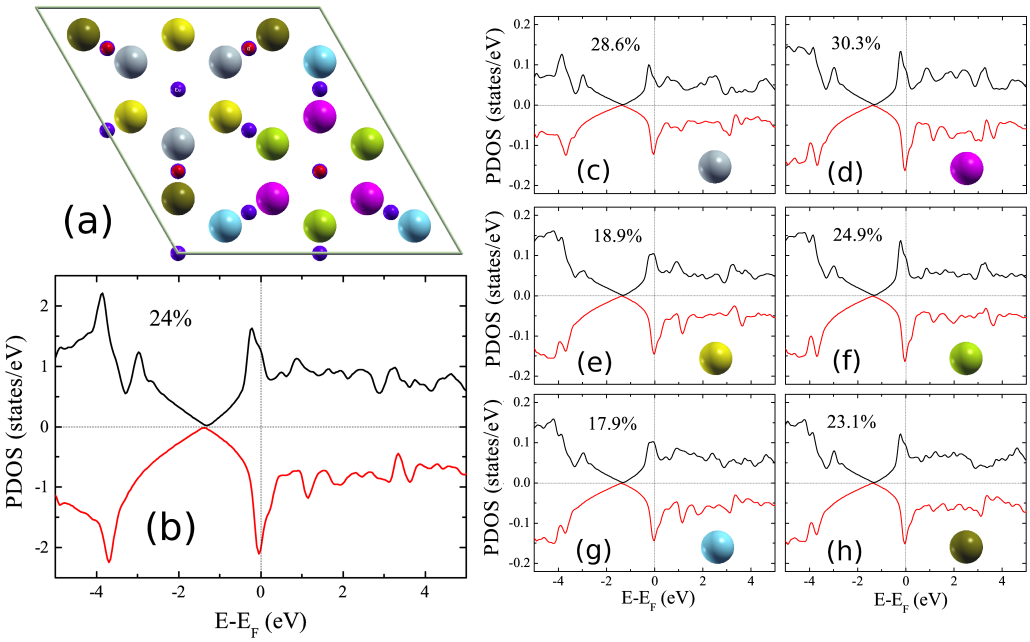

Fig. 5.3 : (a) The six lattices of graphene on EuO represented with different colors, (b) total density of states of p_z orbital of graphene, (c)-(h) local density of states on each inequivalent atom of the supercell (a). The spin polarizations in (b)-(h) are calculated by comparing the density of states between minority and majority states normalized by the total density of states at Fermi level, i.e. $p = \frac{n^{\downarrow} - n^{\uparrow}}{n^{\downarrow} + n^{\uparrow}}$.

symmetry groups, their contribution to the total spin polarization are also different. For the purple one having largest magnetic moment in graphene, its spin polarization can reach up to 72%, while for the yellow one with smallest magnetic moment, its spin polarization is just 9.6%. Also because the direct interaction between two lattices of intrinsic graphene and the interaction between graphene and EuO substrate, the spin polarization of some of carbon atoms is negative.

The origin of the spin polarized electrons are due to p_z orbital, namely the π bond as shown in Figure 5.3(c).

5.4 Tuning of Dirac Cone

The honeycomb structure can be thought of as a triangular lattice with a basis of two atoms per unit cell, with 2D lattice vectors $\mathbf{A_0} = \frac{a_0}{2}(\sqrt{3}, 1)$ and $\mathbf{B_0} = \frac{a_0}{2}(\sqrt{3}, -1)$, where a_0 is the graphene lattice 2.46 Å. Of particular importance for the physics of graphene are the two points $\mathbf{K}$ and $\mathbf{K'}$ at the inequivalent corners of the graphene Brillouin zone $\mathbf{K} = \frac{2\pi}{a_0}(\frac{1}{\sqrt{3}}, \frac{1}{3})$ and $\mathbf{K'} = \frac{2\pi}{a_0}(\frac{1}{\sqrt{3}}, -\frac{1}{3})$ Which are called Dirac points, they play a role similar to the role of $\mathbf{\Gamma}$ points in direct band-gap semiconductors such as GaAs. The reason why these points are called Dirac points are due to the band dispersion close to the $\mathbf{K}$ (or $\mathbf{K'}$) vector, as $\mathbf{k} = \mathbf{K} + \mathbf{q}$, with $|\mathbf{q}| \ll |\mathbf{K}|$, has the form [Wal47],

$$E_{\pm}(\mathbf{q}) \approx \pm v_F |\mathbf{q}| + O[(q/K)^2] \tag{5.1}$$

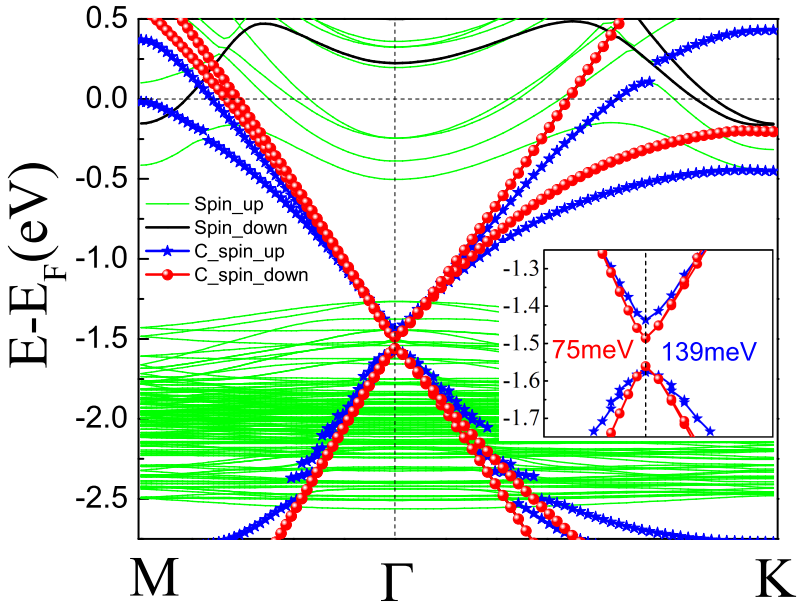

Fig. 5.4 : Band structure of graphene on EuO. Black and red lines represent spin up and spin down bands, respectively. Inset is the zoom in of graphene band at Dirac cone.

where $\mathbf{q}$ is the momentum measured relatively to the Dirac points and v_F is the Fermi velocity, given by $v_F = \sqrt{3}ta_0/2$, with a value $v_F \simeq 1 \times 10^6 m/s$, and t is the nearest-neighbor hopping energy of 2.8 eV.

In the usual case with $\epsilon(\mathbf{q}) = q^2/(2m)$, where m is the electron mass, the velocity, $v = k/m = \sqrt{2E/m}$, changes with energy. In Equation 5.1, the Fermi velocity does not depend on the energy or momentum. For more details of discussion, please see review by Castro Neto et al. [CNGP+09]. In this chapter, we use substrate effects to tune the dispersion at Dirac point.

As one can see from Figure 5.4, at K point, the linear dispersion of graphene band structure is preserved on EuO substrate even though there is a band gap opening. More interestingly, the breaking of Dirac point is spin dependent. Two of the spin branches give the gap opening in graphene with values of 75 meV and 139 meV, respectively [see the inset in Figure 5.4]. This spin splitting is due to the interaction of C-p_z and Eu-4f orbitals, and as we know that the orbital of Eu-4f right below Fermi level is pure spin up states [as shown in Figure 5.1]. Thus, when interacting with graphene, the substrate behaves like a spin injector from Eu-4f state. This can be seen from the band structure, where the graphene bands are involved with the spin up Eu-4f bands.

Considering that graphene is very flexible, and the interaction between graphene and substrate is much weaker than that of intra C-C interaction. This interaction is easily affected by the environment. We calculated the configurations with different distance between graphene and substrate [Figure 5.2]. One can see from Figure 5.2(c) that with shifting of graphene less than 1 Å, the energy does not change much, 0.085 and 0.156 eV/cell for shifting in- and out-ward 0.5 Å, respectively. Here we say the energy does not change much, because one supercell contains 18 carbon atoms, in average, the energy

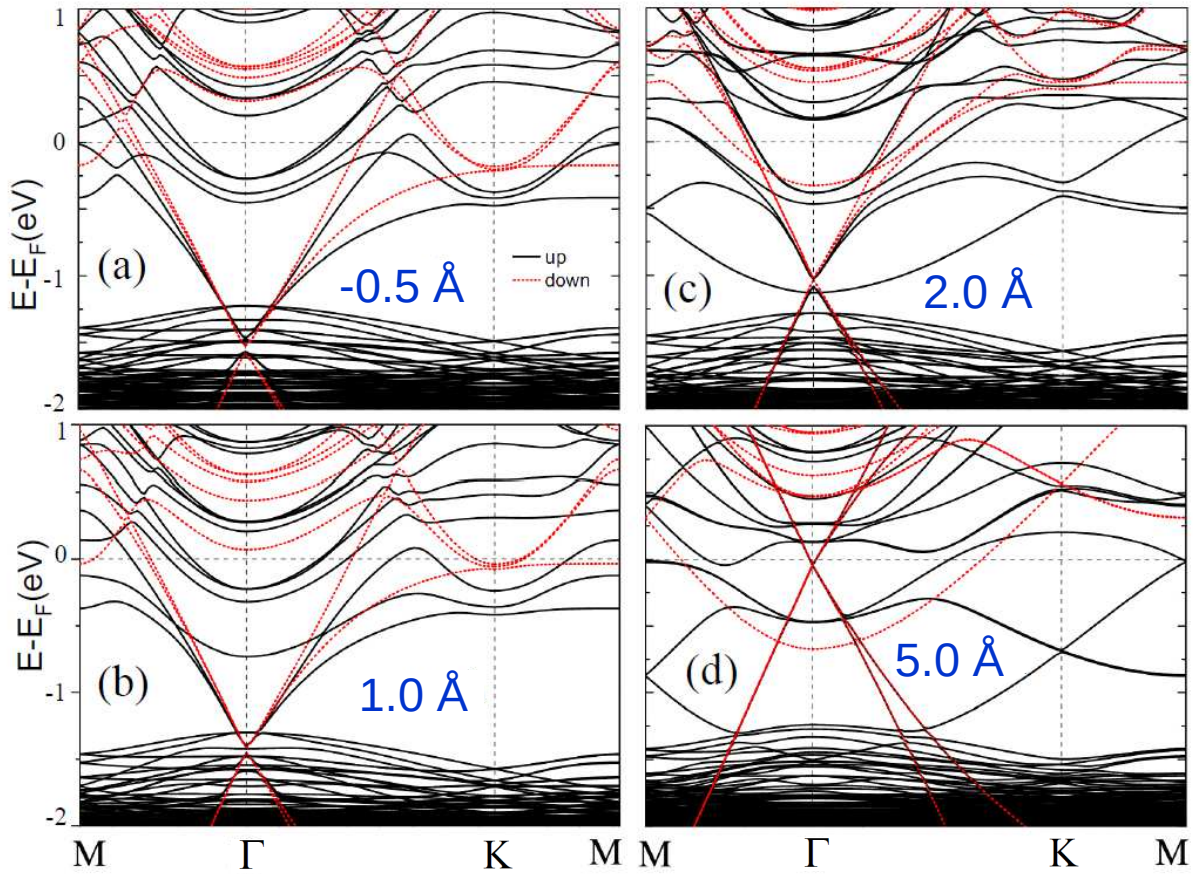

Fig. 5.5 : Band structures for graphene on EuO with graphene shifted inward (compared to optimized structure) 0.5 Å (a), with graphene shifted outward 1.0 Å (b), with graphene shifted outward 2.0 Å (c) and shifted outward 5.0 Å (d).

changes per carbon atom is in meV order.

Even though the stability with small distance shifting is not strongly affected, the band dispersion of graphene, actually, is strongly tuned as shown in Figure 5.5. For the inward shifting of graphene with 0.5 Å, there are more charge/electrons (spins) transfered to graphene layer due to enhanced overlap between C p_z and Eu $4f$ orbitals. Therefore, one can see that the Dirac point is a bit deeper inside of valence band compared to the optimized case. Whereas, with outward shifting of graphene, a clear trend of Dirac point is shifting out from the valence band of EuO and approaching closer to the Fermi level. In case of very large shifting with 5 Å [Figure 5.5(d)], one can see that the Dirac point almost cross the Fermi level. At the same time, with the shifting of the Dirac point out of EuO valance band, the degeneracy of spin up and spin down bands are becoming closer and closer. In case of the 5 Å shifting, the spin up and spin down branches become degenerated again.

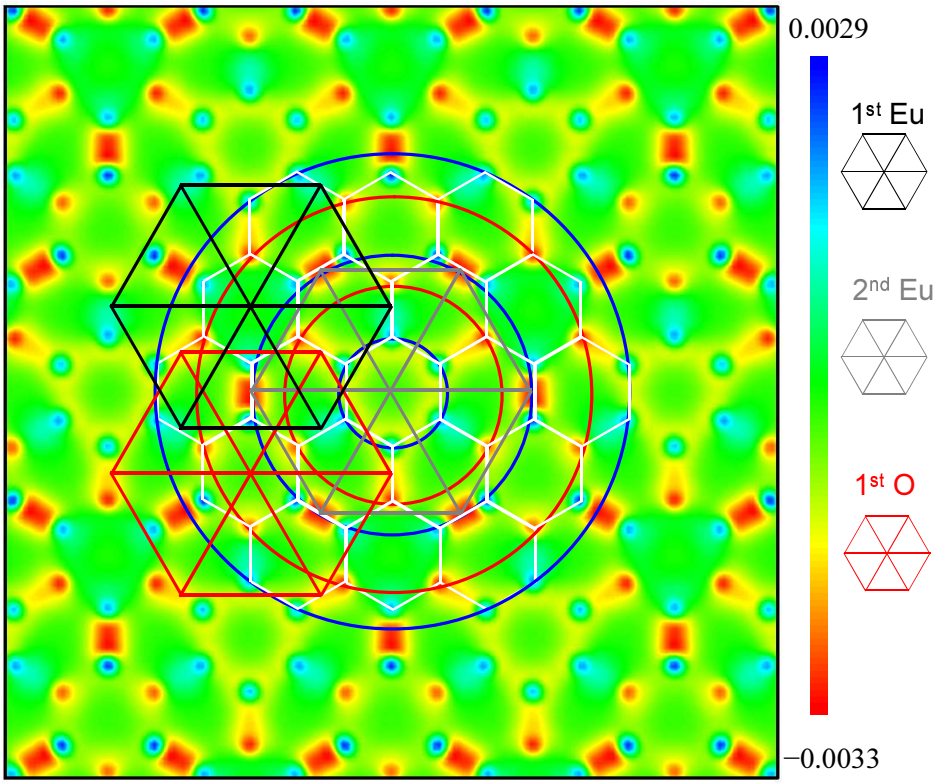

Fig. 5.6 : Spin density ($\mu_B/\text{Å}^2$) for graphene on EuO across the graphene layer. The structure of graphene is partially indicated with white lines. The 1st and 2nd layer of Eu and 1st oxygen in substrate are also indicated. Red and blue circles represent the spin up and spin down atoms in graphene layer.

5.5 Magnetic order in graphene on EuO

The interaction between graphene and EuO substrate causes the symmetry breaking of graphene lattices. In one unit cell, we have six lattices as shown with different colors in Figure 5.3(a). As we have seen in the previous section, the spin polarization and magnetic moment strongly depend on lattice position, namely its neighboring atoms. We also investigated the magnetic moment and spin polarization for each lattice. The magnetic order, long range and short range, is indeed a very important information for both fundamental research and applications. Therefore, in this section, we continue investigating the magnetic ordering in spin polarized graphene caused by EuO substrate.

In order to visualize the magnetic order, a straightforward way is to plot the spin distribution of the system. Since graphene is a 2-D material, a spin density across graphene layer is enough to see the magnetic order. In Figure 5.6, we plot the spin density for optimized graphene on EuO substrate (in unit of $\mu_B/\text{Å}^2$). For clarity, the structure of graphene is partially indicated by white honeycomb configuration. Since the substrate effect is important, we also show the structure of substrate for the first and second layer of Eu, as well as first layer of oxygen [see the caption in Figure 5.6]. One can

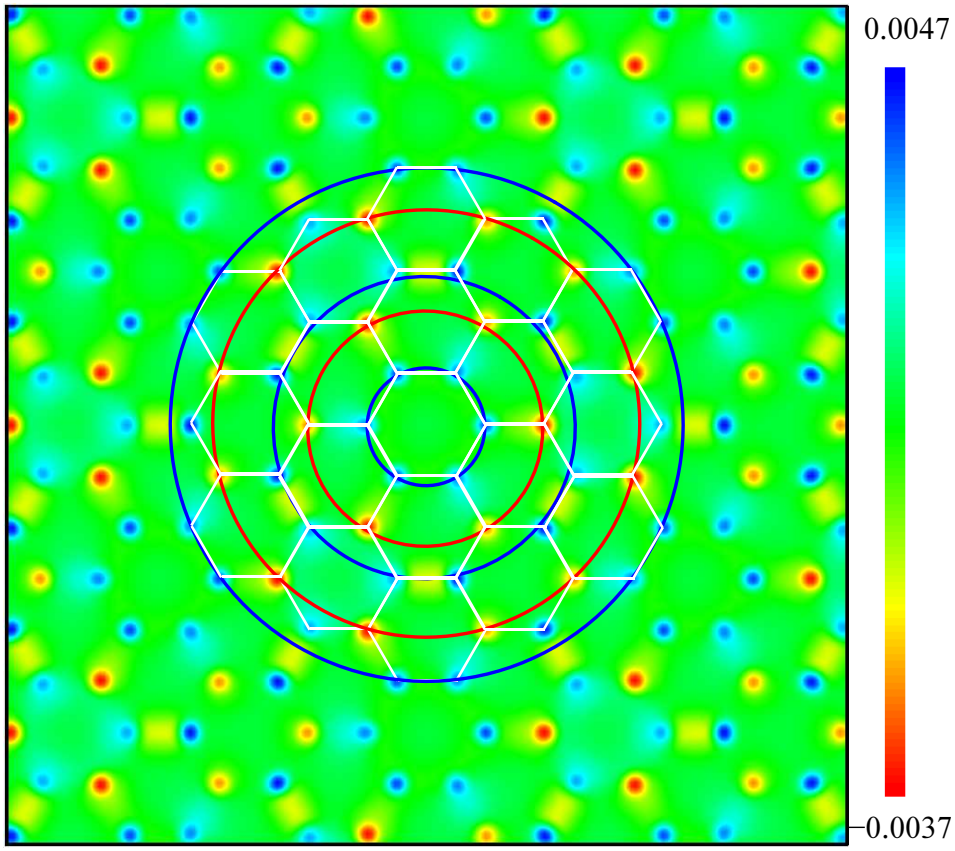

Fig. 5.7 : Spin density ($\mu_B/\text{Å}^2$) for graphene on EuO across the graphene layer when graphene is shifted outward 0.5 Å compared to the optimized structure.

clearly see that starting from a local ferromagnetic centered hexagonal structure [shown by the smallest blue circle in Figure 5.6], at least five opposite spin circles are formed. It is necessary to note that large squared red spots are caused by the substrate oxygen p_z orbital which should be ignored when we consider the magnetic order in graphene layer. Their role will become clear later when we show the shifted graphene on EuO. The hexagonal structure on top of the first layer of oxygen forms a localized ferromagnetic structure, which is opposite to the normal picture of spin distribution in graphene. Because in a hexagonal structure, three atoms belong to A lattice and another three belongs to B lattice, according to Lieb's theorem which is calculated by a Hubbard model, A and B sites should have opposite spin orientation if there is spin caused by defects. [Lie89, YCB+11]. Next, two carbon atoms across an oxygen atom will form ferromagnetic coupling, a kind of super-exchange, but the angle for C-O-C being 20.28°. At the same time, two carbon atoms across an Eu atom will form antiferromagnetic coupling, the angles for C-Eu(1^{st} layer)-C and C-Eu(2^{nd} layer)-C are 29.48° 14.38°, respectively.

As we have mentioned above, shifting of graphene within 1 Å will not affect much of the total energy, which means at room temperature those structures are also possible to realize. We investigated thus the magnetic ordering of shifted graphene on EuO compared to optimized case. Indeed, these shifted structures give clear evolution pictures. As shown

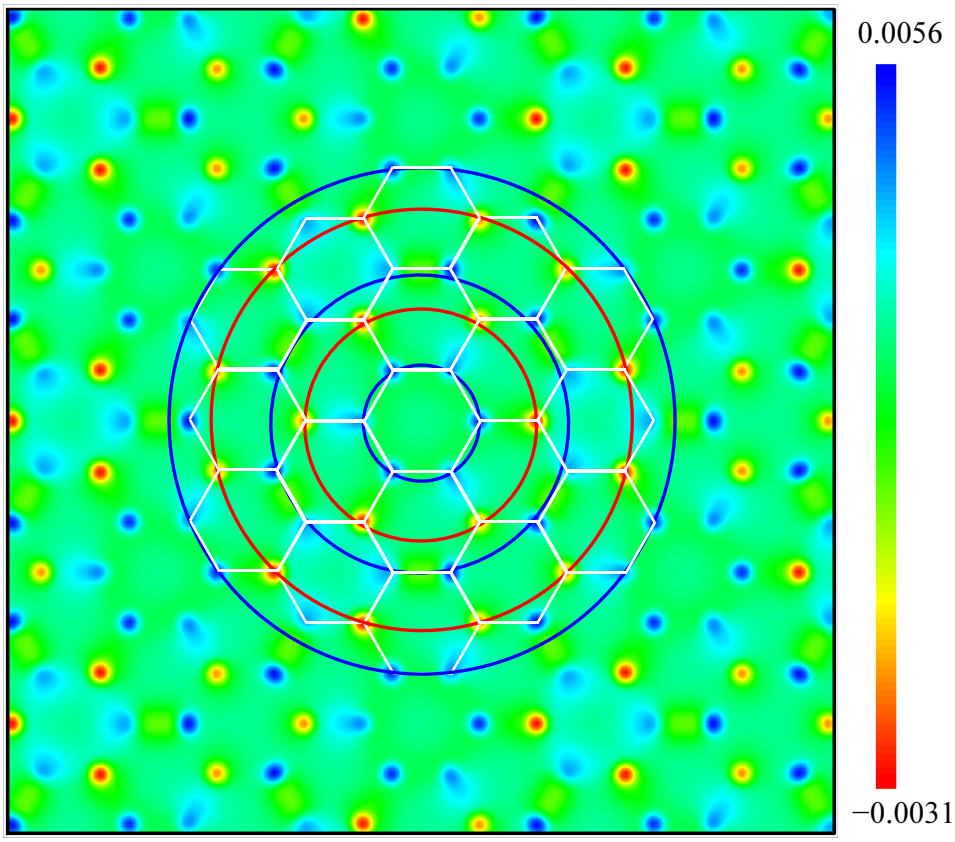

Fig. 5.8 : Spin density ($\mu_B/\text{Å}^2$) for graphene on EuO across the graphene layer when graphene is shifted outward 1.0 Å compared to the optimized structure.

in Figure 5.7, the spin distribution for graphene shifted outward with 0.5 Å compared to that of the optimized case. Similar to the tuning of Dirac cone, where with the outward shifting of graphene, the interaction between graphene and EuO becomes weaker and the degeneracy splitting between spin up and spin down bands becomes smaller, as well as the Dirac cone moves out of EuO valance band to Fermi level. For the spin distribution, we see that even with very small shifting of graphene, 0.5 Å, it is clear that the red square spots become weaker compared to small yellow square ones. It actually also reflects that the overlap between graphene and EuO orbtials is becoming weaker. More clearly, for the case with graphene shifted outward by 1.0 Å [Figure 5.8], the large square red spots in optimized case or the yellow square spots in Figure 5.7 are almost invisible. However, in both of the 0.5 Å and 1.0 Å shifting cases, the magnetic order does not change and the pattern is still preserved as in optimized case.

5.6 Summary and Perspective

With a very good lattice matching between graphene and rock salt EuO (111) surface, we investigated the spin polarization of graphene and its magnetic order induced by EuO proximity. EuO substrate breaks a bipartite lattice of graphene into six ones. At the same time, graphene becomes magnetic due to strong magnetization of EuO which behaves like a spin injector. Therefore, it is straightforward that the magnetization of carbon atoms of graphene should depend on their positions on EuO, which leads to an unusual magnetic order in graphene. This magnetic order is still unclear. Nevertheless, both spin polarization and magnetic order reported should lead to many interesting phenomena. For instance, the substrate induced magnetic moment in graphene may lead to stronger anomalous Hall effect, the gap opening in graphene may provide a root to semiconducting applications. And the difference gap opened at Dirac point for spin up and spin down is also very exciting for spintronics. Furthermore, the unusual magnetic order may serve for realizing spin frustration structures or even spin density wave investigations.

Chapter 6

Electronic and magnetic properties of graphene nanomeshes

In this Chapter, we explore the electronic and magnetic properties of graphene nanomeshes (GNM), a regular network of large vacancies, produced either by lithography or nanoimprint. When removing an equal number of A and B sites of the graphene bipartite lattice, the nanomesh made mostly of zigzag (armchair) -type edges exhibit antiferromagnetic (spin unpolarized) states. In contrast, in situations of sublattice symmetry breaking, stable ferri(o)magnetic states are obtained. For hydrogen-passivated nanomesh, the formation energy is dramatically decreased, and ground state is found to strongly depend on the vacancies shape and size. For triangular-shaped holes, the obtained net magnetic moments increase with the number difference of removed A and B sites in agreement with Lieb's theorem for even A + B. For odd A + B triangular meshes and all cases of nontriangular nanomeshes, including the one with even A + B, Lieb's theorem does not hold anymore, which can be partially attributed to the introduction of armchair edges. In addition, large triangular-shaped GNMs could be as robust as nontriangular GNMs, providing a possible solution to overcome one of the crucial challenges for the sp magnetism. Finally, significant exchange-splitting values as large as 0.5 eV can be obtained for highly asymmetric structures evidencing the potential of GNM for room-temperature carbon-based spintronics. These results demonstrate that a turn from zero-dimensional graphene nanoflakes throughout one-dimensional graphene nanoribbons with zigzag edges to GNM breaks localization of unpaired electrons and provides deviation from the rules based on Lieb's theorem. Such delocalization of the electrons leads the switch of the ground state of a system from an antiferromagnetic narrow gap insulator discussed for graphene nanoribons to a ferromagnetic or nonmagnetic metal.

6.1 Introduction

Two-dimensional graphene has emerged as a natural candidate for developing "beyond CMOS" nanoelectronics [NGM+04, NGM+05, ZTSK05, BSL+06, GN07, IK07]. In addition to the reported huge charge mobilities, the weak intrinsic spin-orbit coupling in carbon-based sp^2 structures [HGB06, YYQ+07] could potentially allow for very large (micron long) spin diffusion lengths. These features, together with the other

"semi-conductor like" properties of graphene, make graphene-based spintronic devices highly promising [FBY+01b, WAB+01] and have triggered a quest for controlling spin injection in graphene [TJP+07b, HWP+09, HPM+10, YBV+11]. Many routes have been attempted to induce magnetism by proximity effect or inject spins from magnetic electrodes [DSA+10]. Another, more intrinsic, possibility is shaping the geometry of graphene by designing graphene nanoribbons with zigzag edges [SCL06a, YPS+07]. This has been found to induce localized edge magnetic states which can serve as a conceptually new building block for spintronics [SCL06b, BFD07, WAB+08, MFP09, YH07, Yaz08, Yaz10, FP07, PFB08, SNT+12].

The existence of intrinsic magnetism driven by atomic-scale defects (such as vacancies, chemisorbed species, grain boundaries,etc.) has also been suggested theoretically [YH07, Yaz08, Yaz10, PFP+08, FPBJ09, ZZZ+09, LFM+04, HZP10, CYL08, SNT+12]. However, as we have mentioned in the general introduction, the magnetism in graphene remains fiercely debated on the experimental side [ESH+03, ČKF09b, MMJP+10, UBGG10, OEA+10, SNR+10]. The reason may be due to that it is very difficult to obtain a precise experimental characterization of those defects. Additionally, the absence of a true energy gap in two-dimensional graphene limits the elaboration of active graphene-based devices and circuits with standard semiconductor technologies.

Another route to make graphene magnetic is either chemisorption of odd number of adatoms or functional groups [YH07, Yaz08, Yaz10, Bou10, BK11], or using magnetism on zigzag edges [SCL06b, YK08, CKF09a, ET09]. In the first case the stability of magnetic configurations at room temperature can be easily destroyed by the migration of adatoms with turning the system into nonmagnetic configuration [Bou10, BK11]. In contrast to the adatom based magnetism edge [CKF09a, ET09] and vacancy [BKK11] magnetism in graphite is stable at room temperature. But herewith localization of the magnetic moments on the edges provides formation of the antiferromagnetic (AFM) exchange interactions between two edges [SCL06b].

The case of graphene nanoribbons obey Lieb's theorem because the localized electrons on one edge belong to sublattice A and localized electrons from other edge to sublattice B. Magnetism on the edges of graphene nanoflakes is also described by this theorem [YWMK08, WYMK09]. Electron localization plays an important role in the different many-body effects on graphene edges [CR09, Fer07] and bulk graphene [WG05, HHDS07]. Understanding the nature of the electron localization and delocalization in graphene and related systems is necessary not only for control and manipulation of magnetism in studied compounds but also for the development of knowledge about systems with strongly correlated electrons.

Graphene nanomesh (further GNM) is the intermediate compound between graphene nanoribbons with localized electrons on zigzag edges and perfect bulk graphene with delocalized electrons. The fabrication of GNM, using block copolymer lithography and offering versatility in varying periodicities and neck widths down to 5 nm [BZJ+10], could circumvent the hurdles. Indeed, such technique allows a scalable engineering of superlattices of large graphene vacancies whose density, shape and distribution can be controlled down to the nanoscale. Additionally, GNM-based field-effect transistors were shown to withstand current densities two orders of magnitudes larger than individual graphene nanoribbon devices, with comparable on/off ratio and easily tunable by varying the neck width. Moreover, in accordance to the well-established Lieb's theorem [Lie89],

the possibility to control inner edge structures [SYZ+11] of nanomesh vacancies could enable a true control of intrinsic magnetic properties.

In this chapter, we present first-principles calculations of electronic and magnetic properties of graphene nanomeshes, and found that by varying the shape, different types of intrinsic ferrimagnetic comment states can be obtained with clear identification of optimal conditions.

6.2 Methods

First-principles calculations were performed again using Vienna *ab initio* simulation package (VASP) [KH93, KF96a, KF96b] based on density functional theory (DFT) with generalized gradient approximation (GGA) for exchange correlation potential. We have used projected augmented wave method (PAW) [Blo94] with the Perdew-Becke-Erzenhof (PBE) parametrization [PBE96] potentials to describe the core electrons of carbon. Periodic 6 by 6 unit cells were used to simulate non-passivated GNM structures as shown in Figure 6.1, whereas periodic 8 by 8 unit cells were used to simulate H-passivated GNM structures. The kinetic cutoff energies for the plane wave basis set used to expand the Kohn-Sham orbitals were 520 eV for the self-consistent energy calculations. Methfessel-Paxton method [MP89] is used with a broading width of 0.2 eV for the partial occupancy smearing calculations. A $9 \times 9 \times 1$ k-point mesh was sufficient to ensure good convergence in the total energy differences. The structural relaxations were performed ensuring that the Hellmann-Feynman forces acting on ions were less than 10^{-3} eV/Å.

6.3 Model of graphene nanomeshes

A GNM can be formed by either removing atoms centered of a six ring structure [Figure 6.1(a,b,c)] or centered of one carbon atom [Figure 6.1(d)], which either lead to form GNM with balanced or unbalanced number of removed A and B sites. For the sake of clarity, we label those structures according to their shapes and put the number of removed A and B site atoms as a subscript. For instance, the structure of Figure 6.1(a) named $C_{3:3}$, corresponds to a Circle hole shape GNM with 3:3 denoting 3 A and 3 B atoms removed from perfect graphene. The superscript H is used for hydrogen-passivated GNM.

6.4 Results and discussions

For $C_{3:3}$ structure [Figure 6.1(a)], we find that the configuration with opposite spin orientation [Figure 6.3] between adjacent edge C atoms is energetically favored in comparison with the configuration with parallel spins between edge atoms of two sublattices represented by the blue and red color in Figure 6.1. The total energy calculations reveal quite large magnetic interaction energies. For instance, the energy difference between ferromagnetic (FM) spin-polarized and paramagnetic (PM) state is found to be 0.129 eV per edge atom. The spin configuration is further stabilized by 0.093 eV per edge atom as a result of the antiferromagnetic (AF) coupling between neighboring atoms with magnetic moment of 0.48 μ_B per edge atom for each spin on each sublattice

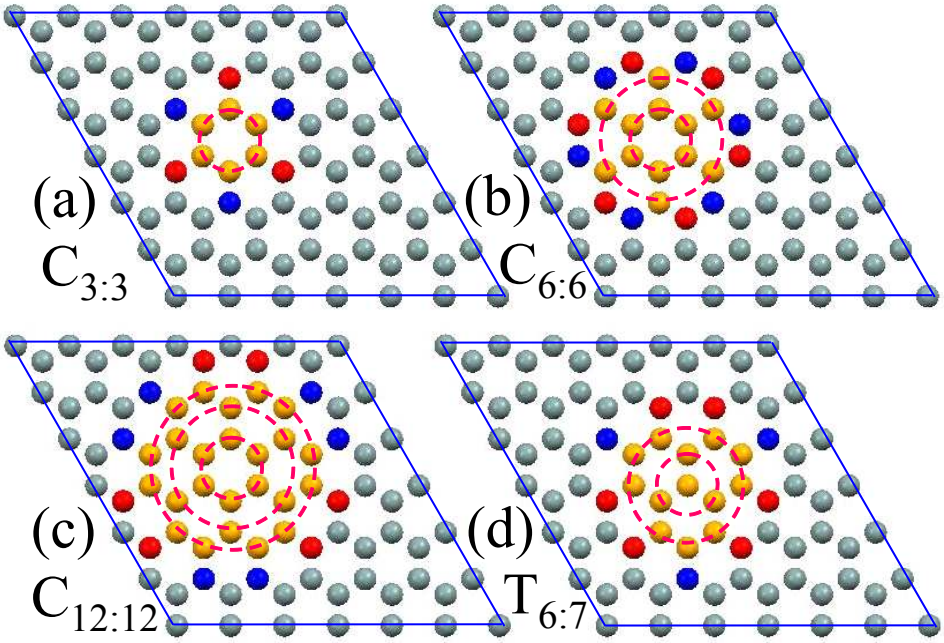

Fig. 6.1 : (a)-(c): Schematics of the calculated crystalline structures for balanced non-passivated circular shaped $C_{3:3}$, $C_{6:6}$ and $C_{12:12}$ GNM structures, respectively; (d) the same for unbalanced non-passivated triangular shaped $T_{6:7}$ GNM structure. Edge carbon atoms are in blue and red color to represent A and B sites, respectively. For convenience, positions of removed atoms are indicated in orange.

Table 6.1: The number of removed atoms on A and B sites and their difference Δ_{AB}. magnetic moment M(μ_B), total energies E (in eV) for ferrimagnetic(FMi), antiferromagnetic(AF) and nonmagnetic(NM) states and defect formation energies E_f (in eV) for different GNM structures. The non-passivated $C_{3:3}$, $C_{6:6}$,$C_{12:12}$, and $T_{6:7}$ and passivated $C^H_{12:12}$ GNMs are calculated with 6×6 unit cell, others are calculated with 8×8 unit cell.

Structure	Δ_{AB}	M(μ_B)	E_{total} (eV)			E_f(eV/C)
			PM	AF	Ferri(o)	
$C_{3:3}$	0	0	-590.414	**-591.742**	(-591.185)	2.81
$C_{6:6}$	0	0	**-528.112**	unstable	unstable	2.10
$C_{12:12}$	0	0	-406.137	**-408.953**	(-407.659)	1.402
$T_{6:7}$	1	3.99	-516.732	unstable	**-518.255** (-517.630)	1.98
$T^H_{6:7}$	1	10^{-4}	-1089.046	unstable	-1089.046	0.142
$T^H_{10:12}$	2	1.80	-1015.387	unstable	**-1015.403**	0.120
$T^H_{15:18}$	3	2.16	-923.346	unstable	**-923.365**	0.103
$T^H_{21:25}$	4	3.62	-813.104	unstable	**-813.223**	0.084
$S^H_{19:21}$	2	1.04	-862.346	unstable	**-862.348**	0.082
$P^H_{18:21}$	3	2.15	-872.125	unstable	**-872.147**	0.156
$C^H_{3:3}$	0	0	**-627.565**	unstable	unstable	0.22
$C^H_{12:12}$	0	0	**-481.358**	unstable	unstable	0.078
$R^H_{24:24}$	0	0	**-795.267**	unstable	unstable	0.070
$P'^H_{18:19}$	1	10^{-4}	-887.147	unstable	-887.147	0.075

with opposite orientation. The magnetic moment is slightly larger than that of graphene nanoribbons which is ∼0.43 μ_B [SCL06b].

We now discuss the case of a 3-ring defect $C_{12:12}$ GNM [Figure 6.1(c)]. The total energy calculations show that the ground state is AF with a magnetic moment of 0.45 μ_B per edge atom for each spin on each sublattice with opposite orientation [Figure 6.4]. The FM state is lower by 0.127 eV per edge atom compared to PM state, and the spin configuration is further stabilized by 0.107 eV per edge atom as a result of the AF coupling between neighboring atoms on different sublattice with opposite spin orientations [see TABLE 6.1].

The 1-ring and 3-ring defect $C_{3:3}$ and $C_{12:12}$ structures considered above present no net permanent magnetic moment, since the spin-polarized edge atoms appear in pair with opposite orientations, resulting in AF ground state with balanced spin-up and spin-down sublattices [Figure 6.3 and 6.4]. However, in a view of spintronic applications, it would be much more interesting to find the GNM structures with nonzero net magnetic moment. This can be actually done by building unbalanced sublattice [Figure 6.1(d)]. We found that the ground state of this unbalanced-defect triangular structure $T_{6:7}$ turns out to be ferrimagnetic (FMi) with total net moment of 3.987 μ_B per unit cell [Figure 6.5]. This moment originates from each edge atom's dangling bond (σ-bond) with spin moment of 1 μ_B providing the magnetic moment of 6(red)-3(blue)=3μ_B in addition to contribution from π-bond equal to 1 μ_B according to total number difference between atoms on A and B sublattice Δ_{AB}.

Dangling bonds at the edge C atoms of non-passivated GNM are strongly chemically

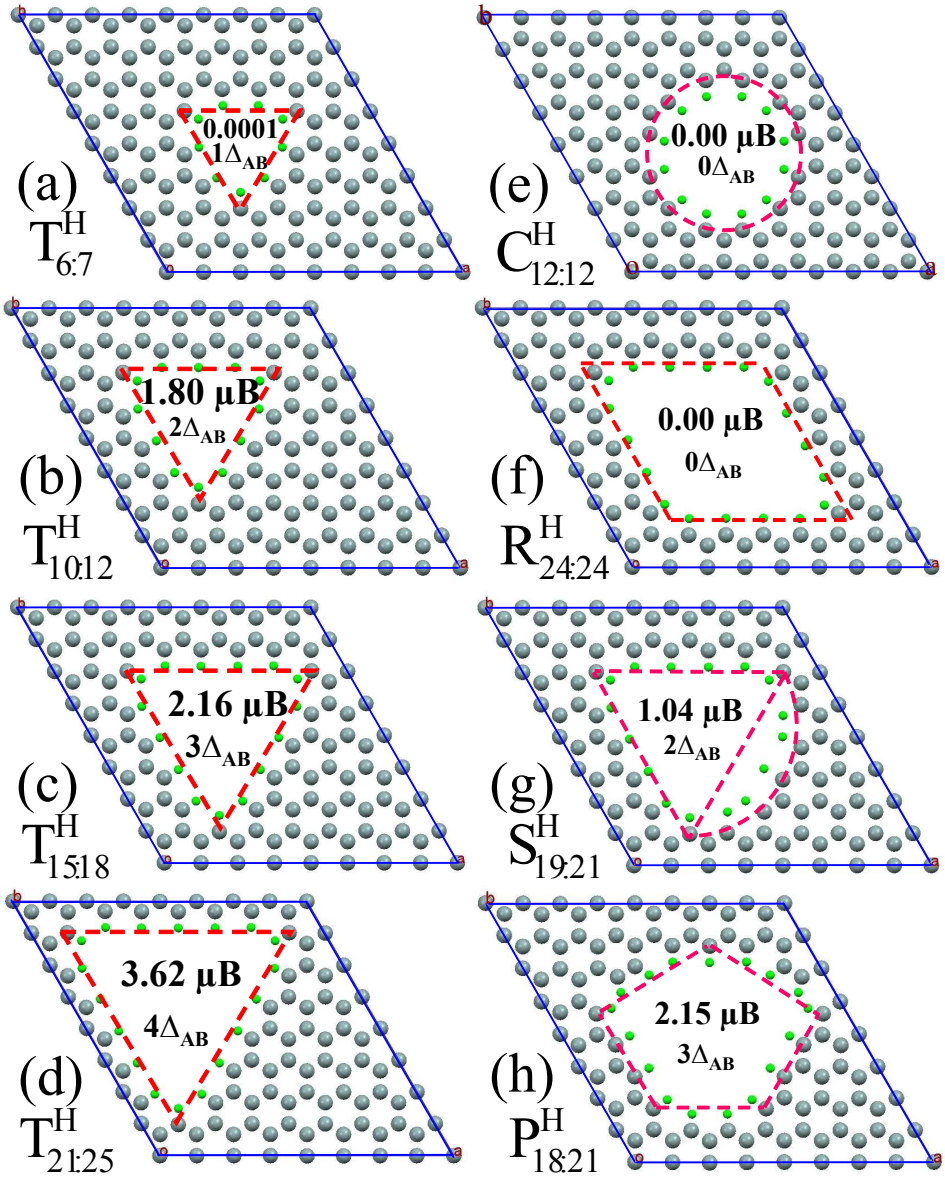

Fig. 6.2 : H-passivated GNMs with triangular shapes: (a) $T^{H}_{6:7}$, (b)$T^{H}_{10:12}$, (c)$T^{H}_{15:18}$, (d) $T^{H}_{21:25}$; with circled shape (e) $C^{H}_{12:12}$; with rhombic shape (f) $R^{H}_{24:24}$; with sector shape (g) $S^{H}_{19:21}$; and with pentagon shape (h) $P^{H}_{18:21}$. The corresponding net magnetic moments for each structure are also indicated.

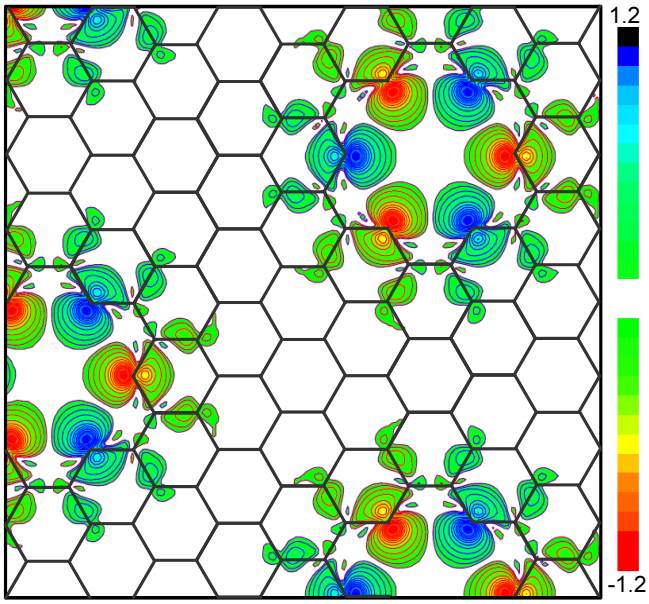

Fig. 6.3 : Spin density ($\mu_B/\text{Å}^2$) distribution for the pure graphene nanomesh $C_{3:3}$.

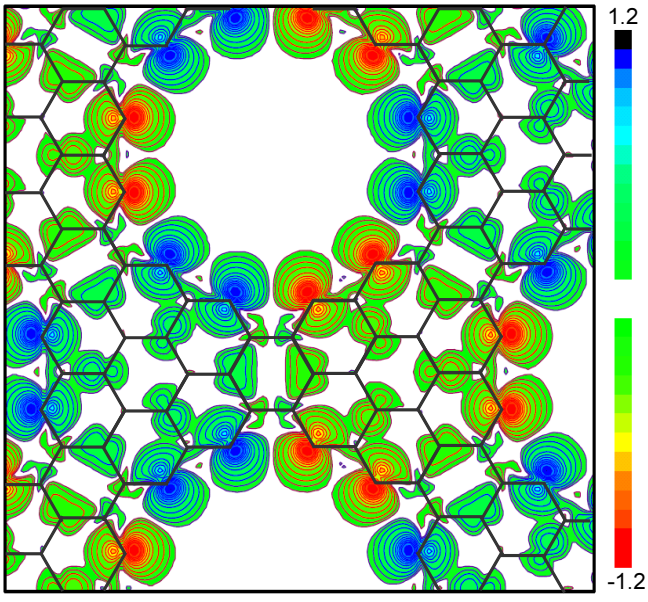

Fig. 6.4 : Spin density ($\mu_B/\text{Å}^2$) distribution for the pure graphene nanomesh $C_{12:12}$.

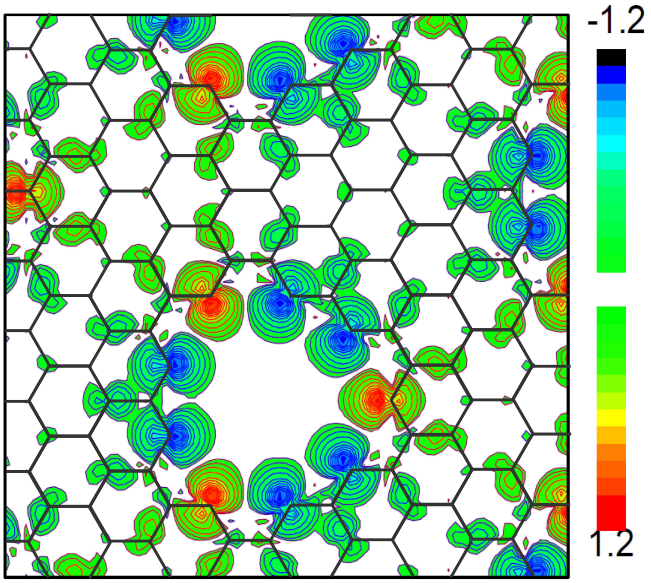

Fig. 6.5 : Spin density ($\mu_B/\text{Å}^2$) distribution for the pure graphene nanomesh $T_{6:7}$.

reactive[BK08], which leads to hole formation energy of pure GNM higher than 1 eV/C [see TABLE 6.1]. Thus edge C atoms are likely to be passivated by light elements. We used hydrogen for passivation of edge C atoms and considered basic geometrical GNM shapes (Figure 6.2) for which the GNM hole formation energy is dramatically decreased due to passivation of dangling bonds [see TABLE 6.1]. For triangular holes, one can see that the formation energy decays as a function of hole dimension. At the same time, the magnetic moment increases and is roughly proportional to the GNM hole size. When the triangular hole size is increased, one observes that the net moment gets bigger [Figure 6.2(b,c and d)] and reaches 3.62 μ_B for the biggest hole shown in Figure 6.2(d). It is interesting to note that Lieb's theorem was originally formulated for even A+B number of atoms, and indeed the obtained values for $T^H_{10:12}$ and $T^H_{21:25}$ follow Lieb's theorem predictions. However, there is an exception for non-triangular case of ($S^H_{19:21}$) with total sum of A and B being even, which is not well accounted by Lieb's theorem. In addition, one can see from TABLE 6.1 that the formation energy values of triangular GNMs decrease as a function of hole size and are comparable to those of the non-magnetic configurations.

In Figure 6.6(a) we summarize aforementioned results including the calculated net magnetic moments for circular ($C^H_{12:12}$), rhombic ($R^H_{24:24}$), sector ($S^H_{19:21}$) and pentagon ($P^H_{18:21}$) GNM shapes represented in Figure 6.2(e)-(h), respectively. In addition, the curves contain the net magnetic moment values for alternative pentagon shape GNM, $P'^H_{18:19}$, obtained from $P^H_{18:21}$ by adding 2 A sites to complete 2 hexagons in upper left and upper right 6-rings in Figure 6.2(h). Even though the overall trend of the calculated values qualitatively follows the Lieb's theory, differences are observed, and first-principles calculations do not always correspond to Δ_{AB}, even for the case with A+B is even of $S^H_{19:21}$ as we have already mentioned. In fact, we can ascribe the structures with odd

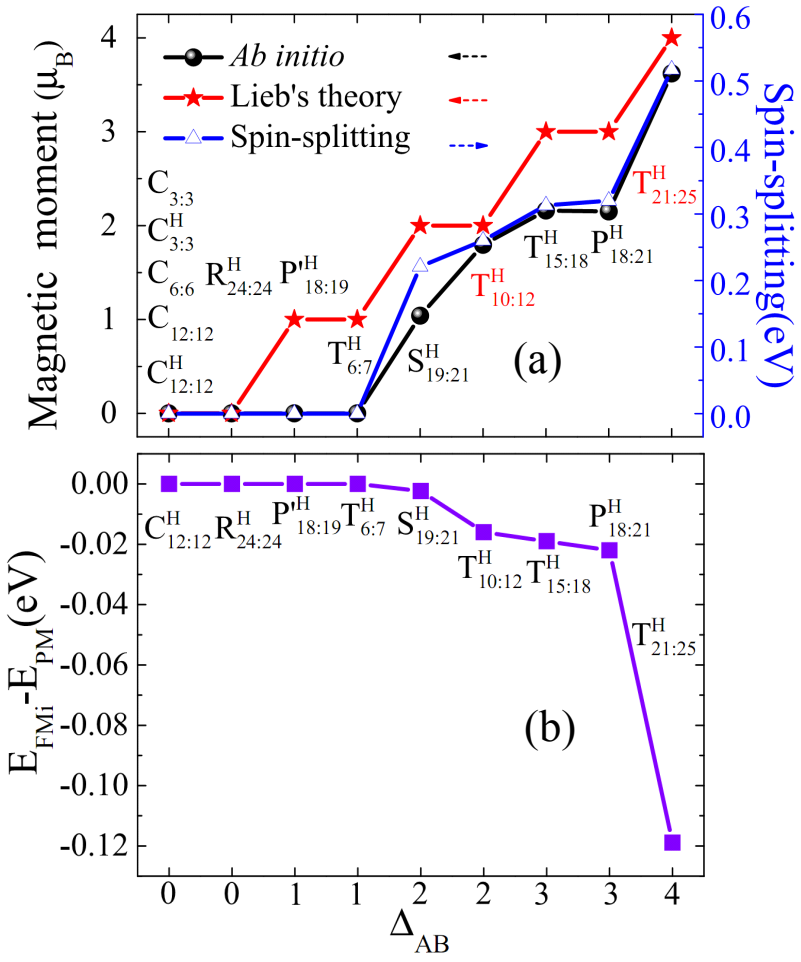

Fig. 6.6 : (a) Total magnetic moment (μ_B/cell) (left) and spin-splitting (right) as a function of Δ_{AB} for various GNM geometries, where $P'^H_{18:19}$ is transformed from a pentagon structure ($P^H_{18:21}$) by adding 2 A atoms to the 2 opened hexagons. The result of the Lieb's theorem prediction is also given for comparison. The even number of A+B structures $T^H_{10:12}$ and $T^H_{21:25}$ are shown in red color to indicate the well agreement with Lieb's theorem prediction. (b) Energy difference between ferrimagnetic and paramagnetic states.

number of A+B atoms, i.e. $T^H_{6:7}$, $P'^H_{18:19}$, $T^H_{15:18}$, $P^H_{18:21}$ as well as sector shape $S^H_{19:21}$ GNMs to intermediate regime between nonmagnetic and highly magnetic regimes. This regime provides a root towards design of magnetic GNM supermeshes. It is worth to note that the possible mechanism for the deviation from the Lieb's theorem of the moment value for the sector shape GNM $S^H_{19:21}$ compared to $T^H_{10:12}$ where A+B is even for both, could be attributed to larger amount of armchair edges (not favorable for moment formation) in $S^H_{19:21}$ structure.

To further elucidate the origin of magnetism in GNM structures, we compute the total and partial density of states (DOS) for considered GNMs. Figure 6.7(a)-(d) give the total DOS for triangular shape GNMs shown in Figure 6.2(a)-(d), respectively. The exchange splitting between majority and minority spins mainly originates from p_z orbitals, as clearly seen from Figure 6.7(c′) where the projected density of states (pDOS) on edge atoms for $T^H_{15:18}$ is plotted. More interestingly, exchange splitting and energy differences between FM and PM states also increase with Δ_{AB} following the same trend as the net magnetic moment [see Figure 6.6(a) and (b)], reaching values of 0.5 eV and 0.12 eV, respectively. These large exchange splitting values suggest that the magnetism could be preserved at room temperature which look very promising for room temperature graphene spintronics developments. Density of states of structures like $T^H_{10:12}$ provides with the evidence for the presence of localized electrons on the zigzag edges similar to the perfect GNR [SCL06b]. The smearing of the p_z peak and increase of the number of states at the Fermi level (metallization) suggest the electron delocalization on edges and switch from AFM to FM configuration similar to the case of partially oxidized graphite edges [BMdSK11]. We have plotted the spin density figures for the localized and delocalized cases for illustrate dramatic changes in localization of electrons with vanishing of pseudogap in density of states (see Figure 6.8).The cause of such delocalization of the unpaired electrons on the edges of GNM holes can be attributed to combination of sublattice degeneracy breaking and deviation from the perfect shapes of the graphene nanoribbon.

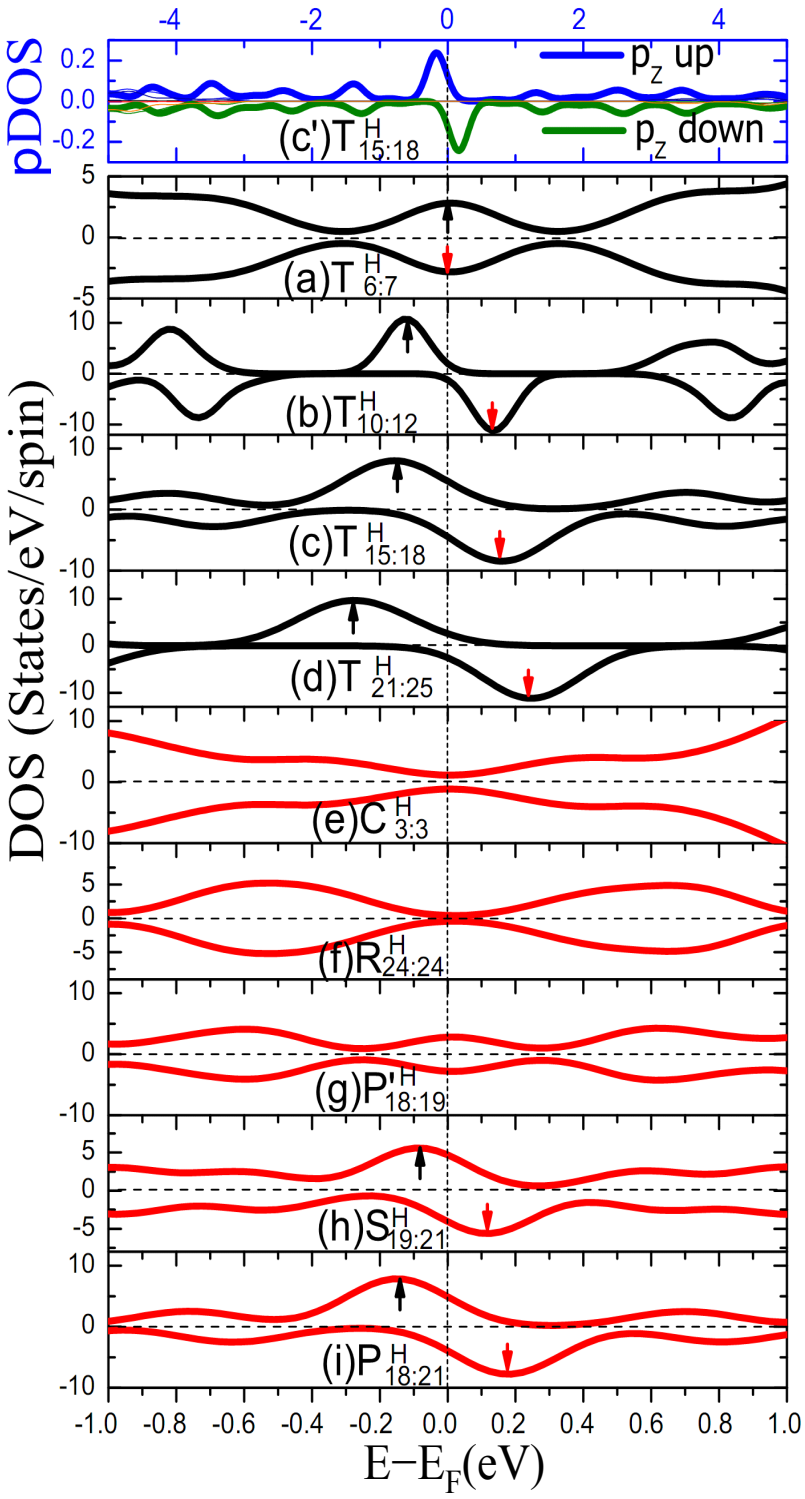

Fig. 6.7 : Density of states for triangular GNMs of (a) $T^H_{6:7}$, (b) $T^H_{10:12}$, (c) $T^H_{15:18}$, (d) $T^H_{21:25}$, (e) $C^H_{3:3}$, (f) $R^H_{24:24}$, (g)$P'^H_{18:19}$, (h) $S^H_{19:21}$, and (i) $P^H_{18:21}$ the peaks around Fermi level are marked with arrows. It can be seen that only p_z state contributes to the moment from (c′) projected density of states of one edge atom in the $T^H_{15:18}$ GNM.

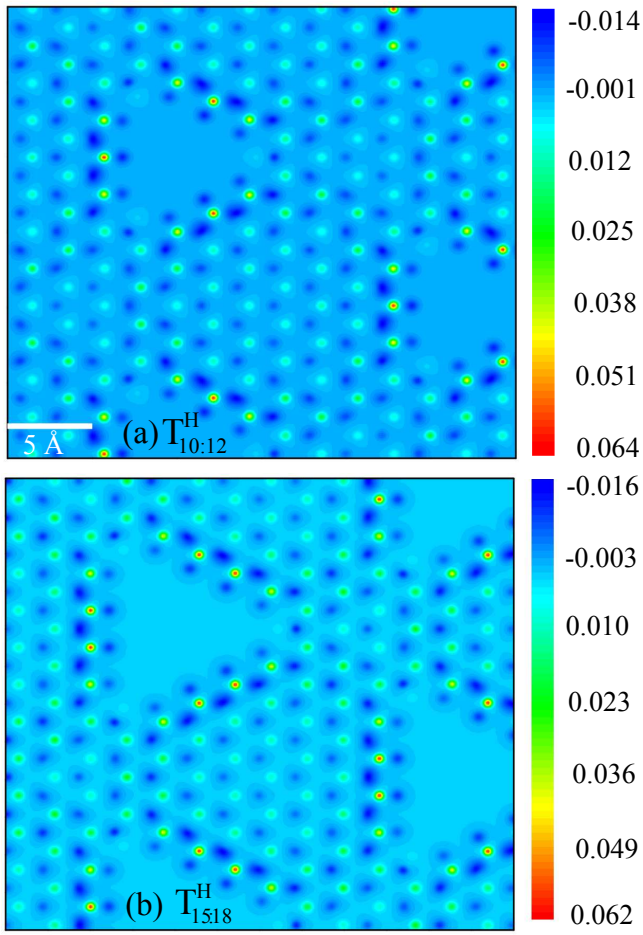

Fig. 6.8 : Spin density ($\mu_B/\text{Å}^2$) distribution for the two types of graphene nanomesh with localized (upper panel) and delocalized (lower panel) unpaired electrons.

6.5 Summary

In conclusion, in this chapter we investigated electronic and magnetic properties in graphene nanomeshes with different geometries using first-principles calculations. For non-passivated GNM with $\Delta_{AB} = 0$, stable non-magnetic states are found for armchair edge termination, while zigzag edge terminations result in antiferromagnetic ground states. These localized magnetic moments however vanish when all edge C-atoms are hydrogen-passivated. In sharp contrast, when $\Delta_{AB} \neq 0$, stable ferri(o)magnetic states are induced with net moment up to 4 μ_B (per 6×6 unit cell) originating from dangling bonds of edge atoms. Furthermore, for hydrogen-passivated GNM, the formation energy is dramatically decreased, and ground state is found to strongly depend on the vacancies shape and size. Our calculations reveal the existence of three magnetic regimes which depend on Δ_{AB}: (i) highly magnetic GNMs obeying Lieb's theorem corresponding to triangular shaped holes with even A+B; (ii) GNMs with quenched magnetic state due to complete chemical bond reconstruction with $\Delta_{AB} = 1$ and trivially nonmagnetic state with $\Delta_{AB} = 0$; and (iii) GNMs following intermediate regime between magnetic and quenched magnetic states, i.e. triangular GNMs with odd A+B and more complicated structures including both even (e.g. sector shaped GNM) and odd (e.g. pentagon shaped GNM) A+B. We show that large triangular GNMs could be as robust as non-triangular GNMs providing possible solution to overcome one of crucial challenges for the sp-magnetism. Moreover, significant exchange splitting values as large as ~ 0.5 eV can be obtained for highly asymmetric structures evidencing the potential of graphene nanomesh for room temperature carbon based spintronics.

Chapter 7

Conclusions

In this thesis, we have investigated spintronic phenomena in magnetic tunnel junctions and graphene-based systems.

The phenomena investigated included interlayer exchange coupling in magnetic tunnel junctions, perpendicular magnetic anisotropy at Fe(Co)|MgO and graphene|Co interfaces, intrinsic magnetism in graphene nanomeshes, magnetic insulator proximity induced spin-polarization, tunable Dirac cone and unusual magnetic ordering in graphene.

For magnetic tunnel junctions, a long debated interlayer exchange coupling behavior in Fe|MgO|Fe tunnel junctions has been systematically investigated and resolved. Namely, it was believed that AF IEC is caused by the presence of oxygen vacancies. We have shown that in pure Fe|MgO|Fe MTJs, the coupling may become antiferromagnetic in the fully optimized system by complete structural relaxation. Furthermore, it is demonstrated that the oxidation conditions have a strong impact on the behavior of interlayer exchange coupling. Namely, the antiferromagnetic IEC is strongly enhanced in the presence of oxygen vacancies in agreement with previous studies while it is decreased by overoxidation and may even become ferromagnetic for sufficiently high oxygen concentration at the Fe|MgO interface.

Next, we studied and clarified the origin of large perpendicular magnetic anisotropy at Fe|MgO interfaces. We provided the explanation for the PMA by the band spectra analysis with the presence of spin-orbit coupling and showed that the PMA are mainly caused by: (i) the spin-orbit coupling with out-of-plane quantization orientation axis causing larger splitting for the degenerated Δ_5 $[d_{xz(yz)}]$ symmetric orbitals compared to those in case of SOC with in-plane quantization orientation axis; (ii) the hybridization between d_{z2} and $d_{xz(yz)}$ which enhances the effect from degeneracy lift of Δ_5 symmetric orbitals; and (iii) the hybridization between Fe-3d_{z2} and O-2p_z orbitals which further enhances the effect from (ii). We also explains the weakening of the PMA in case of contaminated Fe|MgO interfaces.

Furthermore, we showed that PMA and TMR can reach their maxima for pure Fe|MgO interfaces. This is due to the fact that the most important contribution to PMA originates from Δ bands (especially the Δ_1 band) which are also responsible for the Bloch states symmetry-based spin filtering causing large TMR ratios. This correlation further proves the potential of MgO-based magnetic tunnel junctions for realizing next-generation high-density non-volatile memory and logic chips with high thermal stability and low critical current for current-induced magnetization switching in magnetic tunnel junctions

with ferromagnetic electrodes.

We have also investigated the magnetocrystalline anisotropy at ferromagnetic metal and graphene interfaces, such as graphene on Co, where the lattices match very well in the system. Our calculations showed that for Co films thicker than three monolayers, the PMA can be preserved. This is in agreement with experimental results showing that the PMA can be preserved for 2-7 monolayers of Co thickness. Recent experiments show also that the PMA may even be observed for 50 monolayers in Co/Graphite systems, which is very promising. Even though, in our calculations, graphene does not improve the PMA of thicker Co films, for a single layer of Co film, with graphene coverage, the easy axis switches to out-of-plane with PMA values larger than that of Co/Pt interface. In the Co/Graphene system, we also saw the reduction of magnetic moment and work function, which are in good agreement with experiments.

We also investigated the proximity effects from magnetic insulator EuO on graphene electronic and magnetic properties. The average spin-polarization of around 12% have been found. At the same time when tuning the Fermi energy, much larger spin-polarization including half metallic state may be obtained. Furthermore, we showed the possibility to tune Dirac cone in graphene by placing graphene on EuO surface at different distances. Finally, an unusual magnetic order is found in graphene on EuO substrate. We saw that EuO is a very promising substrate to inject spin into graphene and can cause so many interesting phenomena.

Besides to the substrates caused magnetism, we also studied the possibility of inducing intrinsic magnetism in recently realized graphene nonomesh structures. We showed that the shape and size of nanomesh have strong influence on the magnetism. For triangular-shaped holes, the obtained net magnetic moments increase with the number difference of removed A and B sites in agreement with Lieb's theorem for even A + B. For odd A + B triangular meshes and all cases of nontriangular nanomeshes, including the one with even A + B, Lieb's theorem does not hold anymore, which can be partially attributed to the introduction of armchair edges. In addition, large triangular-shaped GNMs could be as robust as nontriangular GNMs, providing a possible solution to overcome one of the crucial challenges for the sp magnetism. Finally, the calculated large exchange-splitting values suggest the potential of GNM for room-temperature carbon-based spintronics.

Chapter 8

First-principles calculations

In this thesis, we mainly use density-functional theory (DFT) for the calculations. The details of the theory, can be found in papers by Hohenberg et al, and by Kohn et al the reference [HK64, KS65] or the book 'electronic structure' by Ricahrd M. Martin [Mar04]. But since we use DFT to calculate spintronic phenomena, I will give a brief introduction of DFT calculation of spin-resolved total energy and how spin-orbit coupling is included in VASP code. (vasp guide book)

For spin-polarized (magnetic) materials, one arrives at an energy functional, which depends both on the majority and on the minority spin densities or total density

$$n(\mathbf{r}) = n^{\uparrow}(\mathbf{r}) + n^{\downarrow}(\mathbf{r}) \tag{8.1}$$

and magnetization density

$$m(\mathbf{r}) = n^{\uparrow}(\mathbf{r}) - n^{\downarrow}(\mathbf{r}) \tag{8.2}$$

The Kohn-Sham scheme attempts to calculate this functional from an effective one-electron theory, where the majority and minority electrons move in an effective potential that is constructed to generate the ground-state density for these electrons. This theory is a practical way of calculating charge and magnetization densities, and in addition it is possible to write down an expression for the total energy of the system,

$$E[n^{\uparrow}(\mathbf{r}), n^{\downarrow}(\mathbf{r})] = T_{op}[n^{\uparrow}(\mathbf{r}), n^{\downarrow}(\mathbf{r})] + \int n(\mathbf{r})v(\mathbf{r})d^3r + \frac{1}{2}\int\int e^2\frac{n(\mathbf{r})\cdot n(\mathbf{r}')}{|\mathbf{r}-\mathbf{r}'|}d^3r d^3r' + E_{xc}[n^{\uparrow}(\mathbf{r}), n^{\downarrow}(\mathbf{r})]. \tag{8.3}$$

Here $T_{op}[n^{\uparrow}(\mathbf{r}), n^{\downarrow}(\mathbf{r})]$ is the kinetic energy of one particle (or independent) electrons, the second term contains interactions between the electrons and an external potential, like the one given by a nucleus, and the third term is the classical Hartree interaction. The last term, the exchange-correlation energy, for which useful parametrizations as functions of $n^{\uparrow}(\mathbf{r})$ and $n^{\downarrow}(\mathbf{r})$ exist [CA80], is defined as the difference between the true (unknown) energy functional and the three first terms on the right-hand side of equation(8.3).

The Kohn-Sham equation with spin-up and spin-down effective potentials

$$[-\frac{\nabla^2}{2} + V_{eff}^{\uparrow(\downarrow)}]\Psi_i^{\uparrow(\downarrow)} = E_i^{\uparrow(\downarrow)}\Psi_i^{\uparrow(\downarrow)} \tag{8.4}$$

determines the one-particle wave functions from which the majority and minority spin densities can be calculated as

$$n_{op}^{\uparrow(\downarrow)}(\mathbf{r}) = \sum_{i=1} |\psi_i^{\uparrow(\downarrow)}|^2 \tag{8.5}$$

The effective potentials in equation(8.4) are different for the two spin directions due to differences in the exchange-correlation potential,

$$V_{eff}^{\uparrow(\downarrow)}(\mathbf{r}) = v(\mathbf{r}) + \int e^2 \frac{n(\mathbf{r}')}{|\mathbf{r} - \mathbf{r}'|} d^3r' + \mu_{xc}^{\uparrow(\downarrow)}(\mathbf{r}) \tag{8.6}$$

where $\mu_{xc}^{\uparrow(\downarrow)}(\mathbf{r}) = dE_{xc}/dn^{\uparrow(\downarrow)}$

Hence the simplest form of spin-polarized calculation treats spin-up and spin-down electrons separately in the Kohn-Sham equation. Spin-up and spin-down densities are then calculated by occupation of the lowest eigenvalues of the two separate Kohn-Sham equations. Since a given $V_{eff}^{\uparrow}(\mathbf{r})$, which may be different from $V_{eff}^{\uparrow}(\mathbf{r})$, may lead to more occupied (below Fermi level E_F) spin-up states $n_i^{\uparrow}$ than spin-down states $n_i^{\downarrow}$, spin polarization can occur. With a self-consistent spin and magnetization density the magnetic moment is calculated as $\int m(\mathbf{r}) d^3r$ (in μ_B) and the total energy can be calculated from equation 8.3.

If spin-orbit interaction is not included, the energy does not depend on the direction of the magnetic moment, which means rotating all magnetic moments by the same angle gives the same energy. Hence there is no need to define the spin quantization axis direction, if spin-orbit coupling is not included. When spin-orbit interaction is included, spin-orbit coupling couples the spin to the crystal structure. One needs to set a quantization axis for spin $S_{axis} = s_x, s_y, s_z$. In VASP, the default S_{axis} is setting to (0,0,1). All magnetic moments are given with respect to the axis (s_x, s_y, s_z). Therefore, with respect to the lattice vectors the components of the magnetization are given by

$$m_x = cos(\beta)cos(\alpha)m_x^{axis} - sin(\alpha)m_y^{axis} + sin(\beta)cos(\alpha)m_z^{axis}, \tag{8.7}$$

$$m_y = cos(\beta)cos(\alpha)m_x^{axis} + cos(\alpha)m_y^{axis} + sin(\beta)sin(\alpha)m_z^{axis}, \tag{8.8}$$

and

$$m_x = -sin(\beta)m_x^{axis} + cos(\beta)m_z^{axis} \tag{8.9}$$

Where m^{axis} is the externally visible magnetic moment, α is the angle between the S_{axix} vector (s_x, s_y, s_z) and the cartesian vector $\hat{x}$, and β is the angle between the vector S_{axix} and the vector $\hat{z}$.

$$\alpha = atan\frac{s_y}{s_x}; \beta = atan\frac{|s_x^2 + s_y^2|}{s_z} \tag{8.10}$$

The inverse transformation is given by

$$m_x^{axis} = cos(\beta)cos(\alpha)m_x + cos(\beta)sin(\alpha)m_y + sin(\beta)m_z, \tag{8.11}$$

$$m_y^{axis} = -sin(\alpha)m_x + cos(\alpha)m_y, \tag{8.12}$$

and

$$m_z^{axis} = sin(\beta)cos(\alpha)m_x + sin(\beta)sin(\alpha)m_y + cos(\beta)m_z \tag{8.13}$$

For the default setting in VASP (s_x, s_y, s_z)=(0,0,1), both angles α and β are zero. In this case, the internal representation is simply equivalent to the external representation $m_i = m_i^{axis}$.

Another important case is m_x^{axis}=0 and m_y^{axis}=0, so that,

$$m_x = sin(\beta)cos(\alpha)m_z^{axis} = m_z^{axis}s_x/\sqrt{s_x^2 + s_y^2 + s_z^2}, \tag{8.14}$$

$$m_y = sin(\beta)sin(\alpha)m_z^{axis} = m_z^{axis}s_y/\sqrt{s_x^2 + s_y^2 + s_z^2}, \tag{8.15}$$

and

$$m_z = cos(\beta)m_z^{axis} = m_z^{axis}s_z/\sqrt{s_x^2 + s_y^2 + s_z^2} \tag{8.16}$$

Now the magnetic moment is parallel to the vector S_{axis}. Thus there are two ways to rotate the spins in an arbitrary direction, either by changing the initial magnetic moments or by changing S_{axis}, and they should, in principle, yield the same result.

So by changing the S_{axis} [or initial magnetic moment], one can calculate the total energy which depends on S_{axis} [or initial magnetic moment], and thus can easily get the magnetic anisotropy. For the details of the total energy calculation and the parameters to include spin-orbit coupling by using VASP program, please read the guide book of VASP from website: *www.vasp.at*

Bibliography

[BBB+03] M. Bowen, M. Bibes, A. Barthelemy, J.-P. Contour, A. Anane, Y. Lemaitre, and A. Fert. Nearly total spin polarization in lasrmnofrom tunneling experiments. *Applied Physics Letters*, 82(2):233–235, 2003.

[BBC+03] D E Burgler, M Buchmeier, S Cramm, S Eisebitt, R R Gareev, P Grunberg, C L Jia, L L Pohlmann, R Schreiber, M Siegel, Y L Qin, and A Zimina. Exchange coupling of ferromagnetic films across metallic and semiconducting interlayers. *Journal of Physics: Condensed Matter*, 15(5):S443, 2003.

[BBF+88] M. N. Baibich, J. M. Broto, A. Fert, F. Nguyen Van Dau, F. Petroff, P. Etienne, G. Creuzet, A. Friederich, and J. Chazelas. Giant magnetoresistance of (001)fe/(001)cr magnetic superlattices. *Phys. Rev. Lett.*, 61:2472–2475, Nov 1988.

[BBVD02] D. Bagrets, A. Bagrets, A. Vedyayev, and B. Dieny. Influence of $s - d$ interfacial scattering on the magnetoresistance of magnetic tunnel junctions. *Phys. Rev. B*, 65:064430, Jan 2002.

[BC91a] P. Bruno and C. Chappert. Oscillatory coupling between ferromagnetic layers separated by a nonmagnetic metal spacer. *Phys. Rev. Lett.*, 67:1602–1605, Sep 1991.

[BC91b] P. Bruno and C. Chappert. Oscillatory coupling between ferromagnetic layers separated by a nonmagnetic metal spacer. *Phys. Rev. Lett.*, 67:2592–2592, Oct 1991.

[BC92] P. Bruno and C. Chappert. Ruderman-kittel theory of oscillatory interlayer exchange coupling. *Phys. Rev. B*, 46:261–270, Jul 1992.

[BFC+02] A. Barthelemy, A. Fert, J-P. Contour, M. Bowen, V. Cros, J.M. De Teresa, A. Hamzic, J.C. Faini, J.M. George, J. Grollier, F. Montaigne, F. Pailloux, F. Petroff, and C. Vouille. Magnetoresistance and spin electronics. *Journal of Magnetism and Magnetic Materials*, 242-245, Part 1(0):68 – 76, 2002.

[BFD07] L. Brey, H. A. Fertig, and S. Das Sarma. Diluted Graphene Antiferromagnet. *Physical Review Letters*, 99(11):116802, September 2007.

[BGS+09] Kirill I. Bolotin, Fereshte Ghahari, Michael D. Shulman, Horst L. Stormer, and Philip Kim. Observation of the fractional quantum hall effect in graphene. *nature*, 462:196, 2009.

[BGSZ89] G. Binasch, P. Grünberg, F. Saurenbach, and W. Zinn. Enhanced magnetoresistance in layered magnetic structures with antiferromagnetic interlayer exchange. *Phys. Rev. B*, 39:4828–4830, Mar 1989.

[BK08] D. W. Boukhvalov and M. I. Katsnelson. Chemical Functionalization of Graphene with Defects. *Nano Letters*, 8:4373–4379, December 2008.

[BK11] Danil W. Boukhvalov and Mikhail I. Katsnelson. sp-electron magnetic clusters with a large spin in graphene. *ACS Nano*, 5(4):2440–2446, 2011.

[BKK11] Florian Banhart, Jani Kotakoski, and Arkady V. Krasheninnikov. Structural defects in graphene. *ACS Nano*, 5(1):26–41, 2011.

[Blo94] P. E. Blochl. Projector augmented-wave method. *Phys. Rev. B*, 50:17953–17979, Dec 1994.

[BMdSK11] D. W. Boukhvalov, S. Moehlecke, R. R. da Silva, and Y. Kopelevich. Effect of oxygen adsorption on magnetic properties of graphite. *Phys. Rev. B*, 83(23):233408, June 2011.

[Bou10] D. W. Boukhvalov. Modeling of hydrogen and hydroxyl group migration on graphene. *Phys. Chem. Chem. Phys.*, 12:15367, 2010.

[BR84] Yu A Bychkov and E I Rashba. Oscillatory effects and the magnetic susceptibility of carriers in inversion layers. *Journal of Physics C: Solid State Physics*, 17(33):6039, 1984.

[Bru89] Patrick Bruno. Tight-binding approach to the orbital magnetic moment and magnetocrystalline anisotropy of transition-metal monolayers. *Phys. Rev. B*, 39:865–868, Jan 1989.

[Bru95] P. Bruno. Theory of interlayer magnetic coupling. *Phys. Rev. B*, 52:411–439, Jul 1995.

[Bru99] P Bruno. Theory of interlayer exchange interactions in magnetic multilayers. *Journal of Physics: Condensed Matter*, 11(48):9403, 1999.

[BSL+06] Claire Berger, Zhimin Song, Xuebin Li, Xiaosong Wu, Nate Brown, Cecile Naud, Didier Mayou, Tianbo Li, Joanna Hass, Alexei N. Marchenkov, Edward H. Conrad, Phillip N. First, and Walt A. de Heer. Electronic confinement and coherence in patterned epitaxial graphene. *Science*, 312(5777):1191–1196, 2006.

[BZJ+10] J. Bai, X. Zhong, S. Jiang, Y. Huang, and X. Duan. Graphene nanomesh. *Nature Nanotechnology*, 5:190–194, March 2010.

[BZSM01] W. H. Butler, X.-G. Zhang, T. C. Schulthess, and J. M. MacLaren. Spin-dependent tunneling conductance of Fe|MgO|Fe sandwiches. *Phys. Rev. B*, 63:054416, Jan 2001.

[BZV+05] WH Butler, XG Zhang, S Vutukuri, M Chshiev, and TC Schulthess. Theory of tunneling magnetoresistance for epitaxial systems. *IEEE TRANSACTIONS ON MAGNETICS*, 41:2645, 2005.

[BZW+97] W. H. Butler, X.-G. Zhang, Xindong Wang, Jan van Ek, and J. M. MacLaren. Electronic structure of fm—semiconductor—fm spin tunneling structures. *Journal of Applied Physics*, 81(8):5518–5520, 1997.

[CA80] D. M. Ceperley and B. J. Alder. Ground state of the electron gas by a stochastic method. *Phys. Rev. Lett.*, 45:566–569, Aug 1980.

[CFP67] I A CAMPBELL, A FERT, and A R POMEROY. Evidence for 2 current conduction iron. *Philosophical Magazine*, 15:977, 1967.

[CKF09a] J. Cervenka, M. I. Katsnelson, and C. F. J. Flipse. Room-temperature ferromagnetism in graphite driven by two-dimensional networks of point defects. *nature physics*, 5:840, 2009.

[ČKF09b] J. Červenka, M. I. Katsnelson, and C. F. J. Flipse. Room-temperature ferromagnetism in graphite driven by two-dimensional networks of point defects. *Nature Physics*, 5:840–844, November 2009.

[CMS85] P. F. Carcia, A. D. Meinhaldt, and A. Suna. Perpendicular magnetic anisotropy in pd/co thin film layered structures. *Applied Physics Letters*, 47(2):178–180, 1985.

[CMW96] A. Chaiken, R. P. Michel, and M. A. Wall. Structure and magnetism of fe/si multilayers grown by ion-beam sputtering. *Phys. Rev. B*, 53:5518–5529, Mar 1996.

[CNGP+09] A. H. Castro Neto, F. Guinea, N. M. R. Peres, K. S. Novoselov, and A. K. Geim. The electronic properties of graphene. *Rev. Mod. Phys.*, 81:109–162, Jan 2009.

[CNR+] Johann Coraux, Alpha T. NDiaye, Nicolas Rougemaille, Chi Vo-Van, Amina Kimouche, Hong-Xin Yang, Mairbek Chshiev, Nedjma Bendiab, Olivier Fruchart, , and Andrea K. Schmid. Growth, structure and magnetism of cobalt thin films intercalated between graphene and iridium. to be published.

[CR09] A. Cresti and S. Roche. Range and correlation effects in edge disordered graphene nanoribbons. *New Journal of Physics*, 11(9):095004, September 2009.

[CTK+08] M. Chshiev, I. Theodonis, A. Kalitsov, N. Kioussis, and W.H. Butler. Voltage dependence of spin transfer torque in magnetic tunnel junctions. *Magnetics, IEEE Transactions on*, 44(11):2543 –2546, nov. 2008.

[CWT+09] Y. F. Chiang, Jared J. I. Wong, X. Tan, Yan Li, K. Pi, W. H. Wang, H. W. K. Tom, and R. K. Kawakami. Oxidation-induced biquadratic coupling in co/fe/mgo/fe(001). *Phys. Rev. B*, 79:184410, May 2009.

[CYL08] L. Chen, D. Yu, and F. Liu. Magnetism in nanopatterned graphite film. *Applied Physics Letters*, 93(22):223106, December 2008.

[DCR+08] C. Ducruet, B. Carvello, B. Rodmacq, S. Auffret, G. Gaudin, and B. Dieny. Magnetoresistance in co/pt based magnetic tunnel junctions with out-of-plane magnetization. *Journal of Applied Physics*, 103(7):07A918, 2008.

[DCT+01] T. Dimopoulos, V. Da Costa, C. Tiusan, K. Ounadjela, and H. A. M. van den Berg. Interfacial phenomena related to the fabrication of thin al oxide tunnel barriers and their thermal evolution. *Applied Physics Letters*, 79(19):3110–3112, 2001.

[DdJdB87] H.J.G. Draaisma, W.J.M. de Jonge, and F.J.A. den Broeder. Magnetic interface anisotropy in pd/co and pd/fe multilayers. *Journal of Magnetism and Magnetic Materials*, 66(3):351 – 355, 1987.

[DGC+03] T. Dimopoulos, G. Gieres, S. Colis, J. Wecker, Y. Luo, and K. Samwer. Magnetic tunnel junctions with yttrium oxide barrier. *Applied Physics Letters*, 83(16):3338–3340, 2003.

[DHC+04] T. Dimopoulos, Y. Henry, V. Da Costa, C. Tiusan, and K. Ounadjela. Influence of barrier overoxidation and annealing on the inelastic spin-dependent tunneling in alo[sub x]-based junctions. *Journal of Applied Physics*, 95(11):6936–6938, 2004.

[DKS94a] G. H. O. Daalderop, P. J. Kelly, and M. F. H. Schuurmans. Magnetic anisotropy of a free-standing co monolayer and of multilayers which contain co monolayers. *Phys. Rev. B*, 50:9989–10003, Oct 1994.

[DKS94b] G. H. O. Daalderop, P. J. Kelly, and M. F. H. Schuurmans. Magnetic anisotropy of a free-standing co monolayer and of multilayers which contain co monolayers. *Phys. Rev. B*, 50:9989–10003, Oct 1994.

[DMW+02] P.H. Dederichs, Ph. Mavropoulos, O. Wunnicke, N. Papanikolaou, V. Bellini, R. Zeller, V. Drchal, and J. Kudrnovsky. Importance of complex band structure and resonant states for tunneling. *Journal of Magnetism and Magnetic Materials*, 240:108 – 113, 2002. ¡ce:title¿4th International Symposium on Metallic Multilayers¡/ce:title¿.

[DSA+10] B. Dlubak, P. Seneor, A. Anane, C. Barraud, C. Deranlot, D. Deneuve, B. Servet, R. Mattana, F. Petroff, and A. Fert. Are alo and mgo tunnel barriers suitable for spin injection in graphene? *Applied Physics Letters*, 97(9):092502, August 2010.

[DSAHR11] S. Das Sarma, Shaffique Adam, E. H. Hwang, and Enrico Rossi. Electronic transport in two-dimensional graphene. *Rev. Mod. Phys.*, 83:407–470, May 2011.

[DSD+09] Xu Du, Ivan Skachko, Fabian Duerr, Adina Luican, and Eva Y. Andrei. Fractional quantum hall effect and insulating phase of dirac electrons in graphene. *Nature*, 462:192, 2009.

[DTBF+99a] J. M. De Teresa, A. Barthelemy, A.lamy, A. Fert, J. P. Contour, R. Lyonnet, F. Montaigne, P. Seneor, and A. Vaurès. Inverse tunnel magnetoresistance incosrtio3la0.7sr0.3mno3: New ideas on spin-polarized tunneling. *Phys. Rev. Lett.*, 82:4288–4291, May 1999.

[DTBF+99b] Jose Maria De Teresa, Agnes Barthelemy, Albert Fert, Jean Pierre Contour, Francois Montaigne, and Pierre Seneor. Role of metal-oxide interface in determining the spin polarization of magnetic tunnel junctions. *Science*, 286(5439):507–509, 1999.

[dVKdB+97] J. J. de Vries, J. Kohlhepp, F. J. A. den Broeder, R. Coehoorn, R. Jungblut, A. Reinders, and W. J. M. de Jonge. Exponential dependence of the interlayer exchange coupling on the spacer thickness in mbe-grown fe/sife/fe sandwiches. *Phys. Rev. Lett.*, 78:3023–3026, Apr 1997.

[EKI+10] M. Endo, S. Kanai, S. Ikeda, F. Matsukura, and H. Ohno. Electric-field effects on thickness dependent magnetic anisotropy of sputtered mgocofebta structures. *Applied Physics Letters*, 96(21):212503, 2010.

[EKS99] Yasushi Endo, Osamu Kitakami, and Yutaka Shimada. Interlayer coupling in fesi superlattices. *Phys. Rev. B*, 59:4279–4286, Feb 1999.

[Ell54] R. J. Elliott. Theory of the effect of spin-orbit coupling on magnetic resonance in some semiconductors. *Phys. Rev.*, 96:266–279, Oct 1954.

[ESH+03] P. Esquinazi, D. Spemann, R. Höhne, A. Setzer, K.-H. Han, and T. Butz. Induced Magnetic Ordering by Proton Irradiation in Graphite. *Physical Review Letters*, 91(22):227201, November 2003.

[ET09] T. Enoki and K. Takai. The edge state of nanographene and the magnetism of the edge-state spins. *Solid State Communications*, 149:1144–1150, July 2009.

[FBA+09] Xiaobing Feng, O. Bengone, M. Alouani, S. Lebègue, I. Rungger, and S. Sanvito. Effects of structural relaxation on calculations of the interface and transport properties of fe/mgo(001) tunnel junctions. *Phys. Rev. B*, 79:174414, May 2009.

[FBY+01a] A. Fert, A. Barthelemy, J.Ben Youssef, J.-P. Contour, V. Cros, J.M. De Teresa, A. Hamzic, J.M. George, G. Faini, J. Grollier, H. Jaffres, H. Le Gall, F. Montaigne, F. Pailloux, and F. Petroff. Review of recent results on spin polarized tunneling and magnetic switching by spin injection. *Materials Science and Engineering: B*, 84:1 – 9, 2001.

[FBY+01b] A. Fert, A. Barthelemy, J.Ben Youssef, J.-P. Contour, V. Cros, J.M. De Teresa, A. Hamzic, J.M. George, G. Faini, J. Grollier, H. Jaffres, H. Le Gall, F. Montaigne, F. Pailloux, and F. Petroff. Review of recent results on spin polarized tunneling and magnetic switching by spin injection. *Materials Science and Engineering: B*, 84(1-2):1 – 9, 2001.

[FC68] A. Fert and I. A. Campbell. Two-current conduction in nickel. *Phys. Rev. Lett.*, 21:1190–1192, Oct 1968.

[FDD+93] R. F. C. Farrow, B. Dieny, M. Donath, A. Fert, and B. D. Hermsmeier, editors. *Magnetism and Structure in Systems of Reduced Dimensions*. Plenum Press, New York, 1993.

[Fer07] A. C. Ferrari. Raman spectroscopy of graphene and graphite: Disorder, electron phonon coupling, doping and nonadiabatic effects. *Solid State Communications*, 143:47–57, July 2007.

[FGB+95] A. Fert, P. Grunberg, A. Barthelemy, F. Petroff, and W. Zinn. Layered magnetic structures: interlayer exchange coupling and giant magnetoresistance. *Journal of Magnetism and Magnetic Materials*, 140-144, Part 1(0):1 – 8, 1995.

[FMAE+07] J. Fabian, A. Matos-Abiague, C. Ertler, P. Stano, and I. Zutic. Semiconductor spintronics. *Acta Phys. Slov*, 57:565, 2007.

[FML+92] Eric E. Fullerton, J.E. Mattson, S.R. Lee, C.H. Sowers, Y.Y. Huang, G. Felcher, S.D. Bader, and F.T. Parker. Non-oscillatory antiferromagnetic coupling in sputtered fe/si superlattices. *Journal of Magnetism and Magnetic Materials*, 117(3):L301 – L306, 1992.

[FP07] J. Fernández-Rossier and J. J. Palacios. Magnetism in Graphene Nanoislands. *Physical Review Letters*, 99(17):177204, October 2007.

[FPBJ09] J. A. Fürst, T. G. Pedersen, M. Brandbyge, and A.-P. Jauho. Density functional study of graphene antidot lattices: Roles of geometrical relaxation and spin. *Phys. Rev. B*, 80(11):115117, September 2009.

[FVTB+02] J. Faure-Vincent, C. Tiusan, C. Bellouard, E. Popova, M. Hehn, F. Montaigne, and A. Schuhl. Interlayer magnetic coupling interactions of two ferromagnetic layers by spin polarized tunneling. *Phys. Rev. Lett.*, 89:107206, Aug 2002.

[GBB+01] R. R. Gareev, D. E. Bürgler, M. Buchmeier, D. Olligs, R. Schreiber, and P. Grünberg. Metallic-type oscillatory interlayer exchange coupling across an epitaxial fesi spacer. *Phys. Rev. Lett.*, 87:157202, Sep 2001.

[GBD+07] P. Grunberg, D.E. Burgler, H. Dassow, A.D. Rata, and C.M. Schneider. Spin-transfer phenomena in layered magnetic structures: Physical phenomena and materials aspects. *Acta Materialia*, 55(4):1171 – 1182, 2007.

[GDM+11] Isabella Gierz, Jan Hugo Dil, Fabian Meier, Bartosz Slomski, Juerg Osterwalder, Juergen Henk, Roland Winkler, Christian R. Ast, and Kern Klaus. Spin and angular resolved photoemission experiments on epitaxial graphene. *arXiv*, 1004:1573, 2011.

[Gei09] A K Geim. Graphene: Status and prospects. *Science*, 324:1530, 2009.

[Gev10] David Gevaus. graphene switched on. *Nature physics*, 6:1620, 2010.

[GJY+07] Li Gao, Xin Jiang, See-Hun Yang, J. D. Burton, Evgeny Y. Tsymbal, and Stuart S. P. Parkin. Bias voltage dependence of tunneling anisotropic magnetoresistance in magnetic tunnel junctions with mgo and al_2o_3 tunnel barriers. *Phys. Rev. Lett.*, 99:226602, Nov 2007.

[GKB+08] G. Giovannetti, P. A. Khomyakov, G. Brocks, V. M. Karpan, J. van den Brink, and P. J. Kelly. Doping graphene with metal contacts. *Phys. Rev. Lett.*, 101:026803, Jul 2008.

[GLW+06] Vickie W. Guo, Bin Lu, Xiaowei Wu, Ganping Ju, Bogdan Valcu, and Dieter Weller. A survey of anisotropy measurement techniques and study of thickness effect on interfacial and volume anisotropies in co/pt multilayer media. *Journal of Applied Physics*, 99(8):08E918, 2006.

[GN07] A. K. Geim and K. S. Novoselov. The rise of graphene. *Nature Materials*, 6:183–191, March 2007.

[GSP+86] P. Grünberg, R. Schreiber, Y. Pang, M. B. Brodsky, and H. Sowers. Layered magnetic structures: Evidence for antiferromagnetic coupling of fe layers across cr interlayers. *Phys. Rev. Lett.*, 57:2442–2445, Nov 1986.

[HB05] B. Heinrich and J. A. C. Bland, editors. *Ultrathin Magnetic Structures III*. Springer, 2005.

[HGB06] D. Huertas-Hernando, F. Guinea, and A. Brataas. Spin-orbit coupling in curved graphene, fullerenes, nanotubes, and nanotube caps. *Phys. Rev. B*, 74(15):155426, October 2006.

[HHDS07] E. H. Hwang, Ben Yu-Kuang Hu, and S. Das Sarma. notitle. *Phys. Rev. Lett.*, 99:226801, Nov 2007.

[HK64] P. Hohenberg and W. Kohn. Inhomogeneous electron gas. *Phys. Rev.*, 136:B864–B871, Nov 1964.

[HMP+12] Wei Han, K.M. McCreary, K. Pi, W.H. Wang, Yan Li, H. Wen, J.R. Chen, and R.K. Kawakami. Spin transport and relaxation in graphene. *Journal of Magnetism and Magnetic Materials*, 324(4):369 – 381, 2012.

[HPM+10] W. Han, K. Pi, K. M. McCreary, Y. Li, J. J. I. Wong, A. G. Swartz, and R. K. Kawakami. Tunneling Spin Injection into Single Layer Graphene. *Physical Review Letters*, 105(16):167202, October 2010.

[HVC+] E.M.J. Hassen, B. Viala, M.C. Cyrille, M. Cartier, O. Redon, B. Belhadji, H. X. Yang, J. P. Velev, M. Chshiev, and P. Lima. Room-temperature magnetoresistance in cofeb/srtio3/cofeb magnetic tunnel junctions deposited by ion beam sputtering. to be published.

[HWP+09] W. Han, W. H. Wang, K. Pi, K. M. McCreary, W. Bao, Y. Li, F. Miao, C. N. Lau, and R. K. Kawakami. Electron-Hole Asymmetry of Spin Injection and Transport in Single-Layer Graphene. *Physical Review Letters*, 102(13):137205, April 2009.

[HWSS02] H. C. Herper, P. Weinberger, L. Szunyogh, and C. Sommers. Interlayer exchange coupling and perpendicular electric transport in fe/si/fe trilayers. *Phys. Rev. B*, 66:064426, Aug 2002.

[HWV+01] H. C. Herper, P. Weinberger, A. Vernes, L. Szunyogh, and C. Sommers. Electric transport in fe/znse/fe heterostructures. *Phys. Rev. B*, 64:184442, Oct 2001.

[HZP10] H. Y. He, Y. Zhang, and B. C. Pan. Tuning electronic structure of graphene via tailoring structure: Theoretical study. *Journal of Applied Physics*, 107(11):114322, 2010.

[IE08] N. J. C. Ingle and I. S. Elfimov. Influence of epitaxial strain on the ferromagnetic semiconductor EuO: First-principles calculations. *Phys. Rev. B*, 77:121202, Mar 2008.

[IHL+07] S. Ikeda, J. Hayakawa, Young Min Lee, F. Matsukura, Y. Ohno, T. Hanyu, and H. Ohno. Magnetic tunnel junctions for spintronic memories and beyond. *Electron Devices, IEEE Transactions on*, 54(5):991 –1002, may 2007.

[IK07] Mikhail I. and Katsnelson. Graphene: carbon in two dimensions. *Materials Today*, 10(1-2):20 – 27, 2007.

[Ike08] S. Ikeda. Tunnel magnetoresistance of diffusion in cofeb/mgo/cofeb pseudo-spin-valves annealed at high temperature. *Applied Physics Letters*, 93:082508, 2008.

[IMY+10] S. Ikeda, K. Miura, H. Yamamoto, K. Mizunuma, H. D. Gan, M. Endo, S. Kanai, J. Hayakawa, F. Matsukura, and H. Ohno. A perpendicular-anisotropy cofebmgo magnetic tunnel junction. *Nat Mater*, 9:721, 2010.

[Jac98] J. D. Jackson. *Classical Electrodynamics*. Wiley, New York, 1998.

[JBdBdV96] M T Johnson, P J H Bloemen, F J A den Broeder, and J J de Vries. Magnetic anisotropy in metallic multilayers. *Reports on Progress in Physics*, 59(11):1409, 1996.

[JJKdB95] M.T. Johnson, R. Jungblut, P.J. Kelly, and F.J.A. den Broeder. Perpendicular magnetic anisotropy of multilayers: recent insights. *Journal of Magnetism and Magnetic Materials*, 148(1-2):118 – 124, 1995.

[JS95] J.C. and Slonczewski. Overview of interlayer exchange theory. *Journal of Magnetism and Magnetic Materials*, 150(1):13 – 24, 1995.

[Jul75] M. Julliere. Tunneling between ferromagnetic films. *Physics Letters A*, 54:225, 1975.

[Kas56] Tadao Kasuya. A theory of metallic ferro- and antiferromagnetism on zener's model. *Progress of Theoretical Physics*, 16(1):45–57, 1956.

[KCE+97] R. Kläsges, C. Carbone, W. Eberhardt, C. Pampuch, O. Rader, T. Kachel, and W. Gudat. Formation of a ferromagnetic silicide at the fe/si(100) interface. *Phys. Rev. B*, 56:10801–10804, Nov 1997.

[KCT+09] Alan Kalitsov, Mairbek Chshiev, Ioannis Theodonis, Nicholas Kioussis, and W. H. Butler. Spin-transfer torque in magnetic tunnel junctions. *Phys. Rev. B*, 79:174416, May 2009.

[KF96a] G. Kress and J. Furthmüller. Efficiency of ab-initio total energy calculations for metals and semiconductors using a plane-wave basis set. *Computational Materials Science*, 6(1):15 – 50, 1996.

[KF96b] G. Kresse and J. Furthmüller. Efficient iterative schemes for *ab initio* total-energy calculations using a plane-wave basis set. *Phys. Rev. B*, 54:11169–11186, Oct 1996.

[KFY+08] Hitoshi Kubota, Akio Fukushima, Kay Yakushiji, Taro Nagahama, Shinji Yuasa, Koji Ando, Hiroki Maehara, Yoshinori Nagamine, Koji Tsunekawa, David D. Djayaprawira, Naoki Watanabe, and Yoshishige Suzuki. Quantitative measurement of voltage dependence of spin-transfer torque in mgo-based magnetic tunnel junctions. *Nature Physics*, 4:37, 2008.

[KGK+07] V. M. Karpan, G. Giovannetti, P. A. Khomyakov, M. Talanana, A. A. Starikov, M. Zwierzycki, J. van den Brink, G. Brocks, and P. J. Kelly. Graphite and graphene as perfect spin filters. *Phys. Rev. Lett.*, 99:176602, Oct 2007.

[KH93] G. Kresse and J. Hafner. *Ab initio* molecular dynamics for liquid metals. *Phys. Rev. B*, 47:558–561, Jan 1993.

[KJ99] G. Kresse and D. Joubert. From ultrasoft pseudopotentials to the projector augmented-wave method. *Phys. Rev. B*, 59:1758–1775, Jan 1999.

[KS65] W. Kohn and L. J. Sham. Self-consistent equations including exchange and correlation effects. *Phys. Rev.*, 140:A1133–A1138, Nov 1965.

[KSO+08] Gukcheon Kim, Yuya Sakuraba, Mikihiko Oogane, Yasuo Ando, and Terunobu Miyazaki. Tunneling magnetoresistance of magnetic tunnel junctions using perpendicular magnetization l1[sub 0]-copt electrodes. *Applied Physics Letters*, 92(17):172502, 2008.

[KYA92] Kentaro Kyuno, Ryoichi Yamamoto, and Setsuro Asano. Theoretical study on the magnetocrystalline anisotropy of x/co (x=pd, pt, cu, ag, au) multilayers. *Journal of the Physical Society of Japan*, 61(6):2099–2103, 1992.

[KYV+06] T. Katayama, S. Yuasa, J. Velve, M. Ye. Zhuravlev, S. S. Jaswal, and E. Y. Tsymbal. Interlayer exchange coupling in fe/mgo/fe magnetic tunnel junctions. *Applied Physics Letters*, 89(11):112503, 2006.

[LFM+04] P. O. Lehtinen, A. S. Foster, Y. Ma, A. V. Krasheninnikov, and R. M. Nieminen. Irradiation-Induced Magnetism in Graphite: A Density Functional Study. *Physical Review Letters*, 93(18):187202, October 2004.

[LHA+07] D. Lacour, M. Hehn, M. Alnot, F. Montaigne, F. Greullet, G. Lengaigne, O. Lenoble, S. Robert, and A. Schuhl. Magnetic properties of postoxidized pt/co/al layers with perpendicular anisotropy. *Applied Physics Letters*, 90(19):192506, 2007.

[LHHW11] Wen-Chin Lin, Ya-Yun Huang, Tsung-Ying Ho, and Chih-Hsiung Wang. Stable canted magnetization in co thin films on highly oriented pyrolytic graphite induced by template defects. *Applied Physics Letters*, 99(17):172502, 2011.

[LHI+07] Y. M. Lee, J. Hayakawa, S. Ikeda, F. Matsukura, and H. Ohno. Effect of electrode composition on the tunnel magnetoresistance of pseudo-spin-valve magnetic tunnel junction with a mgo tunnel barrier. *Applied Physics Letters*, 90(21):212507, 2007.

[Lie89] E. H. Lieb. Two theorems on the Hubbard model. *Physical Review Letters*, 62:1201–1204, March 1989.

[LKL05] Dongwon Lim, Sungdong Kim, and Seong-Rae Lee. Magnetoresistance behavior of a magnetic tunnel junction with perpendicularly magnetized co/pd multilayers. *Journal of Applied Physics*, 97(10):10C902, 2005.

[LLG+96] Yu Lu, X. W. Li, G. Q. Gong, Gang Xiao, A. Gupta, P. Lecoeur, J. Z. Sun, Y. Y. Wang, and V. P. Dravid. Large magnetotunneling effect at low magnetic fields in micrometer-scale epitaxial $la_{0.67}sr_{0.33}mno_3$ tunnel junctions. *Phys. Rev. B*, 54:R8357–R8360, Sep 1996.

[LSK+00] P. LeClair, H. J. M. Swagten, J. T. Kohlhepp, R. J. M. van de Veerdonk, and W. J. M. de Jonge. Apparent spin polarization decay in cu-dusted coa2o3co tunnel junctions. *Phys. Rev. Lett.*, 84:2933–2936, Mar 2000.

[LSKdJ00] P. LeClair, H. J. M. Swagten, J. T. Kohlhepp, and W. J. M. de Jonge. Tunnel conductance as a probe of spin polarization decay in cu dusted co/al2o3/co tunnel junctions. *Applied Physics Letters*, 76(25):3783–3785, 2000.

[MAF09] A. Matos-Abiague and J. Fabian. Anisotropic tunneling magnetoresistance and tunneling anisotropic magnetoresistance: Spin-orbit coupling in magnetic tunnel junctions. *Phys. Rev. B*, 79:155303, Apr 2009.

[Mar04] Richard M Martin. *Electronic Structure*. Cambridge University, 2004.

[MCK+86] C. F. Majkrzak, J. W. Cable, J. Kwo, M. Hong, D. B. McWhan, Y. Yafet, J. V. Waszczak, and C. Vettier. Observation of a magnetic antiphase domain structure with long-range order in a synthetic gd-y superlattice. *Phys. Rev. Lett.*, 56:2700–2703, Jun 1986.

[MDL+08] A. Manchon, C. Ducruet, L. Lombard, S. Auffret, B. Rodmacq, B. Dieny, S. Pizzini, J. Vogel, V. Uhlíř, M. Hochstrasser, and G. Panaccione. Analysis of oxygen induced anisotropy crossover in pt/co/mox trilayers. *Journal of Applied Physics*, 104(4):043914, 2008.

[MFP09] F. Muñoz-Rojas, J. Fernández-Rossier, and J. J. Palacios. Giant Magnetoresistance in Ultrasmall Graphene Based Devices. *Physical Review Letters*, 102(13):136810, April 2009.

[MG86] A Mauger and C Godart. The magnetic, optical, and transport properties of representatives of a class of magnetic semiconductors: The europium chalcogenides. *Physics Reports*, 141(23):51 – 176, 1986.

[MIP+09] K. Mizunuma, S. Ikeda, J. H. Park, H. Yamamoto, H. Gan, K. Miura, H. Hasegawa, J. Hayakawa, F. Matsukura, and H. Ohno. Mgo barrier-perpendicular magnetic tunnel junctions with cofe/pd multilayers and ferromagnetic insertion layers. *Applied Physics Letters*, 95(23):232516, 2009.

[MKWM95] J. S. Moodera, Lisa R. Kinder, Terrilyn M. Wong, and R. Meservey. Large magnetoresistance at room temperature in ferromagnetic thin film tunnel junctions. *Phys. Rev. Lett.*, 74:3273–3276, Apr 1995.

[MMJP+10] D. Martínez-Martín, M. Jaafar, R. Pérez, J. Gómez-Herrero, and A. Asenjo. Upper Bound for the Magnetic Force Gradient in Graphite. *Physical Review Letters*, 105(25):257203, December 2010.

[Mot36] N F Mott. *The electrical conductivity of transition metals. Proceedings of the Royal Society of London. Series A, Mathematical and Physical Sciences*. Royal Society of London, 1936.

[MP76] Hendrik J. Monkhorst and James D. Pack. Special points for brillouin-zone integrations. *Phys. Rev. B*, 13:5188–5192, Jun 1976.

[MP89] M. Methfessel and A. T. Paxton. High-precision sampling for Brillouin-zone integration in metals. *Phys. Rev. B*, 40:3616–3621, August 1989.

[MPK+01] H. L. Meyerheim, R. Popescu, J. Kirschner, N. Jedrecy, M. Sauvage-Simkin, B. Heinrich, and R. Pinchaux. Geometrical and compositional structure at metal-oxide interfaces: Mgo on fe(001). *Phys. Rev. Lett.*, 87:076102, Jul 2001.

[MPV+08] A. Manchon, S. Pizzini, J. Vogel, V. Uhlir, L. Lombard, C. Ducruet, S. Auffret, B. Rodmacq, B. Dieny, M. Hochstrasser, and G. Panaccione. X-ray analysis of oxygen-induced perpendicular magnetic anisotropy in trilayers. *Journal of Magnetism and Magnetic Materials*, 320(13):1889 – 1892, 2008.

[MRA+02] S. Monso, B. Rodmacq, S. Auffret, G. Casali, F. Fettar, B. Gilles, B. Dieny, and P. Boyer. Crossover from in-plane to perpendicular anisotropy in pt/cofe/alo sandwiches as a function of al oxidation: A very accurate control of the oxidation of tunnel barriers. *Applied Physics Letters*, 80(22):4157–4159, 2002.

[MT95] T. Miyazaki and N. Tezuka. Tmr in al_2o_3. *J. Magn. Magn. Mater.*, 139:231, 1995.

[MU01] J. Mathon and A. Umerski. Theory of tunneling magnetoresistance of an epitaxial fe/mgo/fe(001) junction. *Phys. Rev. B*, 63:220403, May 2001.

[MZBW99] J. M. MacLaren, X.-G. Zhang, W. H. Butler, and Xindong Wang. Layer kkr approach to bloch-wave transmission and reflection: Application to spin-dependent tunneling. *Phys. Rev. B*, 59:5470–5478, Feb 1999.

[NAI+10] Kohji Nakamura, Toru Akiyama, Tomonori Ito, M. Weinert, and A. J. Freeman. Role of an interfacial feo layer in the electric-field-driven switching of magnetocrystalline anisotropy at the fe/mgo interface. *Phys. Rev. B*, 81:220409, Jun 2010.

[NDJT10] Manish K. Niranjan, Chun-Gang Duan, Sitaram S. Jaswal, and Evgeny Y. Tsymbal. Electric field effect on magnetization at the fe/mgo(001) interface. *Applied Physics Letters*, 96(22):222504, 2010.

[NGM+04] K. S. Novoselov, A. K. Geim, S. V. Morozov, D. Jiang, Y. Zhang, S. V. Dubonos, I. V. Grigorieva, and A. A. Firsov. Electric field effect in atomically thin carbon films. *Science*, 306(5696):666–669, 2004.

[NGM+05] K. S. Novoselov, A. K. Geim, S. V. Morozov, D. Jiang, M. I. Katsnelson, I. V. Grigorieva, S. V. Dubonos, and A. A. Firsov. Two-dimensional gas of massless dirac fermions in graphene. *Nature*, 438:197, 2005.

[NKS+98] N. Nakajima, T. Koide, T. Shidara, H. Miyauchi, H. Fukutani, A. Fujimori, K. Iio, T. Katayama, M. Nývlt, and Y. Suzuki. Perpendicular magnetic anisotropy caused by interfacial hybridization via enhanced orbital moment in Co/Pt multilayers: Magnetic circular x-ray dichroism study. *Phys. Rev. Lett.*, 81:5229–5232, Dec 1998.

[NRAD09] L. E. Nistor, B. Rodmacq, S. Auffret, and B. Dieny. Pt/co/oxide and oxide/co/pt electrodes for perpendicular magnetic tunnel junctions. *Applied Physics Letters*, 94(1):012512, 2009.

[NRD+10] L.E. Nistor, B. Rodmacq, C. Ducruet, C. Portemont, I.L. Prejbeanu, and B. Dieny. Correlation between perpendicular anisotropy and magnetoresistance in magnetic tunnel junctions. *Magnetics, IEEE Transactions on*, 46(6):1412 –1415, june 2010.

[OC09] Kaan Oguz and J.M.D. Coey. Room-temperature magnetoresistance in cofeb/sto/cofeb magnetic tunnel junctions. *Journal of Magnetism and Magnetic Materials*, 321(8):1009 – 1011, 2009.

[OEA+10] H. Ohldag, P. Esquinazi, E. Arenholz, D. Spemann, M. Rothermel, A. Setzer, and T. Butz. The role of hydrogen in room-temperature ferromagnetism at graphite surfaces. *New Journal of Physics*, 12(12):123012, December 2010.

[Ohn98] H Ohno. Making nonmagnetic semiconductors ferromagnetic. *Science,*, 281:951–956, 1998.

[ON97] Chuhei Oshima and Ayato Nagashima. Ultra-thin epitaxial films of graphite and hexagonal boron nitride on solid surfaces. *Journal of Physics: Condensed Matter*, 9(1):1, 1997.

[PBE96] J. P. Perdew, K. Burke, and M. Ernzerhof. Generalized gradient approximation made simple. *Physical Review Letters*, 77:3865–3868, 1996.

[PFB08] J. J. Palacios, J. Fernández-Rossier, and L. Brey. Vacancy-induced magnetism in graphene and graphene ribbons. *Phys. Rev. B*, 77(19):195428, May 2008.

[PFP+08] T. G. Pedersen, C. Flindt, J. Pedersen, N. A. Mortensen, A.-P. Jauho, and K. Pedersen. Graphene Antidot Lattices: Designed Defects and Spin Qubits. *Physical Review Letters*, 100(13):136804, April 2008.

[PKP+04] Stuart S. P. Parkin, Christian Kaiser, Alex Panchula, Philip M. Rice, Brian Hughes, Mahesh Samant, and See-Hun Yang. Giant tunnelling magnetoresistance at room temperature with mgo (100) tunnel barriers. *Nat Mater*, 3:862, 2004.

[PPJ+08] Jeong-Heon Park, Chando Park, Taehee Jeong, Matthew T. Moneck, Noel T. Nufer, and Jian-Gang Zhu. Co/pt multilayer based magnetic tunnel junctions using perpendicular magnetic anisotropy. *Journal of Applied Physics*, 103(7):07A917, 2008.

[PRS+99] S. S. P. Parkin, K. P. Roche, M. G. Samant, P. M. Rice, R. B. Beyers, R. E. Scheuerlein, E. J. O'Sullivan, S. L. Brown, J. Bucchigano, D. W. Abraham, Yu Lu, M. Rooks, P. L. Trouilloud, R. A. Wanner, and W. J. Gallagher. Exchange-biased magnetic tunnel junctions and application to nonvolatile magnetic random access memory (invited). *Journal of Applied Physics*, 85(8):5828–5833, 1999.

[PWW+08] B. G. Park, J. Wunderlich, D. A. Williams, S. J. Joo, K. Y. Jung, K. H. Shin, K. Olejnik, A. B. Shick, and T. Jungwirth. Tunneling anisotropic magnetoresistance in multilayer-copt. *Phys. Rev. Lett.*, 100:087204, Feb 2008.

[RAD+03] B. Rodmacq, S. Auffret, B. Dieny, S. Monso, and P. Boyer. Crossovers from in-plane to perpendicular anisotropy in magnetic tunnel junctions as a function of the barrier degree of oxidation. *Journal of Applied Physics*, 93(10):7513–7515, 2003.

[RK54] M. A. Ruderman and C. Kittel. Indirect exchange coupling of nuclear magnetic moments by conduction electrons. *Phys. Rev.*, 96:99–102, Oct 1954.

[RMD+09a] B. Rodmacq, A. Manchon, C. Ducruet, S. Auffret, and B. Dieny. Influence of thermal annealing on the perpendicular magnetic anisotropy of pt/co/alox trilayers. *Phys. Rev. B*, 79:024423, Jan 2009.

[RMD+09b] B. Rodmacq, A. Manchon, C. Ducruet, S. Auffret, and B. Dieny. Influence of thermal annealing on the perpendicular magnetic anisotropy of pt/co/alox trilayers. *Phys. Rev. B*, 79:024423, Jan 2009.

[RVSB+09] O. Rader, A. Varykhalov, J. Sánchez-Barriga, D. Marchenko, A. Rybkin, and A. M. Shikin. Is there a rashba effect in graphene on 3d ferromagnets. *Phys. Rev. Lett.*, 102:057602, Feb 2009.

[SCL06a] Y.-W. Son, M. L. Cohen, and S. G. Louie. Energy Gaps in Graphene Nanoribbons. *Physical Review Letters*, 97(21):216803, November 2006.

[SCL06b] Y.-W. Son, M. L. Cohen, and S. G. Louie. Half metallic graphene nanoribbons. *nature*, 444:347–349, November 2006.

[SCS+08] J. C. Sankey, Y.-T. Cui, J. Z. Sun, J. C. Slonczewski, R. A. Buhrman, and D. C. Ralph. Measurement of the spin-transfer-torque vector in magnetic tunnel junctions. *Nature Physics*, 4:67, 2008.

[Slo89] J. C. Slonczewski. Conductance and exchange coupling of two ferromagnets separated by a tunneling barrier. *Phys. Rev. B*, 39:6995–7002, Apr 1989.

[Slo93] J. C. Slonczewski. Mechanism of interlayer exchange in magnetic multilayers. *Journal of Magnetism and Magnetic Materials*, 126:374 – 379, 1993.

[Slo95] J. C. Slonczewski. Overview of interlayer exchange theory. *Journal of Magnetism and magnetic materials*, 150:13, 1995.

[SMK07] M. Shishkin, M. Marsman, and G. Kresse. Accurate quasiparticle spectra from self-consistent *GW* calculations with vertex corrections. *Phys. Rev. Lett.*, 99:246403, Dec 2007.

[SMN+09] Yoichi Shiota, Takuto Maruyama, Takayuki Nozaki, Teruya Shinjo, Masashi Shiraishi, and Yoshishige Suzuki. Voltage-assisted magnetization switching in ultrathin fe80co20 alloy layers. *Applied Physics Express*, 2(6):063001, 2009.

[SNR+10] M. Sepioni, R. R. Nair, S. Rablen, J. Narayanan, F. Tuna, R. Winpenny, A. K. Geim, and I. V. Grigorieva. Limits on Intrinsic Magnetism in Graphene. *Physical Review Letters*, 105(20):207205, November 2010.

[SNT+12] T. Shimizu, J. Nakamura, K. Tada, Y. Yagi, and J. Haruyama. Magnetoresistance oscillations arising from edge-localized electrons in low-defect graphene antidot-lattices. *Applied Physics Letters*, 100(2):023104, 2012.

[SSR+86] M. B. Salamon, Shantanu Sinha, J. J. Rhyne, J. E. Cunningham, Ross W. Erwin, Julie Borchers, and C. P. Flynn. Long-range incommensurate magnetic order in a dy-y multilayer. *Phys. Rev. Lett.*, 56:259–262, Jan 1986.

[Sti93] M. D. Stiles. Exchange coupling in magnetic heterostructures. *Phys. Rev. B*, 48:7238–7258, Sep 1993.

[Sti99] M. D. Stiles. Interlayer exchange coupling. *Journal of Magnetism and Magnetic Materials*, 200(1-3):322 – 337, 1999.

[SW74] J. Schoenes and P. Wachter. Exchange optics in gd-doped euo. *Phys. Rev. B*, 9:3097–3105, Apr 1974.

[SWN99] Manish Sharma, Shan X. Wang, and Janice H. Nickel. Inversion of spin polarization and tunneling magnetoresistance in spin-dependent tunneling junctions. *Phys. Rev. Lett.*, 82:616–619, Jan 1999.

[SYZ+11] Zhiwen Shi, Rong Yang, Lianchang Zhang, Yi Wang, Donghua Liu, Dongxia Shi, Enge Wang, and Guangyu Zhang. Patterning graphene with zigzag edges by self-aligned anisotropic etching. *Advanced Materials*, 23(27):3061–3065, 2011.

[TBHL92] S. Toscano, B. Briner, H. Hopster, and M. Landolt. Exchange-coupling between ferromagnets through a non-metallic amorphous spacer-layer. *Journal of Magnetism and Magnetic Materials*, 114(1-2):L6 – L10, 1992.

[TCD+99] S. Tehrani, E. Chen, M. Durlam, M. DeHerrera, J. M. Slaughter, J. Shi, and G. Kerszykowski. High density submicron magnetoresistive random access memory (invited). *Journal of Applied Physics*, 85(8):5822–5827, 1999.

[TJP+07a] Nikolaos Tombros, Csaba Jozsa, Mihaita Popinciuc, Harry T. Jonkman, and Bart J. van Wees. Electronic spin transport and spin precession in single graphene layers at room temperature. *Nature*, 448:571, 2007.

[TJP+07b] Nikolaos Tombros, Csaba Jozsa, Mihaita Popinciuc, Harry T. Jonkman, and Bart J. van Wees. Electronic spin transport and spin precession in single graphene layers at room temperature. *Nature*, 448:571, 2007.

[TKK+06] Ioannis Theodonis, Nicholas Kioussis, Alan Kalitsov, Mairbek Chshiev, and W. H. Butler. Anomalous bias dependence of spin torque in magnetic tunnel junctions. *Phys. Rev. Lett.*, 97:237205, Dec 2006.

[TML03] Evgeny Y Tsymbal, Oleg N Mryasov, and Patrick R LeClair. Spin-dependent tunnelling in magnetic tunnel junctions. *Journal of Physics: Condensed Matter*, 15(4):R109, 2003.

[TP98] E. Yu. Tsymbal and D. G. Pettifor. Spin-polarized electron tunneling across a disordered insulator. *Phys. Rev. B*, 58:432–437, Jul 1998.

[TP99] E. Yu. Tsymbal and D. G. Pettifor. The influence of impurities within the barrier on tunneling magnetoresistance. *Journal of Applied Physics*, 85(8):5801–5803, 1999.

[UBGG10] M. M. Ugeda, I. Brihuega, F. Guinea, and J. M. Gómez-Rodríguez. Missing Atom as a Source of Carbon Magnetism. *Physical Review Letters*, 104(9):096804, March 2010.

[VBBD01] A. Vedyayev, D. Bagrets, A. Bagrets, and B. Dieny. Resonant spin-dependent tunneling in spin-valve junctions in the presence of paramagnetic impurities. *Phys. Rev. B*, 63:064429, Jan 2001.

[VBS+05] J. P. Velev, K. D. Belashchenko, D. A. Stewart, M. van Schilfgaarde, S. S. Jaswal, and E. Y. Tsymbal. Negative spin polarization and large tunneling magnetoresistance in epitaxial Co|srtio$_3$|Co magnetic tunnel junctions. *Phys. Rev. Lett.*, 95:216601, Nov 2005.

[VCB06] S. Vutukuri, M. Chshiev, and W. H. Butler. Spin-dependent tunneling in fm—semiconductor—fm structures. *Journal of Applied Physics*, 99(8):08K302, 2006.

[VRS+10] A. Vedyaev, N. Ryzhanova, N. Strelkov, M. Chshiev, and B. Dieny. A two-band model of spin-polarized transport in fe/cr/mgo/fe magnetic tunnel junctions. *Journal of Applied Physics*, 107(9):09C720, 2010.

[VSBS+08] A. Varykhalov, J. Sánchez-Barriga, A. M. Shikin, C. Biswas, E. Vescovo, A. Rybkin, D. Marchenko, and O. Rader. Electronic and magnetic properties of quasifreestanding graphene on ni. *Phys. Rev. Lett.*, 101:157601, Oct 2008.

[VVKBY+10] Chi Vo-Van, Zoukaa Kassir-Bodon, Hongxin Yang, Johann Coraux, Jan Vogel, Stefania Pizzini, Pascale Bayle-Guillemaud, Mairbek Chshiev, Laurent Ranno, ValÃ©rie Guisset, Philippe David, Violaine Salvador, and Olivier Fruchart. Ultrathin epitaxial cobalt films on graphene for spintronic investigations and applications. *New Journal of Physics*, 12(10):103040, 2010.

[VVSC+11] Chi Vo-Van, Stefan Schumacher, Johann Coraux, Violetta Sessi, Olivier Fruchart, Nick B. Brookes, Philippe Ohresser, and Thomas Michely. Magnetism of cobalt nanoclusters on graphene on iridium. *Applied Physics Letters*, 99(14):142504, 2011.

[WAB+01] S. A. Wolf, D. D. Awschalom, R. A. Buhrman, J. M. Daughton, S. von Molnar, M. L. Roukes, A. Y. Chtchelkanova, and D. M. Treger. Spintronics: A spin-based electronics vision for the future. *Science*, 294:1488–1495, November 2001.

[WAB+08] M. Wimmer, I. Adagideli, S. Berber, D. Tománek, and K. Richter. Spin currents in rough graphene nanoribbons: Universal fluctuations and spin injection. *Physical Review Letters*, 100(17):177207, May 2008.

[Wal47] P. R. Wallace. The band theory of graphite. *Phys. Rev.*, 71:622–634, May 1947.

[WAMS08] Han-Chun Wu, S. K. Arora, O. N. Mryasov, and I. V. Shvets. Antiferromagnetic interlayer exchange coupling between fe3o4 layers across a nonmagnetic mgo dielectric layer. *Applied Physics Letters*, 92(18):182502, 2008.

[WG05] S. Wang and M. Grifoni. Helicity and Electron-Correlation Effects on Transport Properties of Double-Walled Carbon Nanotubes. *Physical Review Letters*, 95(26):266802, December 2005.

[WMZ+02] O. Wunnicke, Ph. Mavropoulos, R. Zeller, P. H. Dederichs, and D. Grundler. Ballistic spin injection from fe(001) into znse and gaas. *Phys. Rev. B*, 65:241306, May 2002.

[WP91] Yue Wang and John P. Perdew. Correlation hole of the spin-polarized electron gas, with exact small-wave-vector and high-density scaling. *Phys. Rev. B*, 44:13298–13307, Dec 1991.

[WRH+10] M. Weser, Y. Rehder, K. Horn, M. Sicot, M. Fonin, A. B. Preobrajenski, E. N. Voloshina, E. Goering, and Yu. S. Dedkov. Induced magnetism of carbon atoms at the graphene/ni(111) interface. *Applied Physics Letters*, 96(1):012504, 2010.

[WWF93] Ding-sheng Wang, Ruqian Wu, and A. J. Freeman. Magnetocrystalline anisotropy of co-pd interfaces. *Phys. Rev. B*, 48:15886–15892, Dec 1993.

[WWS+94] D. Weller, Y. Wu, J. Stöhr, M. G. Samant, B. D. Hermsmeier, and C. Chappert. Orbital magnetic moments of co in multilayers with perpendicular magnetic anisotropy. *Phys. Rev. B*, 49:12888–12896, May 1994.

[WYMK09] Wei L. Wang, Oleg V. Yazyev, Sheng Meng, and Efthimios Kaxiras. Topological frustration in graphene nanoflakes: Magnetic order and spin logic devices. *Phys. Rev. Lett.*, 102:157201, Apr 2009.

[Yaf94] Y. Yafet, editor. *Magnetic Multilayers*. World Scientific, Singapore, 1994.

[Yaz08] O. V. Yazyev. Magnetism in Disordered Graphene and Irradiated Graphite. *Physical Review Letters*, 101(3):037203, July 2008.

[Yaz10] O. V. Yazyev. Emergence of magnetism in graphene materials and nanostructures. *Reports on Progress in Physics*, 73(5):056501, May 2010.

[YBV+11] T.-Y. Yang, J. Balakrishnan, F. Volmer, A. Avsar, M. Jaiswal, J. Samm, S. R. Ali, A. Pachoud, M. Zeng, M. Popinciuc, G. Guntherodt, B. Beschoten, and B. ozyilmaz. Observation of Long Spin-Relaxation Times in Bilayer Graphene at Room Temperature. *Physical Review Letters*, 107(4):047206, July 2011.

[YCB+11] Hong-Xin Yang, Mairbek Chshiev, Danil W. Boukhvalov, Xavier Waintal, and Stephan Roche. Inducing and optimizing magnetism in graphene nanomeshes. *Phys. Rev. B*, 84:214404, Dec 2011.

[YCD+11] H. X. Yang, M. Chshiev, B. Dieny, J. H. Lee, A. Manchon, and K. H. Shin. First-principles investigation of the very large perpendicular magnetic anisotropy at fe|mgo and co|mgo interfaces. *Phys. Rev. B*, 84:054401, Aug 2011.

[YCK+10] H. X. Yang, M. Chshiev, A. Kalitsov, A. Schuhl, and W. H. Butler. Effect of structural relaxation and oxidation conditions on interlayer exchange coupling in femgofe tunnel junctions. *Applied Physics Letters*, 96(26):262509, 2010.

[YH07] O. V. Yazyev and L. Helm. Defect-induced magnetism in graphene. *Phys. Rev. B*, 75(12):125408, March 2007.

[YK08] O. V. Yazyev and M. I. Katsnelson. Magnetic correlations at graphene edges: Basis for novel spintronics devices. *Physical Review Letters*, 100(4):047209, February 2008.

[YKI+11] M. Yamanouchi, R. Koizumi, S. Ikeda, H. Sato, K. Mizunuma, K. Miura, H. D. Gan, F. Matsukura, and H. Ohno. Dependence of magnetic anisotropy on mgo thickness and buffer layer in co[sub 20]fe[sub 60]b[sub 20]-mgo structure. *Journal of Applied Physics*, 109(7):07C712, 2011.

[YKS+09] S Yakata, H Kubota, Y Suzuki, K Yakushiji, A Fukushima, S Yuasa, and K Ando. Influence of perpendicular magnetic anisotropy on spin-transfer switching current in cofeb/mgo/cofeb magnetic tunnel junctions. *Journal of Applied Physics*, 105(7):07D131, 2009.

[YNF+04] Shinji Yuasa, Taro Nagahama, Akio Fukushima, Yoshishige Suzuki, and Koji Ando. Giant room-temperature magnetoresistance in single-crystal fe/mgo/fe magnetic tunnel junctions. *Nat Mater*, 3:868, 2004.

[Yos57] Kei Yosida. Magnetic properties of cu-mn alloys. *Phys. Rev.*, 106:893–898, Jun 1957.

[YP09] Oleg V. Yazyev and Alfredo Pasquarello. Magnetoresistive junctions based on epitaxial graphene and hexagonal boron nitride. *Phys. Rev. B*, 80:035408, Jul 2009.

[YPS+07] L. Yang, C.-H. Park, Y.-W. Son, M. L. Cohen, and S. G. Louie. Quasiparticle energies and band gaps in graphene nanoribbons. *Physical Review Letters*, 99(18):186801, November 2007.

[YWMK08] Oleg V. Yazyev, Wei L. Wang, Sheng Meng, and Efthimios Kaxiras. Comment on graphene nanoflakes with large spin: Broken-symmetry states. *Nano Letters*, 8(2):766–766, 2008. PMID: 18205428.

[YYQ+07] Y. Yao, F. Ye, X.-L. Qi, S.-C. Zhang, and Z. Fang. Spin-orbit gap of graphene: First-principles calculations. *Phys. Rev. B*, 75(4):041401, January 2007.

[ZBB03] X.-G. Zhang, W. H. Butler, and Amrit Bandyopadhyay. Effects of the iron-oxide layer in fe-feo-mgo-fe tunneling junctions. *Phys. Rev. B*, 68:092402, Sep 2003.

[ZFDS04] Igor Zutic, Jaroslav Fabian, and S. Das Sarma. Spintronics: Fundamentals and applications. *Rev. Mod. Phys.*, 76:323–410, Apr 2004.

[ZLB+12] Hongbin Zhang, Cesar Lazo, Stefan Blügel, Stefan Heinze, and Yuriy Mokrousov. Electrically tunable quantum anomalous hall effect in graphene decorated by 5*d* transition-metal adatoms. *Phys. Rev. Lett.*, 108:056802, Feb 2012.

[ZTSK05] Y. Zhang, Y.-W. Tan, H. L. Stormer, and P. Kim. Experimental observation of the quantum hall effect and berry's phase in graphene. *Nature(London)*, 438:201–204, November 2005.

[ZTV05] M. Ye. Zhuravlev, E. Y. Tsymbal, and A. V. Vedyayev. Impurity-assisted interlayer exchange coupling across a tunnel barrier. *Phys. Rev. Lett.*, 94:026806, Jan 2005.

[ZVVT06] M. Ye. Zhuravlev, J. Velve, A.V. Vedyayev, and E.Y. Tsymbal. Effect of oxygen vacancies on interlayer exchange coupling in femgofe tunnel junctions. *Journal of Magnetism and Magnetic Materials*, 300(1):e277 – e280, 2006.

[ZZZ+09] X. H. Zheng, G. R. Zhang, Z. Zeng, V. M. Garcia-Suarez, and C. J. Lambert. Effects of antidots on the transport properties of graphene nanoribbons. *Phys. Rev. B*, 80(7):075413, August 2009.

Publication List

Hongxin Yang (杨洪新)

1. Giant Spin Hall Effect Induced by Skew Scattering from Bismuth Impurities inside Thin Film CuBi Alloys
   Y. Niimi, Y. Kawanishi, D. H. Wei, C. Derahlot, H. X. Yang, M. Chshiev, T. Valet, A. Fert, and Y. Otani
   Phys. Rev. Lett. 109, 156602 (2012)

2. Air-Protected Epitaxial Graphene/Ferromagnet Hybrids Prepared by Facile Intercalation
   J. Coraux,A. N'Diaye, N. Rougemaille, C. Vo-Van, A. Kimouche, H.-X. Yang, M. Chshiev, N. Bendiab, O. Fruchar, A. Schmid
   J. Phys. Chem. Lett. 3, 2059 (2012)

3. Room temperature magnetoresistance in CoFeB/$SrTiO_3$/CoFeB magnetic tunnel junctions deposited by ion beam sputtering
   E. M. J. Hassen, B. Viala, M. C. Cyrille, M. Cartier, O. Redon, P. Lima, B. Belhadji, H. X. Yang, J. Velev, and M. Chshiev
   J. Appl. Phys. 111, 07C727 (2012)

4. Inducing and optimizing magnetism in graphene nanomeshes
   H.-X. Yang, M. Chshiev, D. W. Boukhvalov, X. Waintal, and S. Roche
   Phys. Rev. B 84, 214404 (2011)

5. First-principles investigation of the very large perpendicular magnetic anisotropy at Fe|MgO and Co|MgO interfaces
   H. X. Yang, J. H. Lee, M. Chshiev, A. Manchon, K. H. Shin, and B. Dieny
   Phys. Rev. B 84, 054401 (2011)

6. Effect of structural relaxation and oxidation conditions on interlayer exchange coupling in Fe|MgO|Fe tunnel junctions
   H. X. Yang, M. Chshiev, A. Kalitsov, A. Schuhl, and W. H. Butler
   Appl. Phys. Lett. 96, 262509 (2010)

7. Ultrathin epitaxial cobalt films on graphene for spintronic investigations and applications
   C. Vo-Van, Z. Kassir-Bodon, H. X. Yang, J. Coraux, J. Vogel, S. Pizzini, P. Bayle-Guillemaud, M. Chshiev, L. Ranno, V. Santonacci, P. David, V. Salvador and O. Fruchart
   New J. Phys. 12, 103040 (2010)

8. The metallicity of B-doped diamond surface by first-principles study
   C. Lu, Z. L. Wang, L. F. Xu, H. X. Yang, J. J. Li, and C. Z. Gu
   Diam. Relat. Mater. 19, 824-828 (2010)

9. Stable hydroxyl network on diamond (0 0 1) via first-principles and MD investigation
   H. X. Yang, L. F. Xu, C. Z. Gu, Z. Fang, S. B. Zhang, and M. Chshiev
   Surf. Sci. 603, 3035-3040 (2009)

Preprint:

10. Spin-orbit coupling effect by minority interface resonance states in single-crystal magnetic tunnel junctions
    Y. Lu, H. X. Yang, C. Tiusan, M. Hehn, M. Chshiev, C. Bellouard, B. Kierren, G. Lengaigne, A. Duluard, D. Lacour, and F. Montaigne
    Phys. Rev. B under review (2012)

11. Magnetic insulators-induced proximity effects in graphene: spin filtering and exchange splitting gaps
    H. X. Yang, A. Hallal, D. Terrade, X. Wainatl, S. Roche, and M. Chshiev
    Phys. Rev. Lett. under review (2012)

12. First-principles justification of correlation between perpendicular magnetic anisotropy and Bloch states spin filtering in MgO-based tunnel junctions
    H. X. Yang, M. Chshiev, and B. Dieny
    To be submitted

13. Interlayer exchange coupling in FM|$SrTiO_3$|FM tunnel junctions
    H. X. Yang, B. Belhadji, J. Velev, and M. Chshiev
    In prep.

Conference Activities

1. **Ab-initio justification of correlation between perpendicular magnetic anisotropy and Bloch states spin filtering in MgO-based tunnel junctions** (Talk)
   H. X. Yang (presenter), M. Chshiev, and B. Dieny
   56^{th} Annual Conference on Magnetism & Magnetic Materials October 30–November 3, 2011 Scottsdale, Arizona, USA, CC-05

2. **Inducing Magnetism in Graphene Nanomesh** (Talk)
   Hongxin Yang (presenter), Mair Chshiev, Danil W. Boukhvalov, Xavier Waintal, Stephan Roche

56th Annual Conference on Magnetism & Magnetic Materials October 30–November 3, 2011 Scottsdale, Arizona, USA, BE-12

3. **First-principles study of Interlayer Exchange Coupling in Co|SrTiO3|Co Magnetic Tunnel Junctions** (Poster)
   H. X. Yang, B. Belhadji (presenter), J. Velev and M. Chshiev
   56th Annual Conference on Magnetism & Magnetic Materials October 30–November 3, 2011 Scottsdale, Arizona, USA, FP-11

4. **Mechanisms of Perpendicular Magnetic Anisotropy at Co(Fe)|MgO interfaces** (Invited talk)
   H. Yang, J. H. Lee, M. Chshiev (presenter), A. Manchon, K.-H. Shin, and B. Dieny
   Moscow International Symposium on Magnetism, Aug. 21-25, 2011, Moscow, Russia, 23RP-A-3

5. **Nature of perpendicular magnetic anisotropy at Fe|MgO and Co|MgO interfaces from first-principles** (Poster)
   H. Yang (presenter), J. H. Lee, M. Chshiev, A. Manchon, K.-H. Shin, and B. Dieny
   2011 INTERMAG Conference, April 25-29, Taipei, China, FQ-11

6. **Shape induced Magnetic Moment in Graphene Nanomesh** (Talk)
   H. X. Yang, M. Chshiev (presenter), X. Waintal, S. Roche
   Graphene Week 2011: Fundamental Science of Graphene and Applications of Graphene-Based Devices, April 24-29, 2011, Universitätszentrum Obergurgl, Austria

7. **First-principles investigation of the very large Perpendicular Magnetic Anisotropy at Fe|MgO interfaces** (Talk)
   H. X. Yang, J. H. Lee, M. Chshiev (presenter), A. Manchon, L. Nistor, K. H. Shin and B. Dieny
   Recent Trends in Nanomagnetism, Spintronics and their Applications (RTNSA), May 31 - June 4, 2011, Ordizia, Spain

8. **Shape induced Magnetic Moment in Graphene Nanomesh from First-Principles** (Poster)
   H. X. Yang (presenter), M. Chshiev, X. Waintal, S. Roche, 2011
   Graphene@IMAGINENANO, April 11-14, 2011, Bilbao, Spain

9. **Mechanisms of Perpendicular Magnetic Anisotropy at Fe(001)|MgO(001) Interfaces** (Talk)
   H. X. Yang, J. H. Lee, M. Chshiev (presenter), A. Manchon, K. H. Shin and B. Dieny
   2011 NanoSpain@IMAGINENANO, April 11-14, 2011, Bilbao, Spain

10. **Effects of shape and edge-passivation on magnetic moments in graphene nanomeshes by first-principles investigation** (Talk)
    Hongxin Yang (presenter) and Mairbek Chshiev
    2011 APS March Meeting, March 21-25, 2011, Dallas, TX, USA, T31.9

11. **Effect of occupation numbers on exchange coupling in low dimensional magnetic nanostructures** (Talk)
    D. Terrade, H. X. Yang, A. Kalitsov, L. Nistor, M. Chshiev (presenter), B. Dieny
    2011 APS March Meeting, March 21-25, 2011, Dallas, TX, USA, B19.12

12. **Perpendicular magnetic anisotropy of ultrathin epitaxial cobalt films on graphene** (Talk)

C. Vo-Van, Z. Kassir-Bodon, H. X. Yang, C. Johann (presenter), J. Vogel, S. Pizzini, P. Bayle-Guillemaud, M. Chsiev, L. Ranno, V. Santonacci, P. David, V. Salvador, O. Fruchart
55th Conference on Magnetism and Magnetic Materials, November 14-18, 2010, Atlanta, GA, USA, CE-05

13. **Oscillatory interlayer exchange coupling in Fe|GaAs|Fe and Fe|ZnSe|Fe tunnel junctions from first-principles calculations** (Talk)
H. X. Yang (presenter), M. Chshiev, A. Kalitsov, A. Schuhl, B. Dieny
55th Conference on Magnetism and Magnetic Materials, November 14-18, 2010, Atlanta, GA, USA, CB-09

14. **Effect of occupation numbers on Interlayer Exchange Coupling** (Talk)
D. Terrade, A. Kalitsov, H. X.Yang, M. Chshiev (presenter), X. Waintal, C. Baraduc, B. Dieny
55th Conference on Magnetism and Magnetic Materials, November 14-18, 2010, Atlanta, GA, USA, CB-08

15. **Highly stable calcium coated graphene nanoribbon for highly capacity molecular hydrogen storage** (Poster)
H. X. Yang (presenter), Yiyang Sun, L. F. Xu, Z. Fang, S. B. Zhang, and M. Chshiev
Graphene International School 2010, Oct. 11-23, Corsica, France.

16. **Mechanism of magnetotransport properties modulation via interfacial electronic structure in single crystal Fe-MgO-Fe tunnel junctions** (Poster)
C. Tiusan, H. X. Yang (presenter), M. Chshiev, F. Greullet, C. Bellouard, Y. Lu, F. Montaigne and M. Hehn
Colloque Louis Néel, Albé (France), March 30-April 02, 2010, P-ES-3

17. **Effect of oxidation conditions on interlayer exchange coupling in Fe/MgO/Fe MTJs from first-principles and tight-binding approaches** (Poster)
H. X. Yang (presenter), M. Chshiev, A. Kalitsov, A. Schuhl and W.H. Butler
Colloque Louis Néel, Albé (France), March 30-April 02, 2010, P-TMM-24

18. **Effect of oxidation on interlayer exchange coupling in Fe|MgO|Fe tunnel junctions** (Poster)
H. X. Yang, M. Chshiev (presenter), A. Kalitsov, A. Schuhl and W.H. Butler
2010 APS March Meeting, March 15–19, 2010, Portland, OR, USA, S1.00121

19. **Mechanism of magnetotransport properties modulation via interfacial electronic structure in single crystal Fe-MgO-Fe tunnel junctions** (Poster)
C. Tiusan, H. X. Yang (presenter), M. Chshiev, F. Greullet, C. Bellouard, Y. Lu, F. Montaigne and M. Hehn
11th Joint MMM/InterMag Conference, Washington, DC, Jan. 18-22, 2010, EV-07

20. **Effect of oxidation conditions on interlayer exchange coupling in Fe|MgO|Fe tunnel junctions from first-principles and tight-binding approaches** (Talk)
H. X. Yang (presenter), M. Chshiev, A. Kalitsov, A. Schuhl and W.H. Butler
11th Joint MMM/InterMag Conference, Washington, DC, Jan. 18-22, 2010, FB-08

ACKNOWLEDGEMENTS

I would like to thank my PhD advisor, professor Mairbek Chshiev for supporting me during these past three years. I will forever be thankful to him!

First, he has provided insightful and fruitful discussions, comments and advices about research. When discussing with him, you can feel his solid background on physics and mathematics! That surely benefits me a lot! I am very grateful to Mair for his scientific advice and knowledge and many insightful discussions and suggestions. He is my primary resource for getting my science questions answered. It is one of the joys to discuss with him! And as long as we were working in the lab, we would have at least a discussion about research. I roughly estimated that we may have close to one thousand times discussion in the past three years! That surely expanded my view of science, my understanding of research! More important is that during all the discussions, even though sometimes we may have different opinions, Mair always had enough patience to explain or to listen.

Secondly, Mair has been always so supportive and has given me the freedom to pursue various projects without objection.

Thirdly, Mair sent me to many conferences, and that did help me a lot to know what is going on from colleagues all over the world! Also Mair introduced me to many great researchers, which also expanded my research social life and made me love physics more and more!

Moreover, Mair helped a lot for my living life in France, since I do not speak French.

It is one of the luckiest things to have a great Ph.D advisor, and I did have!

I am also very grateful to Dr. Bernard Dieny and Prof. Alain Schuhl for their scientific advices, knowledge and many insightful discussions and suggestions, and their modest and kindness as well!

I also thank my collaborator, Dr. Alan Kalitsov, for his help and teaching while he was a postdoc in the group. He's a great theorist and has taught me a lot for tight binding calculations! Wish my old friend all the best in the US!

I would like to thank Prof. Stephan Roche as well! I met professor Roche during the 2010 ElecMol conference, but actually before that I've read his pioneer review paper on carbon nanotube published on review of modern physics. We started the collaboration since a discussion about graphene nanomeshes! He immediately gave us an advice to the explanation for magnetic moment on different nanomesh structures. He is so energetic and has a great passion on science! He is also very kind and very gentle to everyone!

I thank all the members of the group: Dr. Braham Belhadji, Dr. Ali Hallal and Damien Terrade and my collaborators all over the world: Prof. William. H. Butler, Dr. Xavier Waintal, Dr. O. Fruchart, Dr. J. Coraux, Prof. A. Manchon, Dr. J. H. Lee, Dr. D. W. Boukhvalov, Dr. Zhong Fang, Dr. Changzhi Gu, Dr. Lifang Xu, Dr. Chao Lu, Emilie. M. J. Hassen, Prof. Shengbai Zhang, Prof. Julian P. Velev, Dr. Wolfgang Wernsdorfer, Dr. Yuan Lu, and Prof. Alex Smogunov.

I would also like to thank my friends in Spintec Dr. Mihai Miron, Dr. Gilles Gaudin, Dr. Lavinia Nistor, Dr. Claire Baraduc, Dr. Ursula Ebels, Prof. Liliana Prejbeanu-Buda, Dr. Guillaume Prenat, Dr. Olivier Boulle, Dr. Wei Guo, Emilie Jue, Daria, Helga, Bertrand, Juan, Sylvain, Elmer, Perrine, Jiafeng, Mario, Maria, Ioana, Noel, Alex, Lara, Felipe, Michael, Gor, Emiline, Adrien, Julian, Thomas, Christophe, Abhijit, Marc, and Pierre-Yves.

Thank the football team in CEA, it is a great enjoyment to play football with those lazy guys ☺ or else I could not pass anyone so easily.

I would like to thank the help from the Director of Spintec, Dr.Jean-Pierre Nozieres, the human resource assitant Catherine Broisin and Rachel Mauduit!

Thank the help from nanosciecnes foundation: Dr. Alain Fontaine, Dr. Roland Herino, Dr. Marie-Anne Carré, Stéphanie Monfront, Maud Dayez, and Fériel Kouiten!

I would like to thank the jury: Prof. Dr. Stefan Blugel, Prof. Stefano Sanvito, Dr. Andre Thiaville, Prof. Alain Schuhl and Dr. Claudine Lacroix!

Finally, many thanks to my parents for their encouragement and support, thank my brother and his wife and my nephew Xirui.

I would like to dedicate this thesis to my wife, Manyun, and my son, Xilin, for their constant support and unconditional love.